

Flexible Co(II) Metal-Organic Frameworks with Mixed Ligands under Controlled Pressure

by Phumile Sikiti

Submitted in partial fulfilment of the requirements for the degree
Doctor of Philosophy

Promoter: Prof. Leonard J. Barbour



Department of Chemistry and Polymer Science
Faculty of Science
University of Stellenbosch

December 2019

Declaration

By submitting this dissertation electronically, I declare that the entirety of the work contained therein is my own, original work, that I am the sole author thereof (save to the extent explicitly otherwise stated), that reproduction and publication thereof by Stellenbosch University will not infringe any third party rights and that I have not previously in its entirety or in part submitted it for obtaining any qualification.

December 2019

Copyright © 2019 Stellenbosch University

All rights reserved

Acknowledgements

I have had a great deal of help in completing my PhD studies and writing this dissertation. The University of Stellenbosch has provided a uniquely fertile environment in which to explore my chemistry research. Prof. Len Barbour has not only been a supervisor and source of encouragement to me for many years but also extremely generous with both resources and understanding of how I want my PhD studies to be concluded.

To Dr Charl Bezuidenhout a friend, a colleague, a collaborator as well as a staunch and valued ally, and Dewald van Heerden: I thank you again. My heritage in the Supramolecular Materials Research group at Stellenbosch University has shaped my view as a researcher in chemistry and I am particularly grateful to Prof. Catharine Esterhuysen and Dr Leigh Loots for their support and for proof reading. I am also grateful to Drs Vincent Smith, Emile Engel, Lukman Alimi, Prem Lama and Banele Vatsha for sharing their wisdom with me. Thanks also go to Prof. Janet Scott at the Centre for Sustainable Chemical Technologies of the University of Bath for her incredibly kind supervision, as well as her help and amazing hospitality during my visit there.

An especial thank you is extended to Nokukhanya Cele for her constant encouragement and the support and wisdom. To Debbie Isaacs, I thank you very much too.

Finally, I am very grateful to my family and friends for the support and a great atmosphere outside of research and I fully acknowledge the National Research Foundation of South Africa for funding.

Abstract

A number of flexible metal-organic frameworks (MOFs) are shown to undergo phase changes under CO₂ gas pressure and, in two cases, the mechanisms of these changes have been elucidated using computational simulation and *in situ* variable-pressure single-crystal diffraction (VP-SCD). The primary objective of this work was to utilise suitable ligands to synthesise flexible cobalt-based MOFs that undergo phase changes under gas loading at 298 K. Where possible, the phase change mechanisms were visualised crystallographically at the molecular level by employing an environmental gas cell.

The first section describes a new non-interpenetrated flexible MOF, $\{[\text{Co}_2(\text{OBA})_2(\text{BPMP})] \cdot 1.5(\text{DMF})\}_n$ (**COB-DMF**), where OBA = 4,4'-oxybis(benzoic acid), BPMP = 4-bis(pyridin-4-ylmethyl)piperazine, with a new network topology. **COB** possesses minimal porosity and activation yields a framework with discrete voids and substantial reduction in guest-accessible volume. In the present study it is shown by means of *in-situ* VP-SCD that **COB** exhibits structural flexibility under CO₂ gas loading at 298 K in a single-crystal to single-crystal manner. The mode of flexibility combines two separate mechanisms, which is highly unusual. The results are supported by *in-situ* powder X-ray diffraction.

The second section describes a different MOF ($\{[\text{Co}_2(\text{OBA})_2(\text{BPMP})] \cdot 2.5(\text{DMF})\}_n$, **COB1**) prepared using the same components that were used to prepare **COB**. Although the stoichiometry was the same, the synthesis temperature was different and the framework systems are entirely different. Activation of **COB1** yields a narrow-pore framework from a wide-pore phase. The framework breathes and switches between the narrow-pore and wide-pore phases at a specific CO₂ loading pressure at 298 K. The proposed mechanism for flexibility is well supported by pressure-gradient differential scanning calorimetry and *in situ* VP-SCD and was further validated by means of molecular modelling.

The final section describes a new interdigitated two dimensional PCP $\{[\text{Co}_2(\text{OBA})_2(\text{BPY})_2] \cdot 2(\text{DMF})\}_n$. The material exhibits flexibility at a specific CO₂ pressure at 298 K, with large hysteresis upon desorption, the single crystals did not survive CO₂ uptake, and the flexibility was validated using VP-PXRD. Gas sorption analysis implies that the host exhibits shape memory upon complete desorption, but closer inspection of the desorption isotherm in the low-pressure range shows that the material reverts to its activated form upon complete guest removal. This constitutes approximately 26 bar of hysteresis in the reversal of the gas-induced phase transition.

Uittreksel

Dit word getoon dat 'n aantal buigbare metaal-organiese raamwerke (MOFs) fase verwisseling ondergaan onder CO₂ lading en in twee gevalle is die meganismes van die fase veranderinge uitgelê deur rekenaargebaseerde simulاسie en *in situ* veranderlike-druk enkel-kristal diffraksie (VP-SCD). Die hoof doelwit van hierdie werk was om gepaste ligande te gebruik vir die sintese van buigbare kobalt-gebaseerde MOFs wat fase verwisseling weens gas lading by 298 K ondergaan. Die meganisme van die fase veranderinge was, waar moontlik, kristallografies gevisualiseer deur van 'n gassel gebruik te maak.

Die eerste afdeling beskryf 'n nuwe nie-geïnterpenitreeerde buigbare MOF, $\{[\text{Co}_2(\text{OBA})_2(\text{BPMP})] \cdot 1.5(\text{DMF})\}_n$ (**COB-DMF**), met 'n nuwe network topologie. **COB** beskik oor beperkte poreusheid en aktivering lewer 'n raamwerk met aparte leemtes en 'n aansienlike verlaging in gas-toeganklike volume. In die huidige studie word deur middel van *in situ* VP-SCD gewys dat **COB** strukturele buigbaarheid toon onder CO₂ gas lading by 298 K in 'n enkel-kristal na enkel-kristal wyse. Die modus van buigbaarheid kombineer twee meganismes, wat uitsonderlik is. Die resultate word ondersteun deur *in situ* poeier X-straal diffraksie (PXRD).

Die tweede afdeling beskryf 'n ander MOF ($\{[\text{Co}_2(\text{OBA})_2(\text{BPMP})] \cdot 2.5(\text{DMF})\}_n$, **COB1**) wat verkry is vanaf dieselfde komponente as wat vir die voorbereiding van **COB** gebruik is. Alhoewel die stoïgiometrie dieselfde is, is die temperatuur van sintese anders en die raamwerk sisteme uiteenlopend anders. Die aktivering van **COB1** lewer 'n nou-porie raamwerk vanaf 'n wye-porie fase. Die raamwerk ondergaan 'n asemhaling en skakel tussen die nou-porie en wye-porie fase by 'n spesifieke CO₂ druk by 298 K. Die voorgestelde meganisme vir buigbaarheid word goed ondersteun deur druk-gradiënt differensiële skanderings kalorimetrie, *in situ* VP-SCD asook molekulêre modellering.

Die laaste afdeling beskryf 'n nuwe gedigiteerde twee dimensionele MOF $\{[\text{Co}_2(\text{OBA})_2(\text{BPY})_2] \cdot 2(\text{DMF})\}_n$. Die materiaal vertoon buigbaarheid by 'n spesifieke CO₂ druk by 298 K met groot desorpsie histerese. Die kristal oorleef egter nie en die buigbaarheid is bevestig deur middel van VP-PXRD. Gas sorpsie analise impliseer dat die gasheer vormgeheue tentoonstel, maar met nouer ondersoek van die desorpsie isotherm is gevind dat die materiaal terugkeer na die geaktiveerde vorm na volledige verwydering van die gas. Hierdie maak histerese van ongeveer 26 bar uit en 'n omkeer van die gas-geïnduseerde fase verandering vind plaas.

Manuscripts

1. **P. Sikiti, C. X. Bezuidenhout, D. P. van Heerden and L. J. Barbour.** Direct in situ Crystallographic Visualization of a Dual Mechanism for Uptake of CO₂ Gas by a Flexible MOF. Submitted to *Inorganic Chemistry* For consideration as a communication.
2. **P. Sikiti, C. X. Bezuidenhout, D. P. van Heerden and L. J. Barbour.** A new dynamic framework with direct in situ visualisation of breathing under CO₂ gas pressure. Submitted to *CrystEngComm* for consideration as an article.
3. **P. Sikiti and L. J. Barbour.** A new interdigitated porous coordination polymer that exhibits flexibility and highly hysteretic shape recovery with CO₂ sorption and desorption at 298 K. Not yet submitted.

Abbreviations

1D	1-dimensional
2D	2-dimensional
3D	3-dimensional
ASU	Asymmetric unit
BPMP	4-bis(pyridin-4-ylmethyl)piperazine
BPY	4,4'-bipyridine
DMF	dimethylformamide
HFU	Host formula unit
MOF	Metal-organic framework
<i>np</i>	Narrow-pore
OBA	4,4'-oxybis(benzoic acid)
PCP	Porous coordination polymer
PG-DSC	Pressure-gradient differential scanning calorimetry
SBU	Secondary building unit
TGA	Thermogravimetric analysis
VP-PXRD	Variable pressure powder X-ray diffraction
VP-SCD	Variable pressure single-crystal X-ray diffraction
<i>wp</i>	Wide-pore

TABLE OF CONTENTS	
Declaration	i
Acknowledgements	ii
Abstract	iii
Manuscripts	v
Abbreviations	vi
TABLE OF CONTENTS	vii
CHAPTER 1	1
INTRODUCTION	1
1.1. Porous Materials	1
1.2 Porous coordination polymers	2
1.3. Two dimensional coordination polymers.....	3
1.4. Metal-Organic Frameworks (MOFs)	4
1.4.1. Synthesis of MOFs	5
1.4.2. Secondary building units	6
1.4.3. Isorecticular synthesis of MOFs	6
1.5. Porosity in MOFs.....	7
1.6. Gas sorption.....	8
1.7. Flexible MOFs	10
1.8. Aims.....	12
1.9. Thesis Outline	12
REFERENCES.....	14
CHAPTER 2	18
2.1. Manuscript submitted to <i>Inorganic Chemistry</i>	18
2.2. Supporting Information	24
CHAPTER 3	32
3.1. Manuscript submitted to <i>CryEngComm</i>	32
3.2 Supporting information.....	37
CHAPTER 4	45
4.1. Manuscript not yet submitted	45
4.2. Supporting information.....	51
CHAPTER 5	57
Summary and Conclusion	57
APPENDIX	59

CHAPTER 1

INTRODUCTION

1.1. Porous Materials

Much attention has been devoted to the use of many different compounds to create nanostructured materials. Such materials are considered of interest for applications such as separation, storage of gases, sensing, and heterogeneous catalysis.¹ Until the mid-1990s two types of porous materials were in widespread use, namely inorganic and carbon-based materials. The inorganic materials are divided into two subclasses, the aluminosilicates and aluminophosphates.² Aluminosilicates are zeolites and a class of microporous crystalline materials which have been extensively studied for many years.¹

They are made from low silica to high alumina ratios in order to produce 3-dimensional (3D) crystalline hydrated alkaline or alkaline-earth aluminosilicates with the general formula $M^{n+}[(AlO_2)_x(SiO_2)_y]x \cdot wH_2O$ (M = metal).³ They have corner-sharing TO_4 tetrahedra ($T = Al, Si$), and form interconnected tunnels or cages in which water molecules and metal ions are inserted.³ After removal of water from these cages zeolites remain unaltered, yielding porous frameworks that are highly stable with uniformity in the pore size.⁴ As a result, zeolites have been reported as molecular sieves for sorption applications as well as other applications of interest to the global economy.⁵ However, a major limitation of zeolites is their high affinity for guest molecules, which results in difficulty when guests need to be released.

As a consequence, attention has shifted towards the use of activated carbons, which are porous materials with high surface areas that provide relatively strong adsorption sites for gases while also allowing gas release (desorption).⁶ Activated carbons are structurally disordered and feature twisted networks of defective hexagonal carbon layers that are cross-linked by aliphatic bridging groups.⁷ The widths of the layers of activated carbons vary, but are typically about 5 nm when simple functional groups are attached. Heteroatoms can be incorporated into the network and bound to the periphery of the carbon layers. Non-homogeneity of activated carbon limits the efficiency as a material for selective sorption and separation of guests. Although activated carbon and zeolites have high thermal stability due to their strong C-C or Si-O bonds, respectively, their syntheses remain challenging in the context of designing new frameworks with new topologies that possess various pore size and shapes such that gases can be released when needed. A limited number of other porous materials have also been reported. These include Werner complexes $[\beta-M(4\text{-methylpyridyl})_4(NCS)_2]$ ($M = Ni^{II}$ or Co^{II}), Prussian blue compounds and Hofmann clathrates (constructed from carbon nitrile linkages between square-planar or tetrahedral tetracyanometallate units and octahedral metal units coordinated by complementary ligands), which reversibly absorb small molecules.^{8,9}

In the early 1990s Robson¹⁰ introduced a new class of porous material consisting of a wide range of infinite 3D scaffold-like frameworks that are accessible and tunable. Their synthesis generally occurs under mild conditions with careful selection of discrete molecular units in order to produce a desired extended framework with large cavities, low density and accessible space while maintaining high thermal, chemical and mechanical stability. These 3D frameworks hold much potential for use in applications such as molecular sieving, ion exchange and catalysis.^{10,11} Some years after Robson's first report, other researchers demonstrated the use of carboxylate-based ligands under hydrothermal conditions to obtain robust 3D crystalline frameworks with open cavities,¹² and around the same time a 3D framework was used for methane storage at ambient temperature.¹³ Thereafter, Kitagawa showed that frameworks could

be constructed by combining different connectors such as metal nodes or clusters, and organic linkers to produce an endless array of architectures, as summarised in Figure 1.¹⁴ The strategy can be employed to great success in the formation 1D, 2D and 3D framework architectures. The term metal-organic framework (MOF) was proposed, and used as the technical term for any extended framework comprised of metal nodes and organic linkers (either mono- or polynuclear).¹² Nevertheless, there is still little distinction in the literature with regard to the definitions of porous coordination polymers (PCPs) and MOFs. According to IUPAC guidelines, a MOF is an extended porous coordination network, and thus restricted to 3D frameworks. The term PCP is generally used to describe porous metal-organic systems with one (1D) or two dimensional (2D) connectivity.¹⁵ Therefore, in this dissertation, we explicitly describe 1D and 2D systems as PCPs, and 3D frameworks as MOFs.

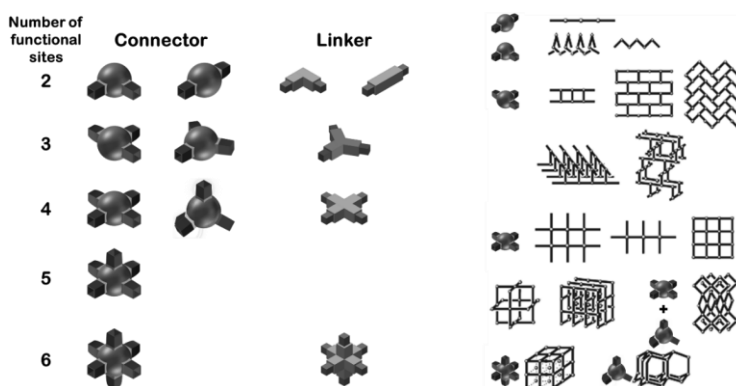
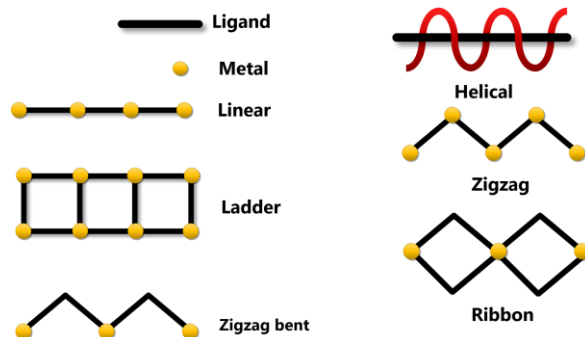


Figure 1. Components of coordination polymers and possible frameworks that can be assembled using different combinations of connectors and linkers. Figure recreated from reference 14.

1.2 Porous coordination polymers

Nearly 55 years ago, an analogy between organic polymers and a class of inorganic coordination complexes was drawn and the name “coordination polymers (CPs)” was coined.¹⁶ Since then, 1D coordination polymers have been studied intensely. They employ (usually ditopic) organic linkers to join metal centres to form conceptually-infinite coordination chains. The modular nature of these compounds makes it relatively easy to develop strategies for engineering multifunctional polymeric materials.¹⁷



Scheme 1. Various geometrical conformations that show the diversity of 1D coordination polymers.

1D CPs normally yield interesting architectures with appealing functional properties. Architectures such as linear, ladder, ribbon, zigzag and helical structures (**Scheme 1**) are possible, depending on the conformations of the ligands, and the coordination environment of the metal ions under specific conditions.¹⁸ The formation of these different architectures can depend on the conditions of their formation, such as temperature, the nature of the solvent, and relative concentrations of the reactants.

1.3. Two dimensional coordination polymers

Evidently, the topology of a 2D framework depends on factors such as the ligand to metal ion ratio, the preferred metal coordination geometries, as well as the nature of the coordination ligands. For example, the combination of transition metal ions with linear bifunctional ligands in a ratio of 1:2 have yielded many square grid 2D frameworks.¹⁹ Other topologies such as rhombic, rectangular, herringbone, brick wall, honeycomb and bilayers have been also reported^{20,21} (**Figure 2**).

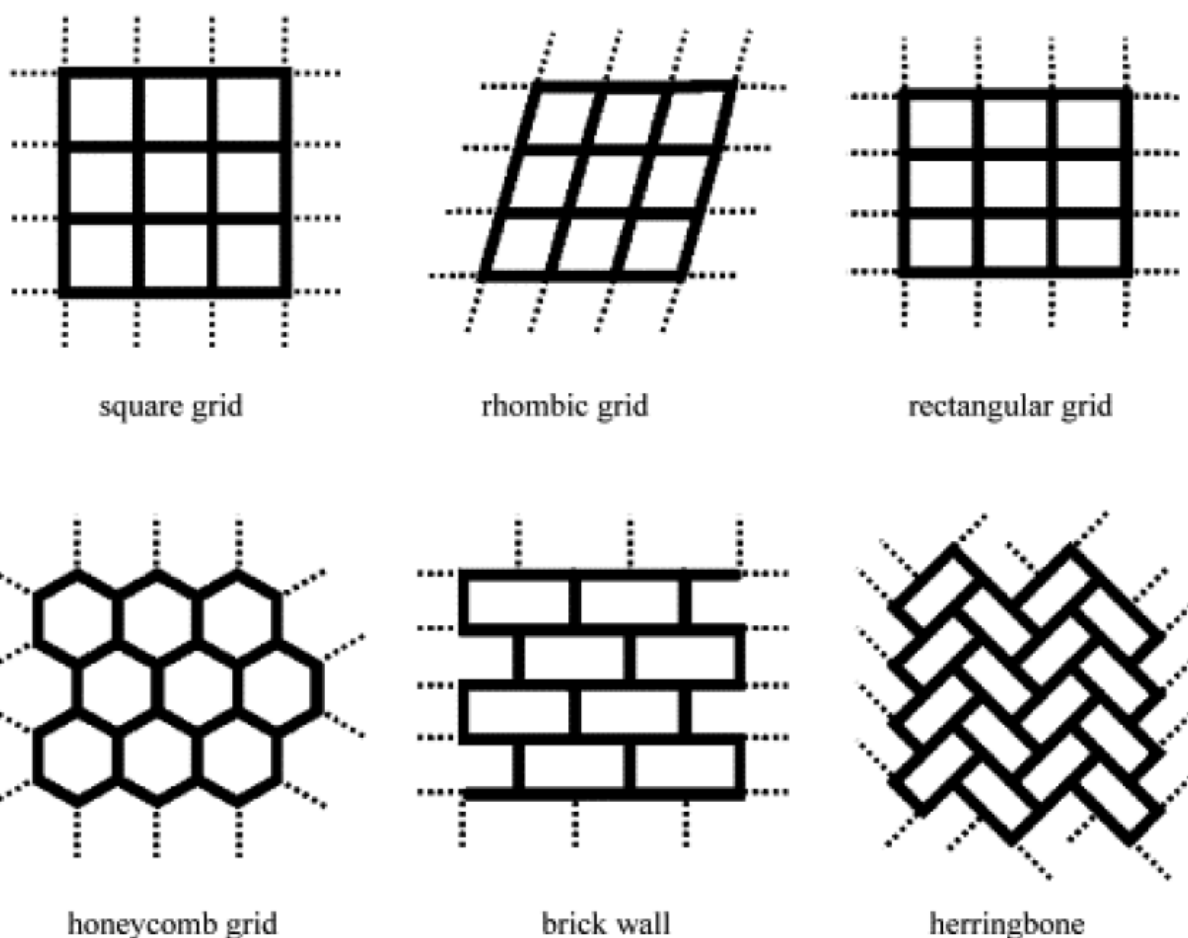


Figure 2. Different examples of 2D coordination polymers (from reference 19).

There are also many examples of mixed ligand 2D systems; e.g. Cu^{II} nitrate, 2,5-dihydroxybenzoic acid (HDHBC) and 4,4'-bipyridine (4,4'-BPY) were used to synthesise a square-grid coordination polymer.

The metals are connected in one dimension by 4,4'-BPY to produce straight chains, which are then cross-linked by DHBC to yield interdigitated 2D frameworks²² (**Figure 3**).

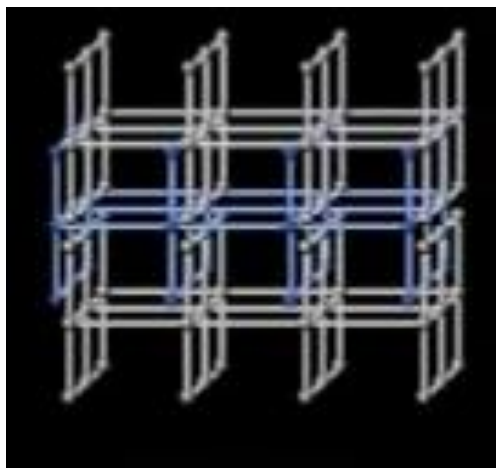


Figure 3. Schematic representation of $[\text{Cu}(\text{DHBC})_2(4,4'\text{-BPY})]\cdot\text{H}_2\text{O}$. Reproduced from reference 22.

Since then, many other examples of mixed-ligand 2D frameworks have been reported.^{23,24} Some have exhibited potentially useful properties; Kitagawa and co-workers recently reported a 2D PCP $[\text{Mn}(\text{BDC})(\text{DPE})]$ (where H_2BDC = 1,4-benzenedicarboxylic acid, DPE = 1,2-di(4-pyridyl)ethylene) with zero-dimensional pores, which shows an adsorbate discriminatory gate effect for C_2H_6 over CO_2 gas.²⁵ This system was characterized using synchrotron powder X-ray diffraction analysis and computational methods.

1.4. Metal-Organic Frameworks (MOFs)

Three dimensional coordination networks were discovered well after the initial work on Werner complexes, Prussian blue compounds, and Hofmann clathrates and their derivatives.^{8,9} However, their sorption behaviour was not reported in the initial articles.¹⁰ Nevertheless, these frameworks soon inspired many scientists to investigate the copolymerization of a wide range of larger organic linkers with metal-ions to yield a class metal-organic frameworks (MOFs) with unusual open architectures and unprecedented pore size and shape.¹² Consequently, secondary building units (SBUs) were introduced as a new modular approach (**Figure 4**) to designing and preparing new robust MOFs that remain stable even after solvent removal.²⁶

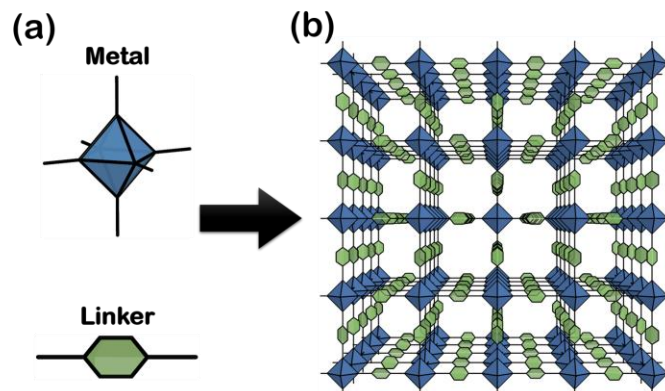


Figure 4. Schematic representation of the basic concept behind MOF framework assemblies using the MOF-5 crystal structure as an example, (a) with metal ion and linker components, and (b) a typical framework that can be formed using these components

Additionally, computational predictions have advanced significantly to yield MOFs with better stability and larger pores (30-40 Å).²⁷ Hence, there are thousands of MOF structures in the Cambridge Structural Database, including MOFs with densities as low as 0.13 g cm⁻³,²⁸ accessible space up to 90% free volume,^{29,30} and surface areas greater than 6000 m² g⁻¹.^{31,32} Given that MOFs are constructed from a variety of inorganic nodes (i.e. metal clusters or ions) and organic linkers, the number of metal-organic combinations (**Figure 4**),²⁶ and their structural possibilities, are essentially endless.

Furthermore, MOFs are not only limited to potential application such as gas storage and separation,^{31,33} but they have also been shown to have relevance for a wide variety of other applications, including chemical separations,^{34,35} catalysis,^{36,37} drug delivery,³⁸ light harvesting,³⁹ energy conversion,⁴⁰ sensing,⁴¹ conductivity,⁴² ion-exchange⁴³ and removal of toxic substances from air and water.^{44,45}

1.4.1. Synthesis of MOFs

Optimization of parameters such as molar ratios of starting materials (reactants), pH, quantities/ratios/types of solvents, process parameters such as reaction time, temperature, and pressure yields thousands of new frameworks every year. Evidently, synthetic methods using the same ligands and metal ion under different conditions can result in a variety of interesting structures.^{46,47} The conventional solvothermal methods for synthesising MOFs involve mixing of components at room temperature, followed by heating for 12-72 h or more, and then cooling to room temperature. However, while the above procedures generally yield high quality crystalline materials, they suffer from long reaction times and can be difficult to scale up above 1 g, especially when making use of high boiling point solvents such as dimethylformamide (DMF).⁴⁸

Therefore, alternative synthetic routes such as microwave, sonochemical, and mechanochemical methods, which are use less solvent with fast reaction times have recently been reported.^{47,49} The two most commonly used methods are hydrothermal or solvothermal, and microwave-assisted syntheses. Hydrothermal or solvothermal syntheses use solvents such as water (hydrothermal) or dimethylformamide (solvothermal, when not water). These solvents can also act as reagents at elevated temperature to deprotonate carboxylic acid groups of ligands. The reactions take place in closed vessels under

autogenous pressure above the boiling point of the solvent.⁵⁰ Microwave-assisted synthesis utilises the interaction of electromagnetic waves with polar species in solution, or with electrons/ions in a solid as a very energy-efficient homogeneous method of heating.⁵¹

1.4.2. Secondary building units

MOFs now constitute a major class of porous materials and thousands of articles are published annually on the topic because of potential applications.⁵² One of the major design strategies that has fuelled MOF synthesis since its inception is that of ‘reticular chemistry’.⁵³ Reticular synthesis can be described as the process of assembling judiciously designed rigid molecular building blocks into predetermined ordered structures (networks), which are held together by strong bonds.⁵⁴

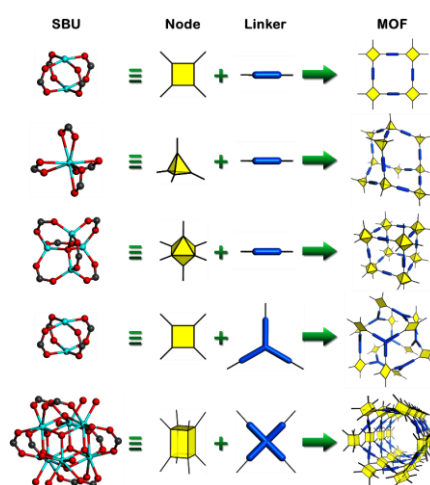


Figure 5. Schematic illustration of the construction of MOFs from SBUs and rigid linkers.⁵⁵

Using the principles of reticular chemistry, MOFs are assembled by linking molecular units with well-defined shapes via strong bonds into periodic arrays. The ligands used in MOF syntheses are carefully selected according to the number and orientation of Lewis-basic sites, and they are combined with metal centres to produce well-defined metal cluster motifs called secondary building units (SBUs) (**Figure 5**).⁵⁶ Topologically, MOF structures can be classified based on the SBUs employed.

One of the most widely used SBUs is constructed from metal-carboxylate clusters using rigid aromatic polydentate carboxylic acids as linker precursors.^{26,57-61} **Figure 5** depicts the most common metal-carboxylate SBUs, which may be combined with different linker geometries to afford a wide range of 3D architectures.^{56,62} Furthermore, the term linker in MOF synthesis describes a ligand that participates in the coordination assembly.⁶³

1.4.3. Isoreticular synthesis of MOFs

A vast number of MOF architectures and topologies have been produced just by replacing organic dicarboxylate ligands with those containing modified spacers.⁶⁴ Generally, a spacer in a ligand is a synthetically inert part of the ligand with respect to MOF synthesis, but it can also alter the functional

properties of the MOF. As a result, MOFs produced using this approach usually possess the same network topology and the principle is referred to as “isoreticular synthesis”.⁶⁴ A typical systematic study of an isoreticular series was produced, and the MOFs were referred to as IRMOFs (**Figure 6**).⁵⁷

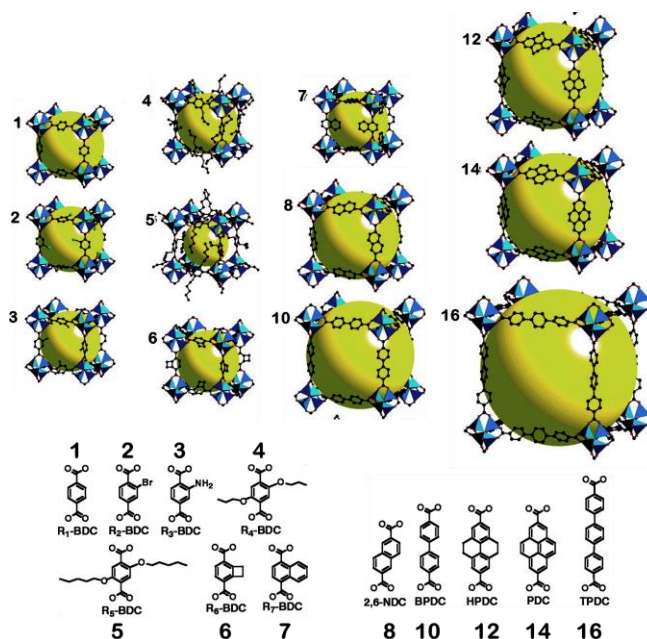


Figure 6. An isoreticular series of IRMOFs showing variation in the spacers. In each case the MOF cavity size is indicated by a large yellow sphere.⁵⁷

The systematic study was based on increasing the length of the spacer in the organic dicarboxylate linker, which resulted in a corresponding increase in the pore volume. More importantly, functionalization was also introduced by adding side groups (e.g. -Br, -NH₂, etc.).⁶⁵ However, it is important to note that to date it is still difficult, although not impossible, to predict the outcome of the MOF synthesis because simple metal ions and organic linkers hold little information about their directionality. This lack of directionality often results in flexibility around the metal ion, which can produce a multiplicity of possible structures.⁶⁶⁻⁶⁸

1.5. Porosity in MOFs

MOFs are attractive because they have pores in their networks that can be functionalized and occupied by guest molecules. However, there should be proof that a MOF is indeed porous, hence permeability of the host phase should be demonstrated.⁶⁹ Normally, porosity can be verified experimentally by determining the surface areas of the material using BET (Brunauer-Emmet-Teller) analysis of a nitrogen sorption experiment at 77 K.⁷⁰ However, it is worth noting that the abovementioned experimental method has its own limitations because the MOF could be permeable only to nitrogen but not to other guests. In addition, MOF materials can have voids within their structures without being permanently porous.⁷¹ Generally the porosity of a MOF is categorised based on the dimensionality of the voids (**Figure 9**).¹⁴ These void could consist of zero-, one-, two- or three-dimensional pores. Zero-dimensional pores are isolated within the host framework. One-dimensional porosity refers to non-intersecting channels, while

two-dimensional porosity describes assemblies of separate layers of available space. Three-dimensional porosity constitutes a system of intersecting channels.¹⁴

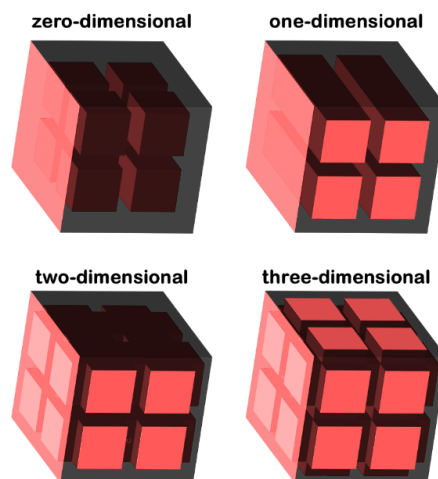


Figure 7. The four categories for the dimensionality of porosity in MOFs/PCPs: 0D, 1D, 2D and 3D porosity.¹⁴

1.6. Gas sorption

Sorption behaviour is divided into two types: *adsorption* and *absorption*. Adsorption is based on enrichment of one or more components in an interfacial layer. Absorption is when molecules enter the bulk of the material. To avoid confusion, the term sorption is often used instead of adsorption and absorption. The counterpart of sorption is desorption, which is simply the converse process in which the amount of the adsorbed guest decreases.

When the sorption and desorption profiles do not coincide, the process is called hysteresis. Sorption usually occurs because of either physisorption or chemisorption, and these processes are determined by what type of an interaction is involved in the sorption process. Specifically, physisorption occurs when a gas (adsorbate) contacts a surface of the solid (adsorbent) and the interaction between the two is very weak, with the enthalpy of adsorption being less than 10 kcal mol⁻¹. Chemisorption normally occurs with the formation of chemical bonds and an enthalpy of adsorption in the range of 25-95 kcal mol⁻¹. The amount of the gas (adsorbate) being absorbed by the solid during the sorption process is referred to as the sorption capacity. This is usually governed either by the molecular sieving effect, which is based on a size/shape exclusion principle, or the thermodynamic effect, which results from preferential packing of gas molecules in the pores of the host, the channel topology and the surface interactions between gas molecules and the channel walls.

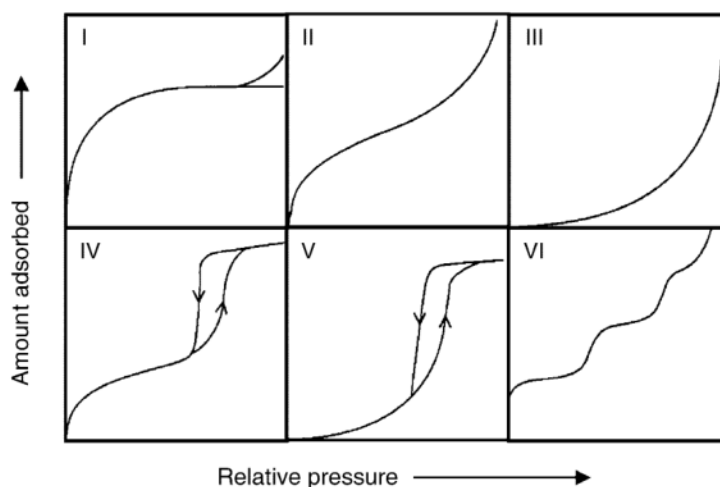


Figure 8. IUPAC classification of adsorption isotherms.⁷²⁻⁷⁴

There is also a kinetic effect, which results from different gases having different kinetic diameters and energies, which in turn leads to variation in diffusion rates. All of the above effects contribute to the characteristic isotherms associated with sorption. As a result, there are six types of characteristic isotherms, as categorized by the IUPAC (**Figure 8**).^{67,73,74}

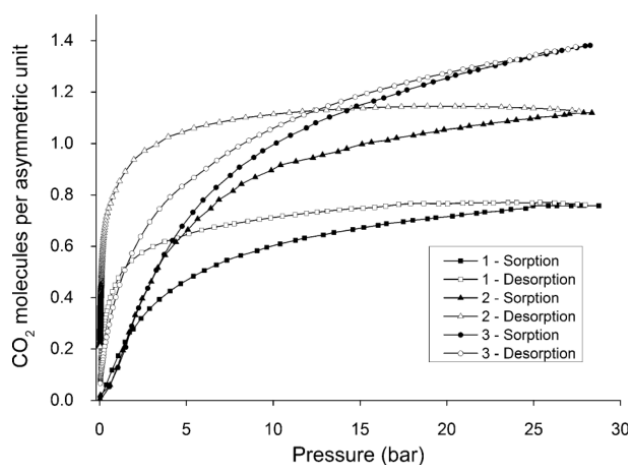


Figure 9. Type I CO₂ sorption and desorption isotherms.⁸⁷

Type I isotherms are usually associated with microporous frameworks, types II, III and VI with macroporous materials, and types IV and V exclusively with mesoporosity (**Figure 8**). Furthermore, the shape of an isotherm is influenced by pore size, host-guest and guest-guest electrostatic interactions, and could result in artefacts being produced. Sorption/desorption hysteresis occurs in rigid MOFs due to strong host-guest interactions and gas trapping within the pore apertures.⁷⁵ An exceptional example of extreme hysteresis under CO₂ gas sorption at 298 K is shown in **Figure 9**. This was observed during an investigation of the three frameworks [Cu₂(glu)₂(bpy)]·2.9H₂O, [Cu₂(glu)₂(bpe)]·3H₂O, and [Cu₂(glu)₂(bpymh)]·7.5H₂O, where glu = glutaric acid, bpy = 4,4'-bipyridine, (bpe) = trans-bis(4-pyridyl)ethylene, and (bpymh) = N,N'-bis(pyridine-4-ylmethylene)hydrazine.

1.7. Flexible MOFs

In 1998 MOFs were first categorised into three generations (**Figure 10**): first, second and third generation based on their response to guest removal.⁷⁶ The first generation collapses and loses its structural integrity and porosity upon guest removal, or even after sorption. The second generation is usually rigid after guest removal and subsequent guest sorption. Third generation MOFs are flexible soft porous crystals that collapse upon guest removal and regenerate upon guest uptake.⁷⁷ Evidently, third generation MOFs demonstrate structural flexibility with a reversible response to external stimuli, such as changes in temperature or gas pressure, even in the absence of guest.^{52,78}

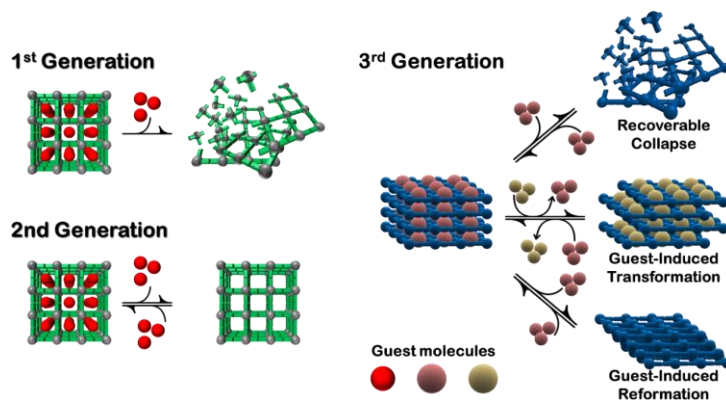


Figure 10. Schematic representation of first, second and third generation porous coordination polymers as described by Kitagawa.^{76,79,80}

Researchers have recently turned their attention to flexible MOFs because they absorb minimal gas before flexibility, and then exhibit an abrupt rise or “step” in adsorption upon undergoing a structural phase change.^{25,78,80,81} This drastic change in sorption behaviour is evident as a step in the sorption isotherm, which may also exhibit hysteresis that enhances selectivity, yields high working capacities, and reduces thermal management requirements.^{82,83} The structural phase change behaviour of these materials can occur through a variety of mechanisms, which include breathing (ligand stretching or flexing), swelling, linker rotation, or subnetwork displacement and slippage of interdigitated and stacked layers. (**Figure 11**).⁸⁴⁻⁸⁷

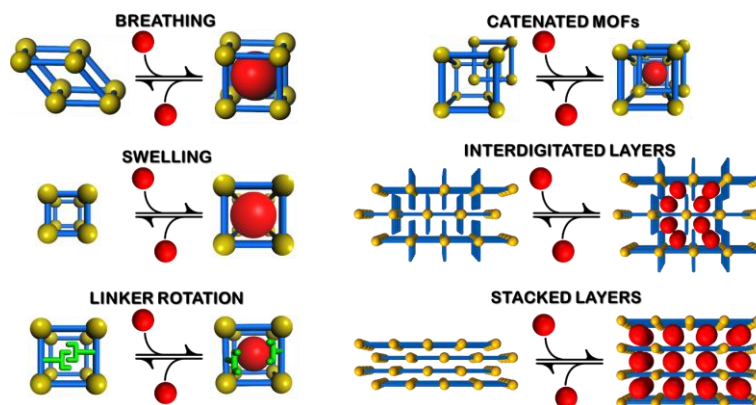


Figure 11. Classification of different modes of flexibility in MOFs. Figure recreated from ref⁸⁸.

The earliest examples of flexible MOFs that exhibit such structural phase change behaviour under gas pressure are the flexible MIL (Materials of Institute Lavoisier) family of MOFs ($[M(X)(BDC)]$, where M is trivalent Al, Cr, Fe or Ga and X is OH^- or F^-).^{27,78,89-92} Owing to the difficulty of producing large single crystals, the structural phase change behaviour in the MIL series was characterized by synchrotron powder X-ray diffraction analysis and computational simulation.^{78,89,91,93-96}

Recently researchers introduced flexible pillared-layered mixed-ligand MOFs (**Figure 12a**) of general composition M_2L_2P (P = neutral nitrogen donor ligand, L^{2-} = dicarboxylate and M^{2+} = divalent metal ion) to yield new pressure-dependent porous forms.⁹⁷ Some of these MOFs consist of interpenetrated networks,^{98,99} meaning they have more than one copy of the network crisscrossing one another to minimize space. Interestingly, they have been shown to exhibit flexibility under gas pressure due to subnetwork displacement or sliding of interpenetrated layers,^{25,81,100-103} by means of PXRD analysis as characterization method at low pressure and non-ambient conditions.^{81,101,103,104}

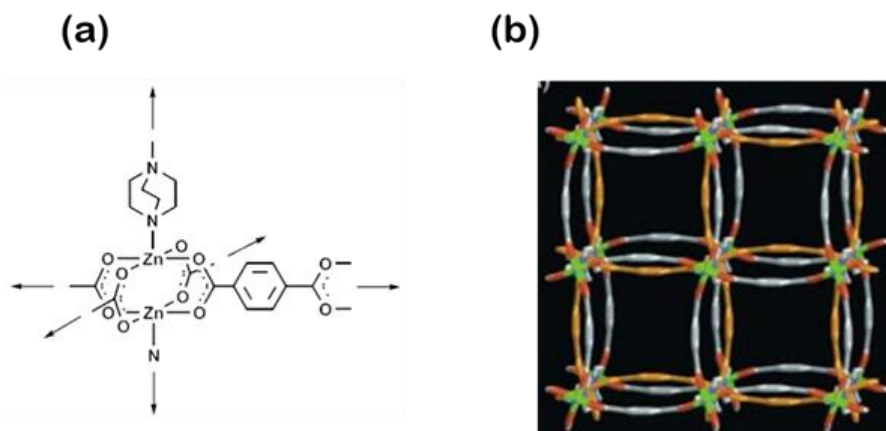


Figure 12. (a) The extension of the 2D square-grid of $\{Zn_2(1,4-bdc)_2\}$ into a 3D structure by using dabco, which occupies the axial positions and, (b) a view along the fourfold axis of the metal–organic framework structure.¹⁰⁵

Researchers have also used linear dicarboxylic ligands bearing flexible substituents together with neutral N-donor ligands as mixed-ligand systems to yield non-interpenetrated flexible pillared-layered MOFs,¹⁰⁶ and their flexibility is attributed to dangling functionality of the dicarboxylic ligand in response to gas pressure at non-ambient conditions.^{107,108} Noticeably, all of the abovementioned flexible pillared-layered MOFs commonly form structures composed of dinuclear M^{2+} linked equatorially by dicarboxylate dianions (L^{2-}) to form ‘paddlewheel’ two-dimensional M_2L_2 sheets with square grid topology (**sql**).¹⁰⁷ The axial sites of the paddlewheels are coordinated by bipyridyl ligands, which link the **sql** networks as pillars to generate three-dimensional (3D) networks (**Figure 12a**), with primitive cubic (**pcu**) topology (**Figure 12b**).¹⁰⁵

In general, structural phase change mechanisms of flexible MOFs have been elucidated using computational simulation and *in situ* variable-pressure VP-PXRD at non-ambient temperature,¹⁰⁹ while a few have been determined by means of *in situ* variable-pressure single-crystal X-ray diffraction analysis (VP-SCD) at 298 K.¹¹⁰⁻¹¹¹ Although the number of flexible materials characterized using VP-PXRD

outnumber those studied by VP-SCD, VP-SCD analysis is a superior analytical tool for investigating structural phase change mechanisms of flexible MOFs. However VP-SCD is more challenging because the stresses and strains due to structural changes rarely occur without fracturing of the single crystal.^{52,99,112} If the single crystals can survive activation and subsequent gas uptake, VP-SCD can enable a direct visualization of the structural phase changes and thereby provide detailed structural information, which may guide researchers to synthesise potential materials for gas-capture or separation applications.

1.8. Aims

The aim of the work presented here was to use the versatility of MOF synthesis to prepare flexible Co(II)-based MOFs with mixed ligands 4,4'-oxybis(benzoic acid) (OBA) with either 4-bis(pyridin-4-ylmethyl)piperazine (BPMP) or 4,4'-bipyridine (BPY), and to investigate their phase change behaviour under CO₂ loading. Where possible, we intended to use *in-situ* VP-SCD to investigate the phase change mechanisms at the molecular level by employing an environmental gas cell. Moreover, complementary experimental techniques such thermal analysis, volumetric sorption analysis, *in-situ* VP-PXRD and P-DSC were used to validate the phase change behaviour of the MOFs under pressure. This study has provided some insight into the mechanisms that induce phase changes under controlled gas pressures in these flexible MOFs.

1.9. Thesis Outline

This dissertation is presented as three manuscripts formatted for submission to journals for publication (Chapters 2-4). The methodologies and experimental conditions used during the work are described in the Supplementary Information sections of each of the relevant chapters.

Chapter 2 describes a new three dimensional non-interpenetrated flexible MOF, $\{[\text{Co}_2(\text{OBA})_2(\text{BPMP})] \cdot 1.5(\text{DMF})\}_n$ (**COB**), with a new 6-connected uninodal net topology, prepared from mixed ligands. **COB** displays structural flexibility under CO₂ gas pressure at 298 K and the resultant porous phases have been characterized by *in situ* VP-SCD analysis. Activation yields a framework with discrete voids and substantial reduction in guest-accessible volume, and **COB** exhibits a breathing mode of flexibility, combined with an overall swelling of the framework. This combination of mechanisms is highly unusual. This chapter has been submitted (as presented) to *Inorganic Chemistry* for consideration as a communication.

Chapter 3 describes a different MOF ($\{[\text{Co}_2(\text{OBA})_2(\text{BPMP})] \cdot 2.5(\text{DMF})\}_n$, **COB1**) using the same components that were used to prepare **COB**. Although the stoichiometry was the same, the synthesis temperature was different. Using single-crystal X-ray diffraction analysis, we show that desolvation yields a framework with substantial reduction in guest-accessible volume. The framework breathes and switches between the narrow pore and wide-pore phases at specific CO₂ loading at 298 K. The characterization of this breathing behaviour is well supported by pressure-gradient differential scanning calorimetry and *in situ* VP-SCD. VP-SCD analysis shows that the deformation of the coordination geometry and flexibility of the pillaring ligand leads to an overall breathing of the framework, which is further validated by means of molecular modelling. This chapter has been submitted (as presented) to *CrystEngComm* for consideration as a full paper.

Chapter 4 describes a new interdigitated two dimensional PCP $\{[\text{Co}_2(\text{OBA})_2(\text{BPY})_2] \cdot 2(\text{DMF})\}_n$. The material exhibits flexibility at a specific CO_2 pressure at 298 K, with large hysteresis on upon desorption. Although the single crystals did not survive CO_2 uptake, the flexibility was validated using VP-PXRD. This chapter, although formatted using the RSC template, has not yet been submitted for publication.

Chapter 5 summarises this work and presents some concluding remarks.

REFERENCES

- (1) Tao, Y. S.; Kanoh, H.; Abrams, L.; Kaneko, K. *Chem. Rev.* **2006**, *106*, 896.
- (2) Kitagawa, S.; Kitaura, R.; Noro, S. *Angew. Chem. Int. Ed.* **2004**, *43*, 2334.
- (3) Wilson, S. T.; Lok, B. M.; Messina, C. A.; Cannan, T. R.; Flanigen, E. M. *J. Am. Chem. Soc.*, **1982**, *104*, 1146.
- (4) Flanigen, E. M. In *Studies in Surface Science and Catalysis*; Elsevier: **1991**; 58,13.
- (5) Lok, B. M.; Cannan, T. R.; Messina, C. A. *Zeolites* **1983**, *3*, 282.
- (6) Siriwardane, R. V.; Shen, M.-S.; Fisher, E. P.; Poston, J. A. *Energy Fuels* **2001**, *15*, 279.
- (7) Lu, W.; Chung, D. D. L. *MRS Proceedings* **1996**, *454*.
- (8) Iwamoto, T. *Journal of Inclusion Phenomena and Molecular Recognition in Chemistry.* **1996**, *24*, 61.
- (9) Park, K.-M.; Kuroda, R.; Iwamoto, T. *Angew. Chem. Int. Ed. Engl.* **1993**, *32*, 884.
- (10) Hoskins, B. F.; Robson, R. *J. Am. Chem. Soc.* **1990**, *112*, 1546.
- (11) Fujita, M.; Kwon, Y. J.; Washizu, S.; Ogura, K. *J. Am. Chem. Soc.* **1994**, *116*, 1151.
- (12) Yaghi, O. M.; Li, H. *J. Am. Chem. Soc.* **1995**, *117*, 10401.
- (13) Noro, S.; Kitagawa, S.; Kondo, M.; Seki, K. *Angew. Chem. Int. Ed.* **2000**, *39*, 2084.
- (14) Kitagawa, S.; Kitaura, R.; Noro, S. *Angew. Chem. Int. Ed.* **2004**, *43*, 2334.
- (15) Batten, S. R.; Champness, N. R.; Chen, X.-M.; Garcia-Martinez, J.; Kitagawa, S.; Öhrström, L.; O'Keeffe, M.; Suh, M. P.; Reedijk, J. *CrystEngComm*, **2012**, *14*, 3001.
- (16) Liu, C. F.; Liu, N. C.; Bailar Jr, J. C. *Inorg. Chem.* **1964**, *3*, 1085.
- (17) Seddon, K. R.; Zaworotko, M. *Crystal engineering: The design and application of functional solids*; Springer Science & Business Media, **1999**; 539.
- (18) Leong, W. L.; Vittal, J. J. *Chem. Rev.* **2011**, *111*, 2, 688.
- (19) Robin, A. Y.; Fromm, K. M. *Coordin Chem Rev.* **2006**, *250*, 2127.
- (20) Uemura, K.; Kitagawa, S.; Fukui, K.; Saito, K. *J. Am. Chem. Soc.* **2004**, *126*, 3817.
- (21) Spichal, Z.; Necas, M.; Pinkas, J.; Novosad, J. *Inorg. Chem.* **2004**, *43*, 2776.
- (22) Kitaura, R.; Seki, K.; Akiyama, G.; Kitagawa, S. *Angew. Chem. Int. Ed.* **2003**, *42*, 428.
- (23) Hijikata, Y.; Horike, S.; Sugimoto, M.; Inukai, M.; Fukushima, T.; Kitagawa, S. *Inorg. Chem.* **2013**, *52*, 3634.
- (24) Kanoo, P.; Matsuda, R.; Kitaura, R.; Kitagawa, S.; Maji, T. K. *Inorg. Chem.* **2012**, *51*, 9141.
- (25) Foo, M. L.; Matsuda, R.; Hijikata, Y.; Krishna, R.; Sato, H.; Horike, S.; Hori, A.; Duan, J.; Sato, Y.; Kubota, Y.; Takata, M.; Kitagawa, S. *J. Am. Chem. Soc.* **2016**, *138*, 3022.
- (26) Eddaoudi, M.; Li, H.; Yaghi, O. M. *J. Am. Chem. Soc.* **2000**, *122*, 1391.
- (27) Férey, G.; Mellot-Draznieks, C.; Serre, C.; Millange, F.; Dutour, J.; Surlblé, S.; Margiolaki, I. *Science* **2005**, *309*, 2040.
- (28) Furukawa, H.; Go, Y. B.; Ko, N.; Park, Y. K.; Uribe-Romo, F. J.; Kim, J.; O'Keeffe, M.; Yaghi, O. M. *Inorg. Chem.* **2011**, *50*, 9147.
- (29) Furukawa, H.; Ko, N.; Go, Y. B.; Aratani, N.; Choi, S. B.; Choi, E.; Yazaydin, A. O.; Snurr, R. Q.; O'Keeffe, M.; Kim, J.; Yaghi, O. M. *Science* **2010**, *329*, 424.
- (30) Farha, O. K.; Eryazici, I.; Jeong, N. C.; Hauser, B. G.; Wilmer, C. E.; Sarjeant, A. A.; Snurr, R. Q.; Nguyen, S. T.; Yazaydin, A. O.; Hupp, J. T. *J. Am. Chem. Soc.* **2012**, *134*, 15016.
- (31) Li, J. R.; Kuppler, R. J.; Zhou, H. C. *Chem. Soc. Rev.*, **2009**, *38*, 1477.
- (32) Farha, O. K.; Eryazici, I.; Jeong, N. C.; Hauser, B. G.; Wilmer, C. E.; Sarjeant, A. A.; Snurr, R. Q.; Nguyen, S. T.; Yazaydin, A. O.; Hupp, J. T. *J. Am. Chem. Soc.* **2012**, *134*, 15016.
- (33) D'Alessandro, D. M.; Smit, B.; Long, J. R. *Angew. Chem. Int. Ed. Engl.* **2010**, *49*, 6058.
- (34) Li, J. R.; Sculley, J.; Zhou, H. C. *Chem. Rev.* **2012**, *112*, 869.

- (35) Bachman, J. E.; Smith, Z. P.; Li, T.; Xu, T.; Long, J. R. *Nat. Mater* **2016**, *15*, 845.
- (36) Lee, J.; Farha, O. K.; Roberts, J.; Scheidt, K. A.; Nguyen, S. T.; Hupp, J. T. *Chem. Soc. Rev.*, **2009**, *38*, 1450.
- (37) Falkowski, J. M.; Liu, S.; Lin, W. B. *Isr. J. Chem.* **2012**, *52*, 591.
- (38) Horcajada, P.; Gref, R.; Baati, T.; Allan, P. K.; Maurin, G.; Couvreur, P.; Férey, G.; Morris, R. E.; Serre, C. *Chem. Rev.* **2012**, *112*, 1232.
- (39) So, M. C.; Wiederrecht, G. P.; Mondloch, J. E.; Hupp, J. T.; Farha, O. K. *Chem. Commun.*, **2015**, *51*, 3501.
- (40) Williams, D. E.; Shustova, N. B. *Chem. Eur. J.* **2015**, *21*, 15474.
- (41) Kreno, L. E.; Leong, K.; Farha, O. K.; Allendorf, M.; Van Duyne, R. P.; Hupp, J. T. *Chem. Rev.* **2012**, *112*, 1105.
- (42) Chen, Q.; Sun, J.; Li, P.; Hod, I.; Moghadam, P. Z.; Kean, Z. S.; Snurr, R. Q.; Hupp, J. T.; Farha, O. K.; Stoddart, J. F. *J. Am. Chem. Soc.* **2016**, *138*, 14242.
- (43) Zhao, X.; Bu, X.; Wu, T.; Zheng, S.-T.; Wang, L.; Feng, P. *Nat. Commun.* **2013**, *4*, 2344.
- (44) DeCoste, J. B.; Peterson, G. W. *Chem. Rev.* **2014**, *114*, 5695.
- (45) Howarth, A. J.; Liu, Y. Y.; Hupp, J. T.; Farha, O. K. *CrystEngComm*, **2015**, *17*, 7245.
- (46) AbdulHalim, R. G.; Shkurenko, A.; Alkordi, M. H.; Eddaoudi, M. *Cryst Growth Des.* **2016**, *16*, 722.
- (47) Stock, N.; Biswas, S. *Chem. Rev.* **2012**, *112*, 933.
- (48) Meek, S. T.; Greathouse, J. A.; Allendorf, M. D. *Adv. Mater.* **2011**, *23*, 249.
- (49) Uzarevic, K.; Wang, T. C.; Moon, S.-Y.; Fidelli, A. M.; Hupp, J. T.; Farha, O. K.; Frišćić, T. *Chem. Commun.*, **2016**, *52*, 2133.
- (50) Rabenau, A. *Angew. Chem. Int. Ed. Engl.* **1985**, *24*, 1026.
- (51) Stock, N.; Biswas, S. *Chem. Rev.* **2012**, *112*, 933.
- (52) Carrington, E. J.; McAnally, C. A.; Fletcher, A. J.; Thompson, S. P.; Warren, M.; Brammer, L. *Nat. Chem.* **2017**, *9*, 8.
- (53) O'Keeffe, M.; Peskov, M. A.; Ramsden, S. J.; Yaghi, O. M. *Acc. Chem. Res.* **2008**, *41*, 1782.
- (54) Cook, T. R.; Zheng, Y.-R.; Stang, P. J. *Chem. Rev.* **2013**, *113*, 734.
- (55) Lu, W.; Wei, Z.; Gu, Z.-Y.; Liu, T.-F.; Park, J.; Park, J.; Tian, J.; Zhang, M.; Zhang, Q.; Gentle Iii, T.; Bosch, M.; Zhou, H.-C. *Chem. Soc. Rev.*, **2014**, *43*, 5561.
- (56) Eddaoudi, M.; Moler, D. B.; Li, H.; Chen, B.; Reineke, T. M.; O'Keeffe, M.; Yaghi, O. M. *Acc. Chem. Res.* **2001**, *34*, 319.
- (57) Eddaoudi, M.; Kim, J.; Rosi, N.; Vodak, D.; Wachter, J.; O'Keeffe, M.; Yaghi, O. M. *Science* **2002**, *295*, 469.
- (58) James, S. L. *Chem. Soc. Rev.*, **2003**, *32*, 276.
- (59) Qiu, S.; Zhu, G. *Coordin Chem Rev* **2009**, *253*, 2891.
- (60) Deng, H.; Doonan, C. J.; Furukawa, H.; Ferreira, R. B.; Towne, J.; Knobler, C. B.; Wang, B.; Yaghi, O. M. *Science* **2010**, *327*, 846.
- (61) Li, M.; Li, D.; O'Keeffe, M.; Yaghi, O. M. *Chem. Rev.* **2014**, *114*, 1343.
- (62) Li, H.; Eddaoudi, M.; O'Keeffe, M.; Yaghi, O. M. *Nature* **1999**, *402*, 276.
- (63) Tranchemontagne, D. J.; Mendoza-Cortes, J. L.; O'Keeffe, M.; Yaghi, O. M. *Chem. Soc. Rev.*, **2009**, *38*, 1257.
- (64) Yaghi, O. M.; O'Keeffe, M.; Ockwig, N. W.; Chae, H. K.; Eddaoudi, M.; Kim, J. *Nature*. **2003**, *423*, 705.
- (65) Deng, H.; Doonan, C. J.; Furukawa, H.; Ferreira, R. B.; Towne, J.; Knobler, C. B.; Wang, B.; Yaghi, O. M. *Science* **2010**, *327*, 846.

- (66) Bezuidenhout, C. X.; Smith, V. J.; Esterhuysen, C.; Barbour, L. J. *J. Am. Chem. Soc.* **2017**, *139*, 5923.
- (67) Bezuidenhout, C. X.; Smith, V. J.; Bhatt, P. M.; Esterhuysen, C.; Barbour, L. J. *Angew. Chem. Int. Ed.* **2015**, *54*, 2079.
- (68) Maity, D. K.; Halder, A.; Bhattacharya, B.; Das, A.; Ghoshal, D. *Cryst. Growth Des.* **2016**, *16*, 1162.
- (69) Barbour, L. J. *Chem. Commun.*, **2006**, 1163.
- (70) Sing, K. S. W. *Journal of Colloid and Interface Science.* **1998**, *3*, 77.
- (71) Barbour, L. J. *Chem. Commun.*, **2006**, 1163.
- (72) Donohue, M. D.; Aranovich, G. L. *Journal of Colloid and Interface Science.* **1998**, *205*, 121.
- (73) Sing, K. S. W. In *Pure and Applied Chemistry.* **1985**; *57*, 603.
- (74) Brunauer, S.; Deming, L. S.; Deming, W. E.; Teller, E. *J. Am. Chem. Soc.* **1940**, *62*, 1723.
- (75) Culp, J. T.; Smith, M. R.; Bittner, E.; Bockrath, B. *J. Am. Chem. Soc.* **2008**, *130*, 12427.
- (76) Uemura, K.; Matsuda, R.; Kitagawa, S. *J. Solid State Chem.* **2005**, *178*, 2420.
- (77) Horike, S.; Shimomura, S.; Kitagawa, S. *Nat. Chem.* **2009**, *1*, 695.
- (78) Férey, G. *New J. Chem.* **2016**, *40*, 3950.
- (79) Kitagawa, S.; Matsuda, R. *Coord Chem Rev.* **2007**, *251*, 2490.
- (80) Uemura, K.; Kitagawa, S.; Kondo, M.; Fukui, K.; Kitaura, R.; Chang, H.-C.; Mizutani, T. *Chem. Eur. J.* **2002**, *8*, 3586.
- (81) Sakata, Y.; Furukawa, S.; Kondo, M.; Hirai, K.; Horike, N.; Takashima, Y.; Uehara, H.; Louvain, N.; Meilikhov, M.; Tsuruoka, T.; Isoda, S.; Kosaka, W.; Sakata, O.; Kitagawa, S. *Science* **2013**, *339*, 193.
- (82) McDonald, T. M.; Mason, J. A.; Kong, X.; Bloch, E. D.; Gygi, D.; Dani, A.; Crocella, V.; Giordanino, F.; Odoh, S. O.; Drisdell, W. S.; Vlaisavljevich, B.; Dzubak, A. L.; Poloni, R.; Schnell, S. K.; Planas, N.; Lee, K.; Pascal, T.; Wan, L. F.; Prendergast, D.; Neaton, J. B.; Smit, B.; Kortright, J. B.; Gagliardi, L.; Bordiga, S.; Reimer, J. A.; Long, J. R. *Nature* **2015**, *519*, 303.
- (83) Yang, Q.-Y.; Lama, P.; Sen, S.; Lusi, M.; Chen, K.-J.; Gao, W.-Y.; Shivanna, M.; Pham, T.; Hosono, N.; Kusaka, S.; Perry, J. J.; Ma, S.; Space, B.; Barbour, L. J.; Kitagawa, S.; Zaworotko, M. J. *Angew. Chem. Int. Ed.* **2018**, *57*, 5684.
- (84) Schneemann, A.; Bon, V.; Schwedler, I.; Senkovska, I.; Kaskel, S.; Fischer, R. A. *Chem. Soc. Rev.* **2014**, *43*, 6062.
- (85) Bousquet, D.; Coudert, F. X.; Fossati, A. G.; Neimark, A. V.; Fuchs, A. H.; Boutin, A. *J. Chem. Phys.* **2013**, *138*, 174706.
- (86) Lama, P.; Aggarwal, H.; Bezuidenhout, C. X.; Barbour, L. J. *Angew. Chem. Int. Ed.* **2016**, *55*, 13271; *Angew. Chem.* **2016**, *128*, 13465.
- (87) Krause, S.; Bon, V.; Senkovska, I.; Stoeck, U.; Wallacher, D.; Töbrens, D. M.; Zander, S.; Pillai, R. S.; Maurin, G.; Coudert, F. o.-X.; Kaskel, S. *Nature* **2016**, *532*, 348.
- (88) Schneemann, A.; Bon, V.; Schwedler, I.; Senkovska, I.; Kaskel, S.; Fischer, R. A. *Chem. Soc. Rev.* **2014**, *43*, 6062.
- (89) Serre, C.; Bourrelly, S.; Vimont, A.; Ramsahye, N. A.; Maurin, G.; Llewellyn, P. L.; Daturi, M.; Filinchuk, Y.; Leynaud, O.; Barnes, P.; Férey, G. *Adv. Mater.* **2007**, *19*, 2246.
- (90) Bourrelly, S.; Llewellyn, P. L.; Serre, C.; Millange, F.; Loiseau, T.; Férey, G. *J. Am. Chem. Soc.* **2005**, *127*, 13519.
- (91) Llewellyn, P. L.; Bourrelly, S.; Serre, C.; Filinchuk, Y.; Férey, G. *Angew. Chem. Int. Ed.* **2006**, *45*, 7751.
- (92) Serre, C.; Millange, F.; Surblé, S.; Férey, G. *Angew. Chem. Int. Ed.* **2004**, *43*, 6285.
- (93) Chen, L.; Mowat, J. P. S.; Fairen-Jimenez, D.; Morrison, C. A.; Thompson, S. P.; Wright, P. A.; Düren, T. *J. Am. Chem. Soc.* **2013**, *135*, 15763.

- (94) Coudert, F. X.; Boutin, A.; Jeffroy, M.; Mellot-Draznieks, C.; Fuchs, A. H. *ChemPhysChem*. **2011**, *12*, 247.
- (95) Coudert, F. X.; Mellot-Draznieks, C.; Fuchs, A. H.; Boutin, A. *J. Am. Chem. Soc.* **2009**, *131*, 11329.
- (96) Ghoufi, A.; Subercaze, A.; Ma, Q.; Yot, P. G.; Ke, Y.; Puente-Orench, I.; Devic, T.; Guillerm, V.; Zhong, C.; Serre, C.; Férey, G.; Maurin, G. *J. Phys. Chem.* **2012**, *116*, 13289.
- (97) Dybtsev, D. N.; Chun, H.; Kim, K. *Angew. Chem.* **2004**, *116*, 5143.
- (98) Aggarwal, H.; Bhatt, P. M.; Bezuidenhout, C. X.; Barbour, L. J. *J. Am. Chem. Soc.* **2014**, *136*, 3776.
- (99) Morris, R. E.; Brammer, L. *Chem. Soc. Rev.* **2017**.
- (100) Kanoo, P.; Matsuda, R.; Higuchi, M.; Kitagawa, S.; Maji, T. K. *Chem. Mater.* **2009**, *21*, 5860.
- (101) Mulfort, K. L.; Farha, O. K.; Malliakas, C. D.; Kanatzidis, M. G.; Hupp, J. T. *Chem. Eur. J.* **2010**, *16*, 276.
- (102) Seo, J.; Bonneau, C.; Matsuda, R.; Takata, M.; Kitagawa, S. *J. Am. Chem. Soc.* **2011**, *133*, 9005.
- (103) Zheng, Y.; Sato, H.; Wu, P.; Jeon, H. J.; Matsuda, R.; Kitagawa, S. *Nat. Commun.* **2017**, *8*, 100.
- (104) Seo, J.; Bonneau, C.; Matsuda, R.; Takata, M.; Kitagawa, S. *J. Am. Chem. Soc.* **2011**, *133*, 9005.
- (105) Dybtsev, D. N.; Chun, H.; Kim, K. *Angew. Chem. Int. Ed.* **2004**, *43*, 5033.
- (106) Engel, E. R.; Jouaiti, A.; Bezuidenhout, C. X.; Hosseini, M. W.; Barbour, L. J. *Angew. Chem. Int. Ed.* **2017**, *56*, 8874; *Angew. Chem.* **2017**, *129*, 9000.
- (107) Schneemann, A.; Vervoorts, P.; Hante, I.; Tu, M.; Wannapaiboon, S.; Sternemann, C.; Paulus, M.; Wieland, D. C. F.; Henke, S.; Fischer, R. A. *Chem. Mater.* **2018**, *30*, 1667.
- (108) Henke, S.; Schneemann, A.; Wütscher, A.; Fischer, R. A. *J. Am. Chem. Soc.* **2012**, *134*, 9464.
- (109) Shivanna, M.; Yang, Q. Y.; Bajpai, A.; Sen, S.; Hosono, N.; Kusaka, S.; Pham, T.; Forrest, K. A.; Space, B.; Kitagawa, S.; Zaworotko, M. J. *Sci Adv* **2018**, *4*, eaaq1636.
- (110) Bhatt, P. M.; Batisai, E.; Smith, V. J.; Barbour, L. J. *Chem. Commun.*, **2016**, *52*, 11374.
- (111) Lama, P.; Barbour, L. J. *J. Am. Chem. Soc.* **2018**, *140*, 2145.
- (112) Carrington, E. J.; Vitorica-Yrezabal, I. J.; Brammer, L. *Acta Cryst.* **2014**, *B70*, 404.

CHAPTER 2

Direct *in situ* Crystallographic Visualization of a Dual Mechanism for Uptake of CO₂ Gas by a Flexible MOF

2.1. Manuscript submitted to *Inorganic Chemistry*

Contributions of the author:

- ✓ Design of project
- ✓ Preparation of the new MOF
- ✓ Collection of single-crystal X-ray data and gas cell work
- ✓ Solution and refinement of single-crystal X-ray structure with Len
- ✓ Recording of PXRD patterns
- ✓ Recording of TGA thermograms
- ✓ Sorption analysis with Len
- ✓ Interpretation of results with Charl X. Bezuidenhout and Dewald P. van Heerden and Len
- ✓ Writing the first draft of the article

Direct *in situ* Crystallographic Visualization of a Dual Mechanism for Uptake of CO₂ Gas by a Flexible MOF

Phumile Sikiti, Charl X. Bezuidenhout, Dewald P. van Heerden and Leonard J. Barbour*

Department of Chemistry and Polymer Science, University of Stellenbosch, Matieland 7602, South Africa

Supporting Information Placeholder

We report a flexible MOF [Co₂(OBA)₂(BPMP)]_n (**COB**), with a new network topology. **COB** displays structural flexibility under CO₂ gas pressure at 298 K and the resultant porous phases have been characterized by *in situ* X-ray diffraction analysis. We show that activation yields a framework with discrete voids and substantial reduction in guest-accessible volume. Single-crystal diffraction analysis under controlled CO₂ pressure shows that **COB** exhibits a breathing mode of flexibility, combined with an overall swelling of the framework. This combination of mechanisms is highly unusual.

Porous metal–organic frameworks (MOFs) are investigated intensively for numerous applications such as molecular sensing, drug delivery and gas separations.¹ Apart from their robust nature and high surface areas,² some MOFs display structural flexibility in response to external stimuli such as light, heat, and pressure.³ It is of particular interest that flexible MOFs can distort or even change phase under gas pressure to selectively absorb more gas.^{1d,4} Flexibility in MOFs is categorized into different modes such as breathing (ligand twisting, tilting and stretching), swelling (expansion in all directions without a change of unit cell shape and space group), linker rotation, subnetwork displacement (in catenated MOFs), and slippage of interdigitated and stacked layers.^{4a,6} These modes of flexibility generally yield stepped sorption profiles where each step is associated with a phase-change.⁷ The earliest examples of flexible MOFs that exhibit such phase-change behavior under gas pressure are the flexible MIL (Materials of Institute Lavoisier) family of MOFs ([M(X)(BDC)], where M is trivalent Al, Cr, Fe or Ga and X is OH⁻ or F⁻).⁸ Owing to the difficulty of producing large single crystals, the phase change behavior in the MIL series has mostly been characterized by synchrotron powder X-ray diffraction analysis (PXRD) and computational simulation.^{8a,8c,8f,9}

MOFs based on mixed ditopic ligands such as bis-tetrazolates or bipyridyls, combined with dicarboxylates, have recently been shown to yield phase-change behavior (flexibility) in response to gas pressure.^{4a,10} Such flexible MOFs have also been characterized extensively by means of *in situ* PXRD under non-ambient conditions, with support from theoretical studies to elucidate the phase-change behavior.¹¹ However, direct visualization of pressure-induced structural changes still poses significant experimental challenges. If crystals can remain intact during activation and subsequent gas loading, *in situ* single-crystal X-ray diffraction (SCD) experiments can be carried out for crystals in controlled environments¹² using an environmental gas cell.^{3a,5b,13} Unequivocal structural information can then be used to study the

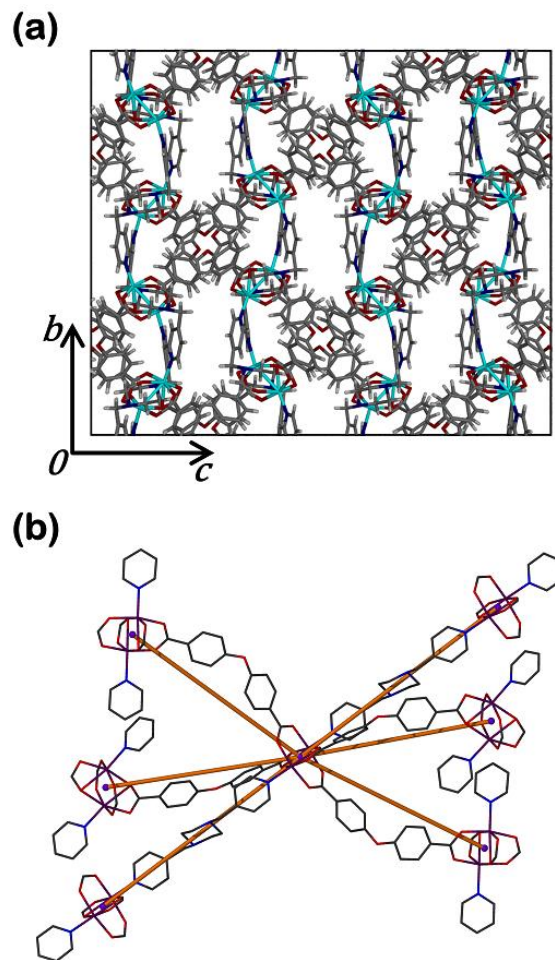


Figure 1. (a) Perspective view of **COB-DMF** projected along [100] (guest molecules not modelled) and (b) connectivity of each 6-connected node to form a 3D net.

dynamic structural moieties that give rise to the phase change events. Although structural transformations due to breathing and swelling have been reported separately, we are not aware of any instances where these processes occur concurrently within the same framework. We now report a dual mechanism for gas uptake by a new non-interpenetrated flexible MOF, {[Co₂(OBA)₂(BPMP)]·1.5(DMF)}_n (**COB-DMF**), where OBA = 4,4'-oxybis(benzoic acid), BPMP = 4-bis(pyridin-4-ylmethyl)piperazine and DMF = dimethylformamide.

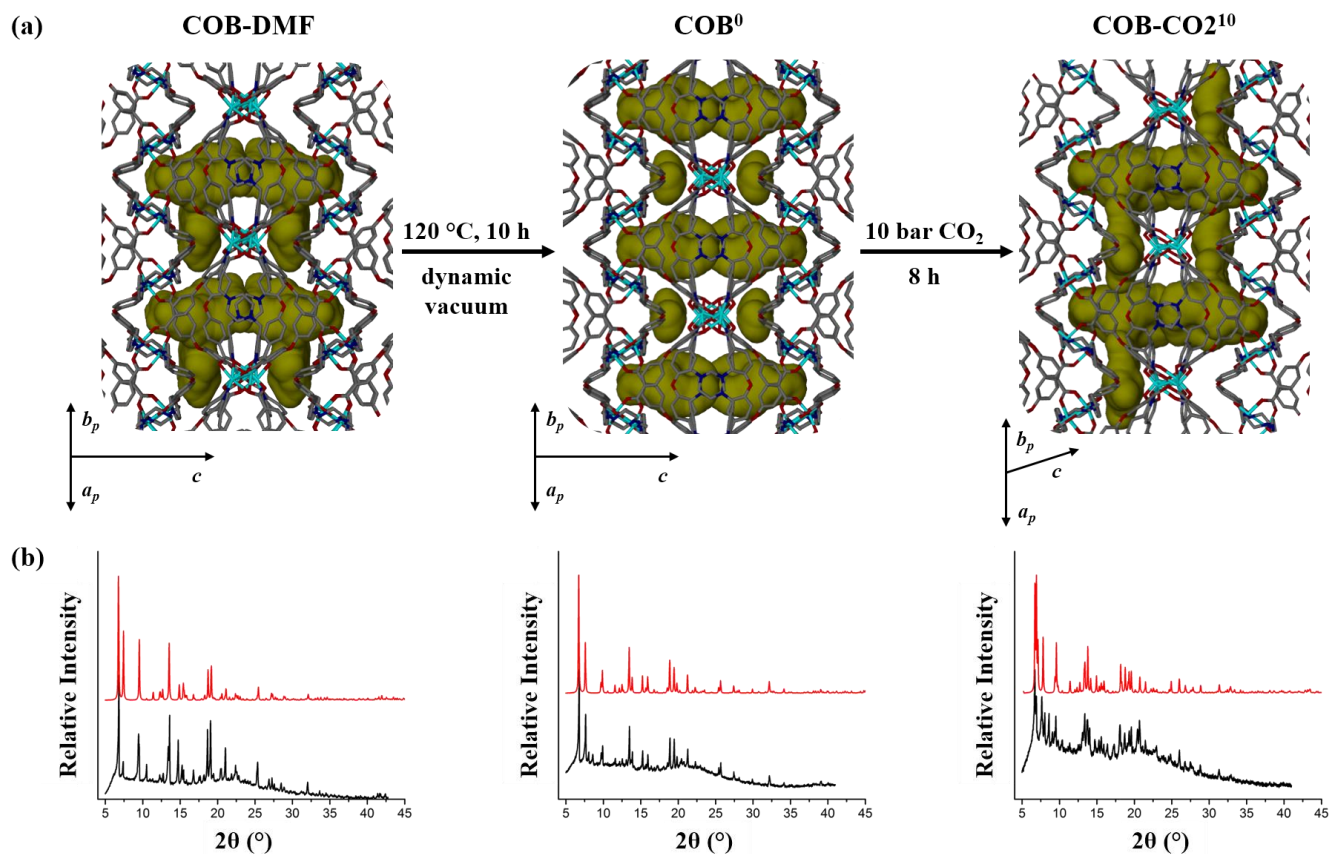


Figure 2. (a) Projections of **COB-DMF**, **COB⁰** and **COB-CO₂¹⁰**, showing the reduction in the guest-accessible space (yellow surfaces) upon activation, followed by expansion of the space upon CO₂ loading. (b) PXRD diffractograms of the corresponding phases recorded at 298 K (black) and simulated from SCD structures (red). The SCD structure of **COB-DMF** was determined at 100 K while those of **COB⁰** and **COB-CO₂¹⁰** were determined at 298 K.

Red prismatic crystals of **COB-DMF** were prepared according to the procedure outlined in Scheme S1 and subjected to SCD analysis at 100 K. **COB-DMF** crystallizes in the space group *F2dd* (Table S1) and the structure consists of a 3D non-interpenetrated network with Co₂OBA₂ paddlewheel nodes (Figures 1a and S1a). The paddlewheel units are linked axially by means of BPMP bridges to form [Co₂(OBA)₂(BPMP)]_n (Figure 1a). Each network node consists of two Co(II) ions surrounded by four OBA²⁻ and two BPMP ligands to form a 6-connected secondary building unit, and the 3D net can thus be rationalized as a new 6-connected uninodal net (Figure 1b) with the point symbol 4⁶6⁷7², which has been assigned the code sus01.¹⁴ Although the guest solvent could not be modelled, **COB-DMF** contains discrete ‘mushroom-shaped’ solvent-accessible virtual voids,¹⁵ each with a volume of approximately 416 Å³ (estimated by MSROLL¹⁶ using a probe radius of 1.4 Å; see Figure 2a, left). Since **COB-DMF** packs in a polar space group the cavities are oriented in a parallel fashion and stacked along [100]. The guest-accessible volume represents approximately 18.5% of the total volume. Phase purity of the bulk material was confirmed by PXRD analysis (i.e. the simulated PXRD pattern corresponds to that measured for the bulk material, as shown in Figure 2b, left).

Thermogravimetric analysis (TGA) of **COB-DMF** shows a weight loss of approximately 17% in the range 25 to 200 °C, which corresponds to 1.5 DMF guest molecules per host formula unit. This value is also in excellent agreement with Rebek’s 55% solution¹⁷ to accommodating DMF in the available space (see the

Supporting Information (SI) for details). Since the framework decomposes after 350 °C (Figure S2), a bulk sample of **COB-DMF** was activated at 120 °C under dynamic vacuum (3.1×10^{-2} mbar) for 10 hours. PXRD analysis under ambient conditions confirmed conversion to a new phase **COB-act** upon desolvation (Figure S3a). A single crystal was selected from the bulk activated sample and placed in an environmental gas cell, which was then evacuated (3.1×10^{-2} mbar) at room temperature. The crystal retains its singularity and we were thus able to determine its structure under vacuum (**COB⁰**) at 298 K. The simulated PXRD pattern of **COB⁰** is comparable to that recorded for **COB-act** (Figure S3a). Although the network connectivity remains intact upon activation, the space group changes from *F2dd* (**COB-DMF**) to *Fddd* (**COB-act** and **COB⁰**) (Table S1). Moreover, the two lobes of each cavity split apart to form two crystallographically unique ellipsoidal voids that alternate along [100] (volumes of 245 and 59 Å³; see Figure 2a, center). This involves a 27% decrease in total solvent-accessible volume upon activation, and a centrosymmetric arrangement of guest-accessible pockets.

Although **COB⁰** does not contain permanent pores, it is known that many such materials are still capable of adsorbing guest molecules.¹⁵ To explore the porosity of **COB⁰**, gas sorption analyses were carried out at 298 K using CO₂ (Figure 3) and N₂ (Figure S4) up to pressures of 50 bar. The type I sorption isotherm for N₂ shows a maximum loading of 0.5 molecules per host formula unit at 50 bar. However, the CO₂ sorption isotherm contains two

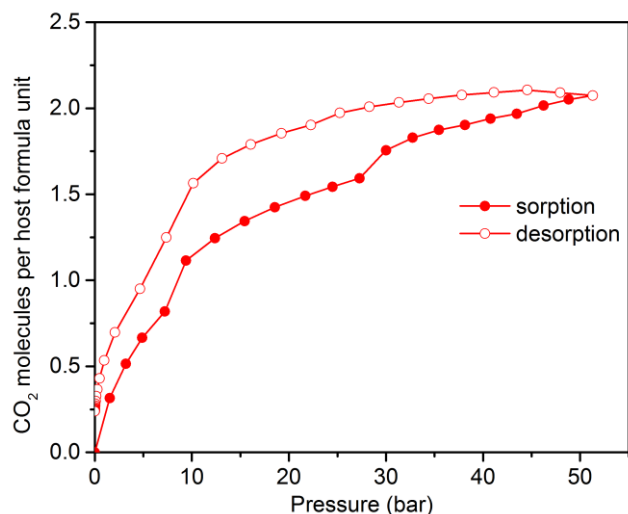


Figure 3. CO₂ sorption/desorption isotherm for **COB** recorded at 298 K.

noticeable inflections. The first step occurs with an onset pressure (P_{on}) of approximately 7 bar, where the CO₂ uptake is 0.75 molecules per host formula unit. Upon further increase in pressure, additional CO₂ is absorbed before the second step occurs with $P_{on} \approx 25$ bar (1.5 CO₂ molecules per host formula unit), with apparent saturation being reached at 50 bar, where the total uptake is two molecules of CO₂ per host formula unit. The sorption and desorption processes display moderate hysteresis.

Stepped sorption profiles usually indicate gas-induced phase transitions that provide additional guest-accessible space and enhanced sorption.¹⁸ To investigate the possibility of two CO₂ induced phase changes, variable-pressure PXRD (VP-PXRD) analyses were carried out at 298 K using an environmental gas cell. A polycrystalline sample of **COB**⁰ was pressurized incrementally with CO₂ gas and diffractograms were recorded at various pressures in the range 0 to 50 bar (Figures 4 and S3b). The PXRD patterns at 0, 1 and 7.5 bar are similar to one another. However, at 10 bar new peaks appear at low 2θ values, thus indicating a phase change, and it appears that this new phase persists until 50 bar. The VP-PXRD results imply that the first step in the sorption isotherm is associated with a structural change, while the second step is not. To gain mechanistic insight into the stepped CO₂ gas sorption profile, we also carried out structural characterization by means of variable-pressure SCD (VP-SCD).

A series of VP-SCD analyses was carried out at 298 K for a single crystal of **COB**⁰ exposed to various CO₂ gas pressures (0, 3, 10, 14, 18, 22, 30 and 35 bar) within an environmental gas cell¹³ (Table S1). Despite lower reflection intensities as compared to the data for **COB**⁰ and **COB-CO2**³ (before the phase change), it was possible to determine the crystal structures of **COB-CO2**^x, where $x = 10, 14, 18, 22, 30$ and 35 (Table S1). The transformation from **COB-CO2**³ to **COB-CO2**¹⁰ involves a change of space group to $C2/c$. In agreement with the VP-PXRD results, no further phase changes are observed in the range 10 to 35 bar. Although the host structure and connectivity of the $Fddd$ and $C2/c$ phases still resemble those of **COB-DMF**, the configurations of the guest-accessible spaces are different in the three structures (Figure 2a). During the CO₂-induced phase transition the alternating voids observed in **COB**⁰ become fused to once again form mushroom-shaped pockets, but in antiparallel stacks along [010]. Although it was not possible to model the guest CO₂ molecules in the guest-

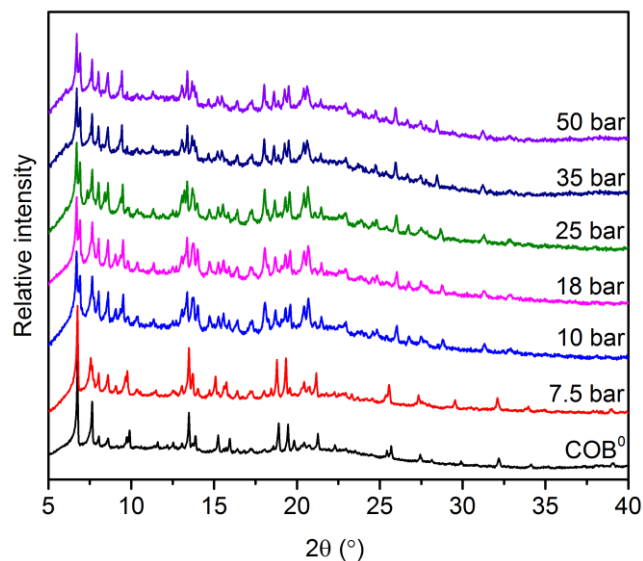


Figure 4. VP-PXRD diffractograms for **COB** exposed to various controlled CO₂ gas pressures, recorded at 298 K.

loaded crystal structures, we are provided with detailed structural information regarding the pressure-induced changes in the host framework. Note that none of the gas-loaded crystal structures exhibit permanent pores.

To understand the mechanism that governs the phase change behavior of **COB** it is useful to describe the structural moieties in simple geometric terms. We consider the Co-OBA-Co connectivity

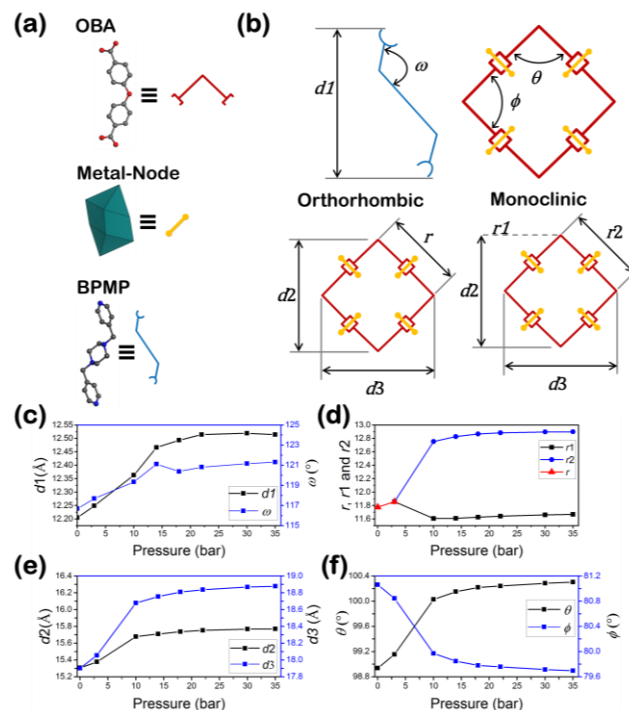


Figure 5. (a) The structural moieties OBA and BPMP can be represented as angled and spring-like linkers, respectively. (b) Relevant distances and angles that characterize the conversion of **COB** under CO₂ gas pressure. (c) – (f) Changes in the **COB** framework parameters with increasing CO₂ pressure.

of **COB** to resemble a rhombic network in the *Fddd* structure (before the phase change) and a parallelogram in the *C2/c* structures (after the phase change) (Figure 5a and 5b). The lengths of the quadrilateral edges are r , $r1$ and $r2$, while $d2$ and $d3$ represent the vertical and horizontal diagonals with θ and ϕ as the internal angles (see the SI for details). The nodes of the quadrilateral networks are connected by BPMP ligands, which are represented by a zig-zag ‘spring’ with length $d1$ and angle ω . Distance $d1$ increases rapidly from vacuum to 14 bar of CO₂ and this elongation becomes more gradual thereafter, while ω exhibits a decaying increase in magnitude up to 35 bar (Figure 5c). The rhombic edge length r increases before the first phase change and then splits into two unique edges $r1$ and $r2$ (due to lowering of crystallographic symmetry), thus representing a parallelogram. Notably, $r1$ decreases relative to r during the phase change (as determined at 10 bar) and then increases slightly at a slower rate with increasing pressure. Conversely, $r2$ increases relative to r (**COB-CO2**¹⁰) and then continues to increase in a deceleratory fashion towards 35 bar (Figure 5d). Although $r1$ decreases, the relatively large increase in $r2$ still results in an overall elongation of both of the parallelogram diagonals $d2$ and $d3$. Indeed, $d2$ and $d3$ increase rapidly during the phase change (as determined at 10 bar), and then increases gently thereafter (Figure 5e). Taken together, the above describes a symmetric swelling before the phase change, followed by asymmetric swelling up to 35 bar.

This mechanism precludes the type of trellis-like motion often observed for similar frameworks, where one diagonal elongates as the other shortens.^{5b} Moreover, the total change in $d2$ (ca 3%) is much lower than that of $d3$ (5%), and this can be explained by considering that $d1$ lies along the same direction as $d2$. The BPMP linker thus acts as a ‘spring’, stretching but also restraining the degree of deviation along $d2$ while leaving $d3$ unaffected. The parallelogram internal angles θ and ϕ exhibit unusual trellis-like behavior, where both of the parallelogram diagonals become elongated, but at different rates (Figure 5f). This mechanism contributes to the swelling caused by elongation of $d1$ with increasing pressure (see Supplementary Video S1).

In conclusion, **COB** is a new non-interpenetrated flexible MOF with a new topology. The guest-accessible space of the as-synthesized form consists of isolated voids that are occupied by DMF solvent molecules. Activation results in a significant reduction in guest-accessible space, where each void splits into two separate voids. The CO₂ sorption isotherm recorded at 298 K exhibits two distinct steps with onset pressures of approximately 7 and 25 bar, implying that two gas-induced phase changes may occur at these pressures. However, VP-PXRD and VP-SCD analyses (0 to 50 and 0 to 35 bar, respectively) show that only one phase change occurs in the pressure ranges investigated. The detailed structural information afforded by the SCD analysis reveals that the first step in the sorption isotherm involves a guest-induced phase change whereby the two unique guest-accessible cavities experience a sudden swelling. Thereafter, the cavities undergo a modest degree of swelling with further CO₂ uptake with little change in the structure of the host framework. In order to rationalize the stepped CO₂ uptake event at $P_{on} = 25$ bar, we postulate that cooperative phenomena arise as the cavities become filled. Importantly, our SCD analyses have shown that flexibility of the material occurs due to two distinct mechanisms: breathing (stretching of the BPMP ligands), together with swelling (an asymmetric trellis-like mechanism). Detailed structural studies involving complementary *in situ* techniques can advance our efforts to design new network topologies for useful applications that rely on pore-opening mechanisms.

ASSOCIATED CONTENT

Supporting Information

Synthetic procedure, TGA Analysis, detailed crystallographic information, and additional figures (PDF)

Single-crystal data in CIF format (CIF)

An animation of the phase change mechanism (S1.MP4)

AUTHOR INFORMATION

Corresponding Author

*E-mail: ljb@sun.ac.za.

Notes

The authors declare no competing financial interest.

ACKNOWLEDGMENT

We thank the National Research Foundation and Department of Science and Technology (SARCHI Program) for financial support.

REFERENCES

- (a) Kreno, L. E.; Leong, K.; Farha, O. K.; Allendorf, M.; Van Duyne, R. P.; Hupp, J. T. Metal–Organic Framework Materials as Chemical Sensors. *Chem. Soc. Rev.* **2012**, *112*, 1105–1125. (b) Horcajada, P.; Serre, C.; Vallet-Regí, M.; Sebba, M.; Taulelle, F.; Férey, G. Metal–Organic Frameworks as Efficient Materials for Drug Delivery. *Angew. Chem. Int. Ed.* **2006**, *45*, 5974–5978. *Angew. Chem.* **2006**, *118*, 6120–6124. (c) Horcajada, P.; Gref, R.; Baati, T.; Allan, P. K.; Maurin, G.; Couvreur, P.; Férey, G.; Morris, R. E.; Serre, C. Metal–Organic Frameworks in Biomedicine. *Chem. Rev.* **2012**, *112*, 1232–1268. (d) Li, J. R.; Sculley, J.; Zhou, H. C. Metal–Organic Frameworks for Separations. *Chem. Rev.* **2012**, *112*, 869–932.
- Farha, O. K.; Eryazici, I.; Jeong, N. C.; Hauser, B. G.; Wilmer, C. E.; Sarjeant, A. A.; Snurr, R. Q.; Nguyen, S. T.; Yazaydin, A. O.; Hupp, J. T. Metal–Organic Framework Materials with Ultrahigh Surface Areas: Is the Sky the Limit? *J. Am. Chem. Soc.* **2012**, *134*, 15016–15021.
- (a) Bhatt, P. M.; Batisai, E.; Smith, V. J.; Barbour, L. J. Creation of new guest accessible space under gas pressure in a flexible MOF: multidimensional insight through combination of *in situ* techniques. *Chem. Commun.* **2016**, *52*, 11374–11377. (b) Krause, S.; Bon, V.; Senkowska, I.; Stoeck, U.; Wallacher, D.; Többs, D. M.; Zander, S.; Pillai, R. S.; Maurin, G.; Coudert, F.-X.; Kaskel, S. A pressure-amplifying framework material with negative gas adsorption transitions. *Nature* **2016**, *532*, 348–352.
- (a) Schneemann, A.; Bon, V.; Schwedler, I.; Senkowska, I.; Kaskel, S.; Fischer, R. A. Flexible metal-organic frameworks. *Chem. Soc. Rev.* **2014**, *43*, 6062–6096. (b) Thallapally, P. K.; Tian, J.; Radha Kishan, M.; Fernandez, C. A.; Dalgarno, S. J.; McGrail, P. B.; Warren, J. E.; Atwood, J. L. Flexible (Breathing) Interpenetrated Metal–Organic Frameworks for CO₂ Separation Applications. *J. Am. Chem. Soc.* **2008**, *130*, 16842–16843. (c) Bezuidenhout, C. X.; Smith, V. J.; Esterhuysen, C.; Barbour, L. J. Solvent- and Pressure-Induced Phase Changes in Two 3D Copper Glutarate-Based Metal–Organic Frameworks via Glutarate (+gauche ⇌ -gauche) Conformational Isomerism. *J. Am. Chem. Soc.* **2017**, *139*, 5923–5929. (d) Zheng, Y.; Sato, H.; Wu, P.; Jeon, H. J.; Matsuda, R.; Kitagawa, S. Flexible interlocked porous frameworks allow quantitative photoisomerization in a crystalline solid. *Nat. Commun.* **2017**, *8*:100.
- (a) Henke, S.; Schneemann, A.; Wütscher, A.; Fischer, R. A. Directing the Breathing Behavior of Pillared–Layered Metal–

- Organic Frameworks via a Systematic Library of Functionalized Linkers Bearing Flexible Substituents. *J. Am. Chem. Soc.* **2012**, *134*, 9464-9474. (b) Lama, P.; Aggarwal, H.; Bezuidenhout, C. X.; Barbour, L. J. Giant Hysteretic Sorption of CO₂: In Situ Crystallographic Visualization of Guest Binding within a Breathing Framework at 298 K. *Angew. Chem. Int. Ed.* **2016**, *55*, 13271-13275; *Angew. Chem.* **2016**, *128*, 13465-13469.
6. (a) Bousquet, D.; Coudert, F.-X.; Fossati, A. G.; Neimark, A. V.; Fuchs, A. H.; Boutin, A. Adsorption induced transitions in soft porous crystals: An osmotic potential approach to multistability and intermediate structures. *J. Chem. Phys.* **2013**, *138*:174706. (b) Ortiz, A. U.; Boutin, A.; Fuchs, A. H.; Coudert, F.-X. Anisotropic Elastic Properties of Flexible Metal-Organic Frameworks: How Soft are Soft Porous Crystals? *Phys. Rev. Lett.* **2012**, *109*:195502. (c) Murdock, C. R.; Hughes, B. C.; Lu, Z.; Jenkins, D. M. Approaches for synthesizing breathing MOFs by exploiting dimensional rigidity. *Coord. Chem. Rev.* **2014**, *258*, 119-136.
 7. (a) McDonald, T. M.; Mason, J. A.; Kong, X.; Bloch, E. D.; Gygi, D.; Dani, A.; Crocellà, V.; Giordanino, F.; Odoh, S. O.; Drisdell, W. S.; Vlasisavljevich, B.; Dzubak, A. L.; Poloni, R.; Schnell, S. K.; Planas, N.; Lee, K.; Pascal, T.; Wan, L. F.; Prendergast, D.; Neaton, J. B.; Smit, B.; Kortright, J. B.; Gagliardi, L.; Bordiga, S.; Reimer, J. A.; Long, J. R. Cooperative insertion of CO₂ in diamine-appended metal-organic frameworks. *Nature* **2015**, *519*, 303-308. (b) Carrington, E. J.; McAnally, C. A.; Fletcher, A. J.; Thompson, S. P.; Warren, M.; Brammer, L. Solvent-switchable continuous-breathing behaviour in a diamondoid metal-organic framework and its influence on CO₂ versus CH₄ selectivity. *Nat. Chem.* **2017**, *9*, 882-889. (c) Yang, S.; Lin, X.; Lewis, W.; Suyetin, M.; Bichoutskaia, E.; Parker, J. E.; Tang, C. C.; Allan, D. R.; Rizkallah, P. J.; Hubberstey, P.; Champness, N. R.; Mark Thomas, K.; Blake, A. J.; Schröder, M. A partially interpenetrated metal-organic framework for selective hysteretic sorption of carbon dioxide. *Nat. Mater.* **2012**, *11*, 710-716 (d) Foo, M. L.; Matsuda, R.; Hijikata, Y.; Krishna, R.; Sato, H.; Horike, S.; Hori, A.; Duan, J.; Sato, Y.; Kubota, Y.; Takata, M.; Kitagawa, S. An Adsorbate Discriminatory Gate Effect in a Flexible Porous Coordination Polymer for Selective Adsorption of CO₂ over C₂H₂. *J. Am. Chem. Soc.* **2016**, *138*, 3022-3030.
 8. (a) Serre, C.; Bourrelly, S.; Vimont, A.; Ramsahye, N. A.; Maurin, G.; Llewellyn, P. L.; Daturi, M.; Filinchuk, Y.; Leynaud, O.; Barnes, P.; Férey, G. An Explanation for the Very Large Breathing Effect of a Metal-Organic Framework during CO₂ Adsorption. *Adv. Mater.* **2007**, *19*, 2246-2251. (b) Bourrelly, S.; Llewellyn, P. L.; Serre, C.; Millange, F.; Loiseau, T.; Férey, G. Different Adsorption Behaviors of Methane and Carbon Dioxide in the Isotypic Nanoporous Metal Terephthalates MIL-53 and MIL-47. *J. Am. Chem. Soc.* **2005**, *127*, 13519-13521. (c) Llewellyn, P. L.; Bourrelly, S.; Serre, C.; Filinchuk, Y.; Férey, G. How Hydration Drastically Improves Adsorption Selectivity for CO₂ over CH₄ in the Flexible Chromium Terephthalate MIL-53. *Angew. Chem. Int. Ed.* **2006**, *45*, 7751-7754. (d) Férey, G.; Mellot-Draznieks, C.; Serre, C.; Millange, F.; Dutour, J.; Surblé, S.; Margiolaki, I. A Chromium Terephthalate-Based Solid with Unusually Large Pore Volumes and Surface Area. *Science* **2005**, *309*, 2040-2042. (e) Serre, C.; Millange, F.; Surblé, S.; Férey, G. A Route to the Synthesis of Trivalent Transition-Metal Porous Carboxylates with Trimeric Secondary Building Units. *Angew. Chem. Int. Ed.* **2004**, *43*, 6285-6289. (f) Férey, G. Giant flexibility of crystallized organic-inorganic porous solids: facts, reasons, effects and applications. *New J. Chem.* **2016**, *40*, 3950-3967.
 9. (a) Chen, L.; Mowat, J. P. S.; Fairen-Jimenez, D.; Morrison, C. A.; Thompson, S. P.; Wright, P. A.; Düren, T. Elucidating the Breathing of the Metal-Organic Framework MIL-53(Sc) with ab Initio Molecular Dynamics Simulations and in Situ X-ray Powder Diffraction Experiments. *J. Am. Chem. Soc.* **2013**, *135*, 15763-15773. (b) Coudert, F.-X.; Boutin, A.; Jeffroy, M.; Mellot-Draznieks, C.; Fuchs, A. H. Thermodynamic Methods and Models to Study Flexible Metal-Organic Frameworks. *ChemPhysChem* **2011**, *12*, 247-258. (c) Coudert, F.-X.; Mellot-Draznieks, C.; Fuchs, A. H.; Boutin, A. Prediction of Breathing and Gate-Opening Transitions Upon Binary Mixture Adsorption in Metal-Organic Frameworks. *J. Am. Chem. Soc.* **2009**, *131*, 11329-11331 (d) Ghoufi, A.; Subercaze, A.; Ma, Q.; Yot, P. G.; Ke, Y.; Puente-Orench, I.; Devic, T.; Guillerme, V.; Zhong, C.; Serre, C.; Férey, G.; Maurin, G. Comparative Guest, Thermal, and Mechanical Breathing of the Porous Metal Organic Framework MIL-53(Cr): Computational Exploration Supported by Experiments. *J. Phys. Chem. C* **2012**, *116*, 13289-13295.
 10. S. Horike, S. Shimomura, Kitagawa, S. Soft porous crystals. *Nat. Chem.* **2009**, *1*, 695-704.
 11. Carrington, E. J.; Vitórica-Yrezábal, I. J.; Brammer, L. Crystallographic studies of gas sorption in metal-organic frameworks. *Acta Cryst.* **2014**, *B70*, 404-422.
 12. Morris, R. E.; Brammer, L. Coordination change, lability and hemilability in metal-organic frameworks. *Chem. Soc. Rev.* **2017**, *46*, 5444-5462.
 13. (a) Jacobs, T.; Lloyd, G. O.; Gertenbach, J. A.; Müller-Nedebock, K. K.; Esterhuysen, C.; Barbour, L. J. In Situ X-ray Structural Studies of a Flexible Host Responding to Incremental Gas Loading. *Angew. Chem. Int. Ed.* **2012**, *51*, 4913-4916 (b) Lama, P.; Barbour, L. J. Distinctive Three-Step Hysteretic Sorption of Ethane with In Situ Crystallographic Visualization of the Pore Forms in a Soft Porous Crystal. *J. Am. Chem. Soc.* **2018**, *140*, 2145-2150.
 14. Blatov, V. A.; Shevchenko, A. P.; Proserpio, D. M. Applied Topological Analysis of Crystal Structures with the Program Package ToposPro. *Cryst Growth Des.* **2014**, *14*, 3576-3586.
 15. Barbour, L. J. Crystal porosity and the burden of proof. *Chem. Commun.* **2006**, 1163-1168.
 16. (a) Connolly, M. L. The molecular surface package. *J. Mol. Graphics.* **1993**, *11*, 139-141. (b) There are no guidelines that dictate the choice of probe radii to determine guest-accessible volumes. Although it is reasonable to use a probe radius similar to the van der Waals radii of atoms at the extremities of potential guest molecules, the volume calculations utilize equilibrium position of atoms and do not take structural dynamics into account. We have therefore used a probe radius that is slightly smaller than the van der Waals radius of an oxygen atom.
 17. Mecozzi, S.; Rebek, J. The 55% Solution: A Formula for Molecular Recognition in the Liquid State. *Chem. Eur. J.* **1998**, *4*, 1016-1022.
 18. (a) Shivanna, M.; Yang, Q.; Bajpai, A.; Sen, S.; Hosono, N.; Kusaka, S.; Pham, T.; Forrest, K. A.; Space, B.; Kitagawa, S.; Zaworotko, M. J. Readily accessible shape-memory effect in a porous interpenetrated coordination network. *Sci. Adv.* **2018**, *4*:eaq1636. (b) Uemura, K.; Yamasaki, Y.; Komagawa, Y.; Tanaka, K.; Kita, H. Two-Step Adsorption/Desorption on a Jungle-Gym-Type Porous Coordination Polymer. *Angew. Chem. Int. Ed.* **2007**, *46*, 6662-6665. (c) Maji, T. K.; Mostafa, G.; Matsuda, R.; Kitagawa, S. Guest-Induced Asymmetry in a Metal-Organic Porous Solid with Reversible Single-Crystal-to-Single-Crystal Structural Transformation. *J. Am. Chem. Soc.* **2005**, *127*, 17152-17153. (d) Kondo, A.; Noguchi, H.; Carlucci, L.; Proserpio, D. M.; Ciani, G.; Kajiro, H.; Ohba, T.; Kanoh, H.; Kaneko, K. Double-Step Gas Sorption of a Two-Dimensional Metal-Organic Framework. *J. Am. Chem. Soc.* **2007**, *129*, 12362-12363. (e) Kano, P.; Sambhu, R.; Maji, T. P. Guest-Specific Double- or Single-Step Adsorption in a Flexible Porous Framework Based on a Mixed-Ligand System. *Inorg. Chem.* **2011**, *50*, 400-402.

2.2. SUPPORTING INFORMATION

Direct *in situ* Crystallographic Visualization of a Dual Mechanism for Uptake of CO₂ Gas by a Flexible MOF

1. Synthesis and characterization

Materials

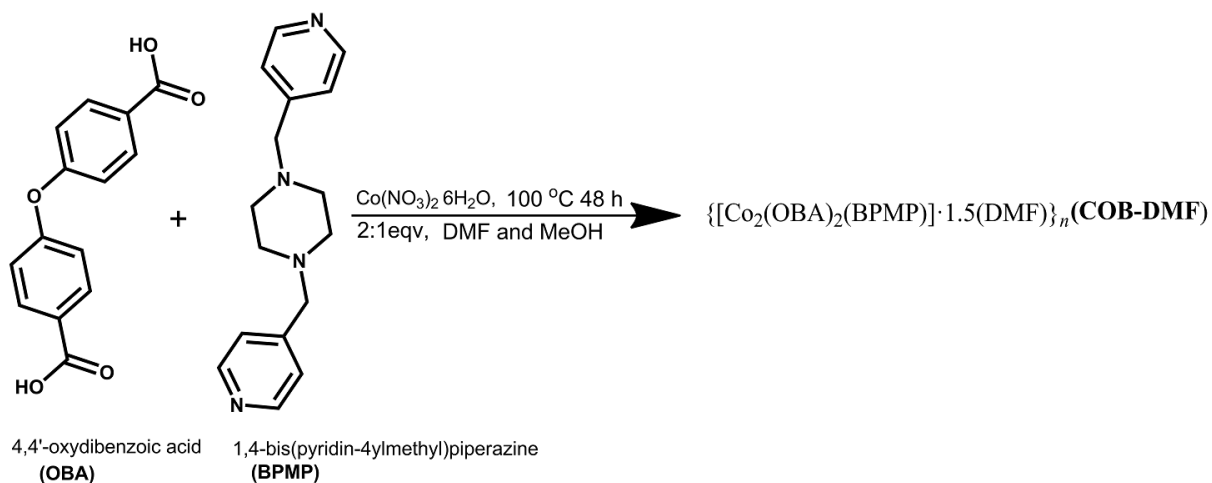
All chemicals and solvents were purchased from Aldrich and used without further purification.

Synthesis

The ligand 4-bis(pyridin-4-ylmethyl)piperazine was synthesized according to literature procedures.¹

MOF preparation

$\{[Co_2(OBA)_2(BPMP)] \cdot 1.5(DMF)}_n \cdot (COB-DMF)$ Co(NO₃)₂ (1 mmol), 4 4'-oxybis(benzoic acid acid (OBA, 1 mmol) and (4-bis(pyridin-4-ylmethyl)piperazine (BPMP, 1 mmol) were mixed in 2 ml methanol (MeOH) and 4 ml dimethylformamide (DMF) and placed in a pre-heated oven at 100 °C. The red block-shaped crystals were obtained after 48 h.



Scheme S1. Synthesis of $\{[Co_2(OBA)_2(BPMP)] \cdot 1.5(DMF)}_n \cdot (COB-DMF)$.

2. Methods

Thermogravimetric analysis (TGA)

Thermogravimetric analysis was carried out using a TA Instruments Q500 analyzer. The sample was loaded in an aluminum pan and heated at 10 °C/min from room temperature up to 600 °C.

Powder X-ray diffraction (PXRD)

Experiments were carried out on a PANalytical X'Pert PRO instrument in transmission mode. Intensity data were recorded using an X'Celerator detector and 2θ scans were performed in the range of 5-40°. During the experiment the powdered sample was exposed to Cu-K α radiation (λ = 1.5418 Å). Samples were sealed within a glass capillary (environmental gas cell) and the capillary spinner configuration (with focusing mirror) of the instrument was used since this setup allows for very accurate temperature control

using an Oxford Cryostream 700 Plus cryostat. Carbon dioxide was used to pressurize **COB** and its variable pressure PXRD patterns were measured at a constant temperature of 298 K.

Single-crystal X-ray diffraction (SCD)

Single crystal X-ray diffraction data were collected on a Bruker APEX-II Quasar CCD area-detector diffractometer equipped with an Oxford Cryostream 700Plus cryostat, and on a Bruker D8 venture PHOTON II CPAD detector equipped with an Oxford Cryostream 800Plus cryostat. A multilayer monochromator with $\text{MoK}\alpha$ radiation ($\lambda = 0.71073 \text{ \AA}$) from an Incoatec $\text{I}_{\mu\text{s}}$ microsource was used. Data reduction was carried out by means of standard procedures using the Bruker software package SAINT² and absorption corrections and the correction of other systematic errors were performed using SADABS.³ The structures were solved by direct methods using SHELXS-2016 and refined using SHELXL-2016⁴ and X-Seed⁵ was used as the graphical interface for the SHELX program suite. Hydrogen atoms were placed in calculated positions using riding models. All of the non-bonding distances and angles were measured using the program X-Seed⁵ and Diamond Version 3.0. Some of the figures were generated using OLEX2⁶ crystallographic software (version 1.2.9) and X-Seed/MSROLL.⁷

Environmental gas cell experiments:

An environmental gas cell (developed in-house) was used to determine the crystal structures of the various phases at 298 K under controlled pressures by means of single-crystal X-ray diffraction. First, crystals of **COB-DMF** were activated thermally under vacuum to yield **COB⁰**. **COB⁰** was activated in situ within the gas cell to remove any moisture before SCD analysis. The in situ activated structure of **COB⁰** was pressurized with 3 bar CO_2 and allowed to equilibrate for 8 hours before SCD analysis to yield **COB-CO2³**. Subsequent structures **COB-CO2¹⁰** to **COB-CO2³⁵** were determined in order after slowly pressurizing the previous sample to the appropriate pressure of CO_2 and allowing it to equilibrate for 8 hours. We note that R1 for the gas-loaded structures increases with pressure, and this is most likely due to increasing strain experienced by the crystals.

Volumetric Sorption Analysis

A Setaram PCTPro-E&E gas sorption analyser with MicroDoser attachment was utilised to conduct high pressure gas sorption experiments with gases such as N_2 and CO_2 at 298 K. The instrument is a volumetric gas analyser which utilises Sievert's volumetric method. The sample temperature was maintained to an accuracy of $\pm 1 \text{ }^\circ\text{C}$ using a Grant refrigerated recirculation bath filled with antifreeze and water. A sample at known pressure and volume was connected to a reservoir of known volume and pressure through an isolation valve. The valve was opened and the system allowed to equilibrate. The difference between the measured pressure and calculated pressure was used to determine the amount of gas adsorbed. NIST software was used to calculate the thermodynamic corrections in order to account for the non-ideal behaviour of the gases at relatively high pressures. The PCTPro-E&E with the MicroDoser attachment is used for small sample sizes and has a range of vacuum to 60 bar. Sample sizes of 100-120 mg were used and activated in-situ using vacuum and heat. Blank runs for each gas were recorded to further correct for any other residual systematic errors in the experiment. Figure preparation and data analyses were performed using Microsoft Excel and OriginPro.

3. Crystallographic tables and structural analysis

Table S1. Crystallographic table of COB-DMF, COB⁰, COB-CO2³, COB-CO2¹⁰, COB-CO2¹⁴, COB-CO2¹⁸, COB-CO2²², COB-CO2³⁰, and COB-CO2³⁵.

Complex	COB-DMF	COB ⁰	COB-CO2 ³	COB-CO2 ¹⁰	COB-CO2 ¹⁴	COB-CO2 ¹⁸	COB-CO2 ²²	COB-CO2 ³⁰	COB-CO2 ³⁵
Temperature (K)	100	298	298	298	298	298	298	298	298
Empirical formula	C _{48.5} H _{46.5} Co ₂ N _{4.5} O _{10.5}	C ₂₂ H ₁₈ CoNO ₅	C ₂₂ H ₁₈ CoNO ₅	C ₄₄ H ₃₆ Co ₂ N ₄ O ₁₀	C ₄₄ H ₃₆ Co ₂ N ₄ O ₁₀	C ₄₄ H ₃₆ Co ₂ N ₄ O ₁₀	C ₄₄ H ₃₆ Co ₂ N ₄ O ₁₀	C ₄₄ H ₃₆ Co ₂ N ₄ O ₁₀	C ₄₄ H ₃₆ Co ₂ N ₄ O ₁₀
Formula weight	992.27	449.31	449.31	898.63	898.63	898.63	898.63	898.63	898.63
Wavelength (Å)	0.71073	0.71073	0.71073	0.71073	0.71073	0.71073	0.71073	0.71073	0.71073
Crystal system	orthorhombic	orthorhombic	orthorhombic	monoclinic	monoclinic	monoclinic	monoclinic	monoclinic	monoclinic
Space group	<i>F2dd</i>	<i>Fddd</i>	<i>Fddd</i>	<i>C2/c</i>	<i>C2/c</i>	<i>C2/c</i>	<i>C2/c</i>	<i>C2/c</i>	<i>C2/c</i>
<i>a</i> (Å)	15.6371(10)	15.9599(5)	15.9234(4)	31.357(4)	31.420(4)	31.473(4)	31.506(4)	31.536(3)	31.540(4)
<i>b</i> (Å)	31.0298(19)	30.6138(8)	30.7560(7)	15.654(2)	15.609(2)	15.592(2)	15.586(18)	15.5749(18)	15.568(2)
<i>c</i> (Å)	37.083(2)	35.8049(9)	36.1096(8)	23.216(5)	23.220(5)	23.252(5)	23.281(3)	23.325(3)	23.336(5)
β (°)	90	90	90	126.779(3)	126.522(3)	126.422(3)	126.407(3)	126.413(3)	126.411(3)
Volume (Å ³)	17993.1(19)	17494.0(8)	17684.3(7)	9127(2)	9152(3)	9182(3)	9201.1(18)	9219.7(18)	9221(3)
Z	16	32	32	8	8	8	8	8	8
Calculated density (g cm ⁻³)	1.465	1.365	1.350	1.308	1.304	1.300	1.297	1.295	1.295
Absorption coefficient (mm ⁻¹)	0.805	0.819	0.810	0.784	0.783	0.780	0.778	0.777	0.777
F ₀₀₀	8224	7392	7392	3696	3696	3696	3696	3696	3696
Approx. Crystal size (mm ³)	0.29×0.18×0.14	0.28×0.25×0.18	0.28×0.25×0.18	0.28×0.25×0.18	0.275×0.25×0.18	0.28×0.25×0.18	0.28×0.25×0.18	0.28×0.25×0.18	0.28×0.25×0.18
θ range for data collection (°)	1.6 to 25.09	2.2 to 26.52	2.2 to 25.92	2.1 to 25.76	2.1 to 26.41	2.1 to 26.43	2.1 to 26.11	2.1 to 26.08	2.1 to 26.09
Reflections collected	78483	41866	87033	12203	71619	12683	12921	77866	86680
Completeness to θ max (%)	0.997	0.999	0.997	0.973	0.980	0.964	0.976	0.987	0.986
Data/restraints/parameters	7926 / 1 / 542	4554 / 0 / 272	4312 / 0 / 284	8528 / 0 / 541	9211 / 0 / 541	9120 / 0 / 541	8936 / 0 / 541	9038 / 0 / 541	9031 / 0 / 541
Goodness-of-fit on F ²	1.063	1.027	1.096	1.035	1.337	1.428	1.507	1.469	1.544
Final R indices [I > 2 σ (I)]	R1 = 0.024 wR2 = 0.061	R1 = 0.040 wR2 = 0.087	R1 = 0.040 wR2 = 0.144	R1 = 0.118 wR2 = 0.293	R1 = 0.118 wR2 = 0.330	R1 = 0.118 wR2 = 0.330	R1 = 0.124 wR2 = 0.348	R1 = 0.124 wR2 = 0.354	R1 = 0.1259 wR2 = 0.362
R indices	R = 0.025 wR2 = 0.061	R1 = 0.074 wR2 = 0.103	R1 = 0.066 wR2 = 0.1595	R1 = 0.140 wR2 = 0.310	1 = 0.151 wR2 = 0.3539	R1 = 0.1446, wR2 = 0.3541	R1 = 0.150 wR2 = 0.3710	R1 = 0.160 wR2 = 0.3802	R1 = 0.152 wR2 = 0.3822
Miller index ranges	-18 ≤ h ≤ 18 -36 ≤ k ≤ 36 -44 ≤ l ≤ 44	-18 ≤ h ≤ 20 -38 ≤ k ≤ 38 -42 ≤ l ≤ 44	-19 ≤ h ≤ 19 37 ≤ k ≤ 37 -44 ≤ l ≤ 44	-38 ≤ h ≤ 38 -19 ≤ k ≤ 19 -28 ≤ l ≤ 28	-39 ≤ h ≤ 38 -19 ≤ k ≤ 19 -28 ≤ l ≤ 29	-39 ≤ h ≤ 39 -19 ≤ k ≤ 19 -29 ≤ l ≤ 29	-38 ≤ h ≤ 38 -19 ≤ k ≤ 19 -28 ≤ l ≤ 28	-33 ≤ h ≤ 38 -19 ≤ k ≤ 19 -28 ≤ l ≤ 28	-38 ≤ h ≤ 38 -19 ≤ k ≤ 19 -28 ≤ l ≤ 28

4. Structural phase classification

Table S2. Classification of the different structural phases.

COB-DMF	As-synthesized version containing DMF guest molecules
COB⁰	Host framework determined under vacuum
COB-CO₂³	Form determined under 3 bar of CO ₂ gas pressure
COB-CO₂¹⁰	Form determined under 10 bar of CO ₂ gas pressure
COB-CO₂¹⁴	Form determined under 14 bar of CO ₂ gas pressure
COB-CO₂¹⁸	Form determined under 18 bar of CO ₂ gas pressure
COB-CO₂²²	Form determined under 22 bar of CO ₂ gas pressure
COB-CO₂³⁰	Form determined under 30 bar of CO ₂ gas pressure
COB-CO₂³⁵	Form determined under 35 bar of CO ₂ gas pressure

5. Perspective view of the COB-DMF framework (guest not shown). The pyridyl (BPMP) linkers have been omitted for clarity.

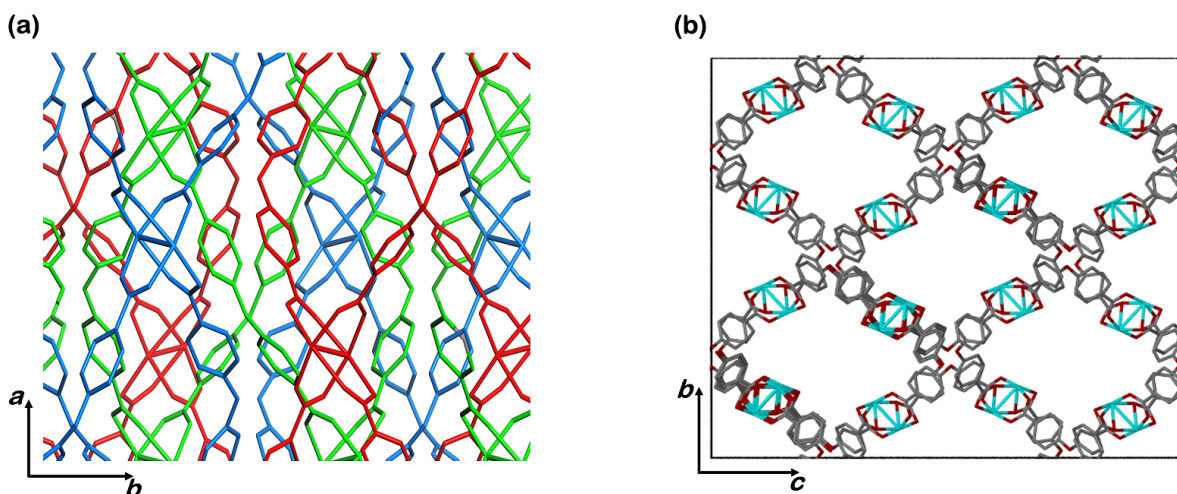


Figure S1. (a) COB-DMF perspective view without pyridyl ligand and the guest, (b) COB-DMF showing the rhombic shape in capped-stick representation without pyridyl ligand and the guest.

6. Thermogravimetric analysis

Thermogravimetric analyses were carried out on a TA Instruments Q500 analyzer. Samples ranging in mass from 2 - 6 mg were placed in an aluminum pan and heated from room temperature to 600 °C at a rate of 10 °C min⁻¹ under N₂ flow of 50 mL min⁻¹. Data Analysis was carried out using the Universal Analysis 2000 (TA Instruments, Version 4.5A) software.

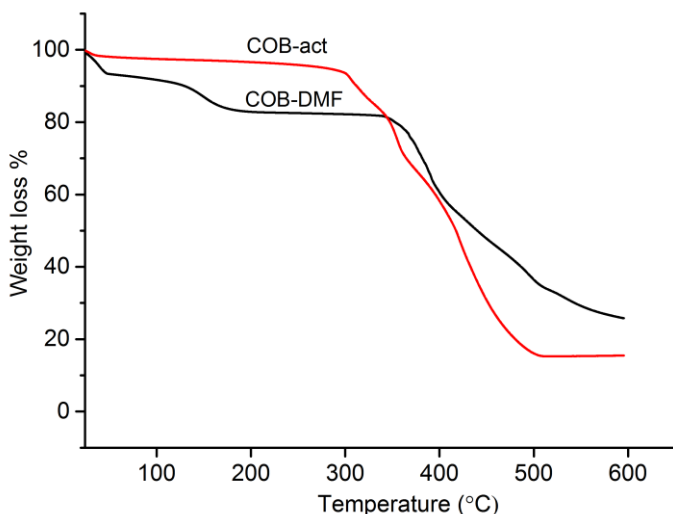


Figure S2. TGA analysis of **COB-DMF** and **COB⁰**. The initial weight loss event (starting at room temperature) for **COB-DMF** is due to surface solvent. The solvate is then stable upon further heating to approximately 125 °C, after which the included DMF is released.

7. PXRD Results

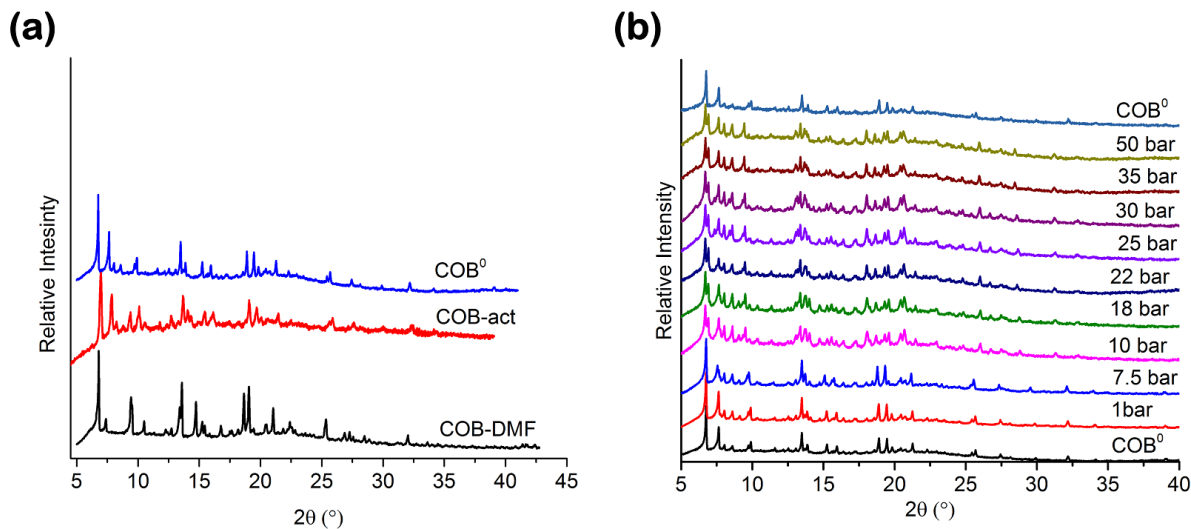


Figure S3. (a) PXRD diffractograms of the corresponding phases recorded at 298 K and (b) in situ variable-pressure PXRD patterns recorded with the sample under vacuum or controlled CO₂ pressure at 298 K.

8. Sorption of N₂

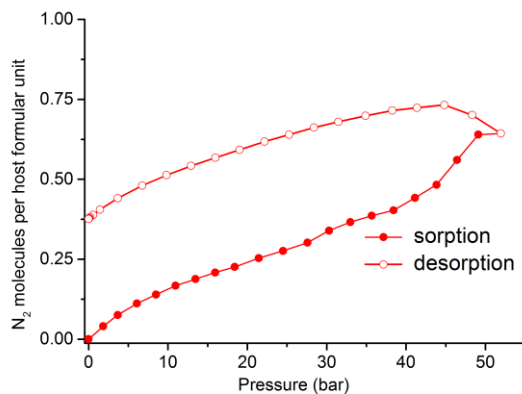


Figure S4. Volumetric sorption of N₂ at 298 K.

9. Unit cell parameters of COB after the phase-change from the *Fddd* to the *C2/c* structure

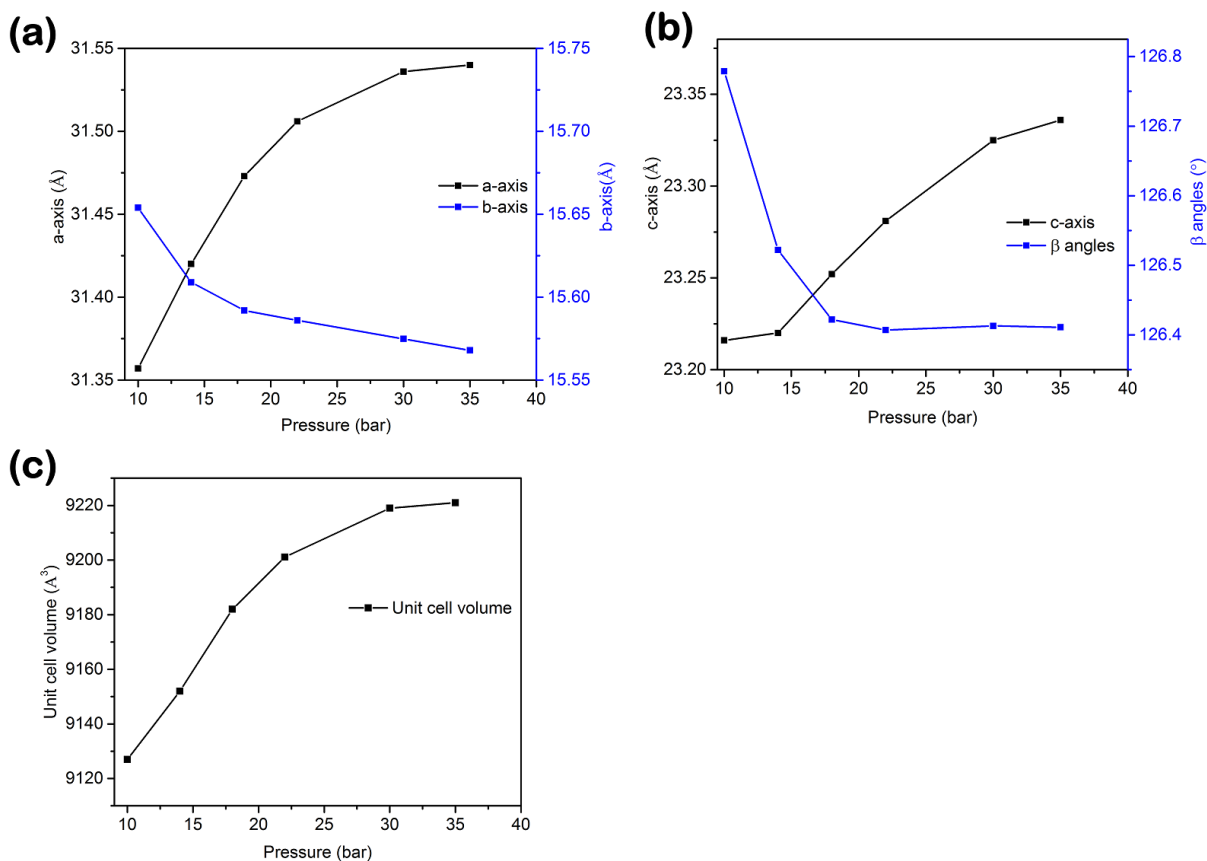


Figure S5. Plots of (a) *a* and *b* axes, (b) *c* axes and β angles, and (c) the unit cell volumes of COB-CO₂¹⁰, COB-CO₂¹⁴, COB-CO₂¹⁸, COB-CO₂²², COB-CO₂³⁰, and COB-CO₂³⁵ as a function of pressure.

10. Use of unit cell dimensions to calculate rhombic lengths, vertical and horizontal distances, and angles for COB⁰ and COB-CO2³

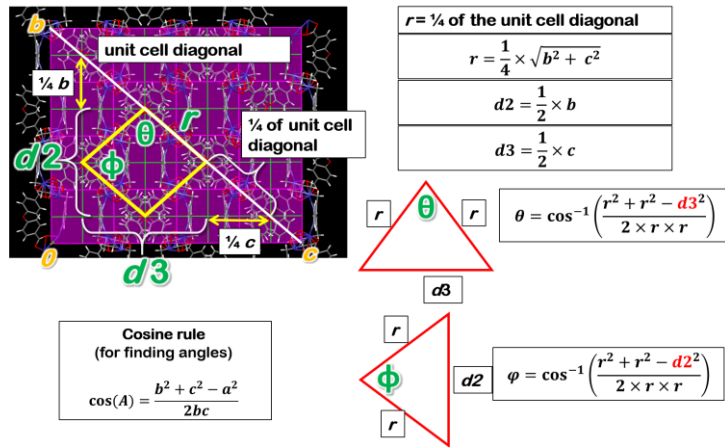


Figure S6. Determination of rhombic geometry for COB⁰ and COB-CO2³.

11. Use of unit cell dimensions to determine parallelogram shape for the monoclinic structures

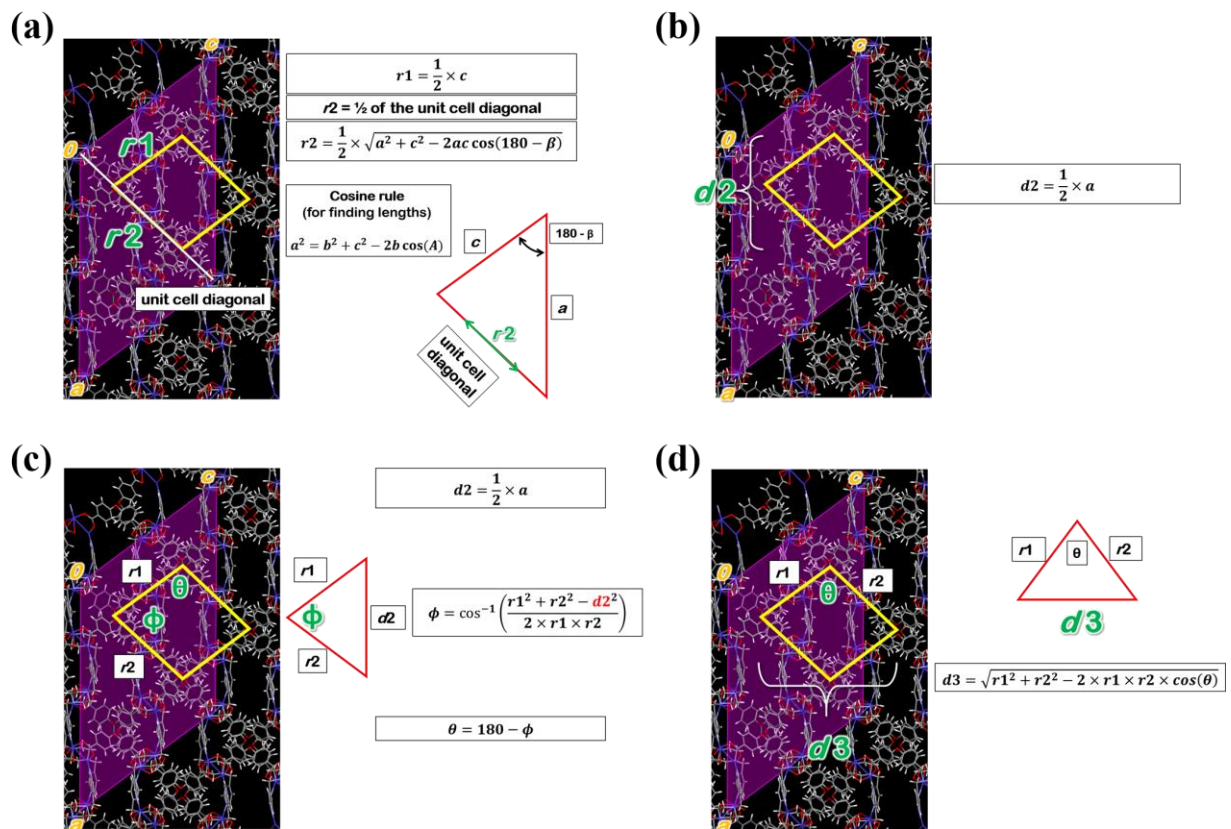


Figure S7. Determination of (a) r1 and r2 (b) d2, (c) phi and (d) d3.

Table S3. Selected non-bonding distances and angles (Figures S6 and S7) within the **COB** network before and after the phase change.

Complex	COB ⁰	COB-CO2 ³	COB-CO2 ¹⁰	COB-CO2 ¹⁴	COB-CO2 ¹⁸	COB-CO2 ²²	COB-CO2 ³⁰	COB-CO2 ³⁵
<i>d</i> 1 (Å)	12.20 (N1-N1)	12.25 (N1-N1)	12.36 (N3-N3)	12.47 (N3-N3)	12.49 (N3-N3)	12.51 (N3-N3)	12.52 (N3-N3)	12.51 (N3-N3)
<i>ω</i> (°)	116.69 (N1-C17-C20)	117.69 (N1-C17-C20)	119.35 (N3-C42-C42)	121.12 (N3-C39-C42)	120.38 (N3-C39-C42)	120.81 (N3-C39-C42)	121.16 (N3-C39-C42)	121.31 (N3-C39-C42)
<i>d</i> 2 (Å)	15.307	15.38	15.68	15.71	15.74	15.75	15.77	15.77
<i>d</i> 3 (Å)	17.90	18.05	18.78	18.76	18.77	18.79	18.82	18.83
<i>r</i> 1 (Å)	11.78	11.86	-	-	-	-	-	-
<i>r</i> 1 (Å)	11.78	11.86	11.61	11.61	11.63	11.64	11.66	11.67
<i>r</i> 2 (Å)	11.78	11.86	12.75	12.83	12.87	12.88	12.90	12.90
<i>θ</i> (°)	98.94	99.15	100.3	100.1	100.1	100.1	100.1	100.1
<i>φ</i> (°)	81.06	80.84	79.71	79.89	79.94	79.94	79.90	79.89

12. Description of video file

Video S1 shows a simplified schematic representation of the mechanism of pore opening and closing in response to gas pressure. This video file is best viewed with the video player set to loop.

13. Rebek's 55% Solution

Rebek postulated a 55% 'rule' for the encapsulation of small guest molecules within the internal cavities of host molecules in solution.⁸ We believe that it is reasonable to apply Rebek's rule to the crystalline solid state. The molecular volume of a DMF molecule is approximately 72 Å³. The discrete guest-accessible cavity of **COB-DMF** has a volume of 395 Å³, and the crystal structure contains two host molecules per cavity. By applying the 55% rule we estimate that each cavity can accommodate 3 DMF molecules, which is consistent with 1.5 DMF molecules per host formula unit.

References

1. Pocic, D.; Planeix, J.; Kyritsakas, N.; Jouaiti, A.; and Hosseini, M. *CrystEngComm*. **2005**, *7*, 624-628
2. *SAINT Data Reduction Software*, Version 6.45; Bruker AXS Inc., Madison, WI, **2003**.
3. (a) *SADABS*, Version 2.05; Bruker AXS Inc., Madison, WI, **2002**; (b) Blessing, R. H. *Acta Crystallogr., Sect. A: Found. Crystallogr.* **1995**, *51*, 33-38.
4. Sheldrick, G. M. *Acta Crystallogr., Sect. A: Found. Crystallogr.* **2008**, *64*, 112-122.
5. Barbour, L. J. *J. Supramol. Chem.* **2001**, *1*, 189-191.
6. Dolomanov, O. V.; Bourhis, L. J.; Gildea, R. J.; Howard, J. A. K.; Puschmann, H. *J. Appl. Cryst.* **2009**, *42*, 339-341.
7. Connolly, M. L. *J. Mol. Graphics.* **1993**, *11*, 139-141.
8. Mecozzi, S.; Rebek, J. *Chem. Eur. J.* **1998**, *4*, 1016-1022.

CHAPTER 3

A new dynamic framework with direct *in situ* visualisation of breathing under CO₂ gas pressure

3.1. Manuscript submitted to *CrystEngComm*

Contributions of the author:

- ✓ Design of project
- ✓ Preparation of the new MOF
- ✓ Collection of single-crystal X-ray data and gas cell work
- ✓ Solution and refinement of single-crystal X-ray structure
- ✓ Recording of PXRD patterns
- ✓ Recording of TGA thermograms
- ✓ Sorption analysis
- ✓ Interpretation of results with Charl X. Bezuidenhout and Dewald P. van Heerden and Len
- ✓ Writing the first draft of the article

A new dynamic framework with direct *in situ* visualisation of breathing under CO₂ gas pressure

Received 00th January 20xx,
Accepted 00th January 20xx

DOI: 10.1039/x0xx00000x

Phumile Sikiti, Charl X. Bezuidenhout, Dewald P. van Heerden, and Leonard J. Barbour*

Department of Chemistry and Polymer Science, University of Stellenbosch, Matieland 7602, South Africa

Using *in situ* single-crystal X-ray diffraction analysis (SCD), direct structural evidence has been obtained for breathing behaviour of a new flexible MOF COB1. Desolvation of the as-synthesised material results in deformation of the coordination geometries due to flexibility of the bridging ligands, and the framework is capable of switching from a wide-pore to a narrow-pore form, with substantial reduction in guest-accessible volume. Upon exposure to CO₂ gas the activated framework breathes and switches back to the wide-pore phase. This breathing behaviour is supported by gas sorption analysis, pressure-gradient differential scanning calorimetry, powder X-ray diffraction analysis and molecular modelling.

Metal-organic frameworks (MOFs) are a class of porous materials constructed using metal ions that are bridged by polytopic organic ligands.¹ Amongst the large number of known MOF materials there are recurring coordination motifs called secondary building units (SBUs), which allow rational design of new materials from new and existing organic building blocks (i.e., reticular synthesis).² Recurring SBUs may yield isorecticular MOFs³ that are rigid and porous, with wide-ranging topologies.⁴ Some MOFs have been shown to possess high surface areas⁵ with sufficient structural diversity to allow tuning of the pore space.^{2b} This tunability has prompted intense investigation into various applications that include catalysis, gas storage and separation of small molecules.⁶ Although MOFs were first reported to be rigid like zeolites, judicious selection of metal ions and organic ligands has yielded MOFs that exhibit structural flexibility in response to external stimuli such as light, heat, and pressure.⁷ In particular, flexible MOFs can distort or even change phase under gas pressure to increase adsorption capacity.⁸ Gas-induced flexibility in MOFs has been classified into different modes such as breathing, swelling, linker rotation, and sliding of layers (in interpenetrated MOFs).^{8a,9} Breathing is accompanied by structural distortions such as changes in bond lengths and angles^{7b} and generally gives rise to stepped sorption profiles where each step is associated with a phase-change.¹⁰ Importantly, breathing has been shown to enhance working capacity for gas storage.¹¹ Among the earliest examples of flexible MOFs that undergo breathing behaviour under gas pressure¹² are the MIL (Materials of Institute Lavoisier) family

([M(X)(BDC)], where M is trivalent Al, Cr, Fe or Ga and X is OH⁻ or F⁻),¹³ and pillared-layered **DMOF-1**.¹⁴ Owing to the difficulty of maintaining single crystal integrity during activation of these materials, the phase changes under gas pressure are normally characterised by variable-pressure powder X-ray diffraction (VP-PXRD) under non-ambient conditions,¹⁵ with support from theoretical studies. We have previously reported direct visualisation of phase changes under gas pressure by means of variable-pressure single-crystal diffraction (VP-SCD);¹⁶ this approach is generally superior to VP-PXRD because it often provides unequivocal structural information relating to the structural flexibility. However, VP-SCD presents a greater technical challenge as it involves exposing a single crystal to a particular gas pressure within a confined environment during the diffraction experiment, with the added requirement that the single crystals must survive the stresses associated with solid-solid phase transitions.¹⁷

Here, we report the structure of the non-interpenetrated flexible MOF **COB1-DMF**, which undergoes structural dynamics upon activation. The framework exhibits further structural adaptation under CO₂ gas pressure at 298 K, and complementary characterisation by means of VP-SCD and pressure-gradient differential scanning calorimetry (PG-DSC) offers detailed structural insight into the flexibility.

Blue prismatic crystals of the solvated MOF {[Co₂(OBA)₂(BPMP)]·2.5(DMF)}_n (**COB1-DMF**), where OBA = 4,4'-oxybis(benzoic acid) and BPMP = 4-bis(pyridin-4-ylmethyl)piperazine), were prepared according to the procedure outlined in Scheme S1. The crystals were subjected

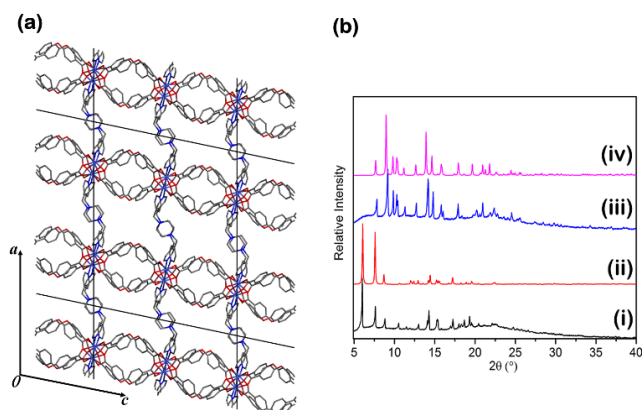


Fig. 1 (a) Perspective view of the host framework of **COB1-DMF**, shown in capped-stick representation (DMF guest molecules and hydrogen atoms omitted for clarity). (b) PXRD diffractograms of (i) **COB1-DMF** (recorded at 298 K), (ii) simulated from the **COB1-DMF** SCD structure recorded at 100 K, (iii) **COB1-act** (recorded at 298 K) and (iv) simulated from **COB1⁰** SCD structure recorded under vacuum at 298 K.

Department of Chemistry and Polymer Science, University of Stellenbosch, Matieland, 7600, South Africa E-mail: ljb@sun.ac.za; Fax: (+27) 21-808-3360

† Electronic supplementary information (ESI) available: Crystallographic Information Files CCDC 1878697, 1878700, 18787101, 1880240, 1880241, experimental methods, PXRD, PG-DSC, and video files. See DOI: 10.1039/x0xx00000x

to SCD analysis at 100 K. **COB1-DMF** crystallises in the monoclinic space group $P2_1/n$ (Table S1) and the structure consists of a three-dimensional (3D) non-interpenetrated framework with primitive cubic (**pcu**) network topology (we report elsewhere¹⁸ that an orthorhombic phase is obtained by raising the synthesis temperature from 80 to 100 °C). Dinuclear Co paddlewheel SBUs are linked equatorially by OBA dianions to form corrugated layers that are pillared axially by BPMP linkers (Fig. 1a). The framework is permeated by 2D channels that propagate parallel to (100) (Fig. 2a); these channels are occupied by highly disordered DMF molecules, which could not be modelled owing to extensive disorder. The guest-accessible volume of **COB1-DMF** is approximately 38% that of the material, as determined using the Connolly surface routine of Materials Studio.¹⁹ Phase purity of the bulk material was confirmed by PXRD analysis (i.e. the PXRD pattern simulated from the crystal structure determined at 100 K corresponds to that recorded for the bulk material at 298 K, as shown in Fig. 1b).

Thermogravimetric analysis (TGA) of the as-synthesised material shows a 30% weight loss in the range 25 to 130 °C, which corresponds to 2.5 DMF molecules per host formula unit (HFU). The framework starts to decompose after 350 °C (Fig. S1, ESI[†]). **COB1-DMF** was therefore activated at 120 °C under dynamic vacuum (3.1×10^{-2} mbar) for 24 hours. PXRD analysis confirmed retention of crystallinity and conversion to a new phase (Fig. 1b), hereafter referred to as **COB1-act**. Owing to the rapid rate at which the DMF molecules leave the framework upon activation, single crystals of **COB1-DMF** disintegrate and become unsuitable for SCD analysis. In order to slow down the rate of desolvation, guest exchange was first carried out by immersing **COB1-DMF** in diethyl ether for 24 hours, followed by subjecting the crystals to dynamic vacuum at ca 195 K (using a dry-ice/acetone slurry) for a further 24 hours. A crystal suitable for SCD analysis was placed in an environmental gas cell,^{16,20} which was then evacuated for 2 hours at 298 K. Intensity data recorded at 298 K reveal a new reduced-pore form (**COB1⁰**), the structure of which is consistent with the PXRD pattern for the bulk activated material. The network connectivity remains intact, although the space group changes from $P2_1/n$ for **COB1-DMF** to $C2/c$ for **COB1⁰** (Table S1, ESI[†]). In converting from **COB1-DMF** to **COB1⁰**, the framework switches from a wide-pore phase to a narrow-pore phase with isolated voids (Fig. 2a). The guest-accessible volume decreases dramatically from 38% to 17%. Activation also results in significant shrinkage of the crystal along the crystallographic *a* and *c* axes (by ca 6 and 3.4 Å, respectively), with concomitant elongation by ca 3 Å along the crystallographic *b* axis[‡] (Fig. S2, ESI[†]).

To understand the phase change that occurs upon desolvation, the structural geometries and moiety conformations were examined before and after activation. The conformation of OBA is largely preserved; the centroid...centroid distances of the Co₂ SBUs across the OBA linker and the centroid_{SBU}...O_{ether}...centroid_{SBU} angle remain unchanged at ca 14.3 Å and 119.5°, respectively (Fig. 2b and Table S3, ESI[†]). The SBU centroid...centroid distance across the BPMP pillar is also maintained at 19.0 Å, (Fig. 2c) while the piperazine moiety undergoes a rotation from 26.4° to almost perpendicular (84.1°) with respect to the *ac* plane (*P_{ac}*). In

addition, the SBU Co...Co distance elongates from 2.63 to 2.75 Å and the acute angle of the Co...Co axis with respect to *P_{ac}* decreases from 43.9° to 35.9° (Fig. 2d). The structural phase change from **COB1-DMF** to **COB1⁰** therefore involves a distortion of the cobalt coordination geometries, with concomitant deformation of the flexible pillaring ligands.

Gas sorption analyses were carried out at 298 K using CO₂ and N₂ (Fig. 3a). N₂ exhibits a typical type I sorption isotherm with a maximum loading of 0.5 molecules per HFU at 50 bar. The CO₂ sorption isotherm features a single step with an onset pressure of approximately 19 bar, at which pressure the CO₂ uptake is approximately 1 molecule per HFU. We attribute the step to a structural transformation from **COB1⁰** to a new phase (**COB1-CO2¹⁹**). Upon further increase in pressure to 50 bar, apparent saturation is reached with a maximum uptake of 4 molecules of CO₂ per HFU. We note that the desorption isotherm does not match the adsorption isotherm; in addition to substantial hysteresis, it exhibits three desorption steps with onset pressures of 32, 23 and 10 bar.

To further investigate potential CO₂-induced gate-opening events, PG-DSC²⁰ analysis was carried out at 298 K over a CO₂ pressure range of 5 to 40 bar to independently confirm the stepped CO₂ sorption profiles (Fig. 3b). A single exothermic peak with an onset pressure of approximately 25 bar is observed for

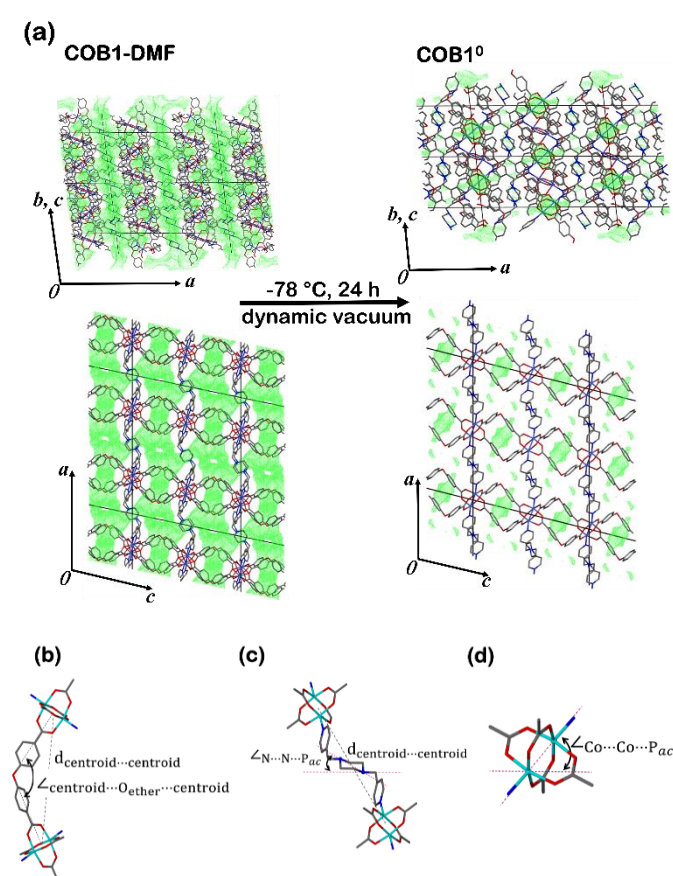


Fig. 2 (a) **COB1-DMF** with 2D guest-accessible channels represented by light green surfaces and **COB1⁰** with discrete voids after activation (probe radius 1.2 Å). Salient geometrical parameters: (b) OBA bend angle and length, (c) BPMP length and the acute angle between pyrazine and *P_{ac}* (d) Co...Co acute angle with *P_{ac}*.

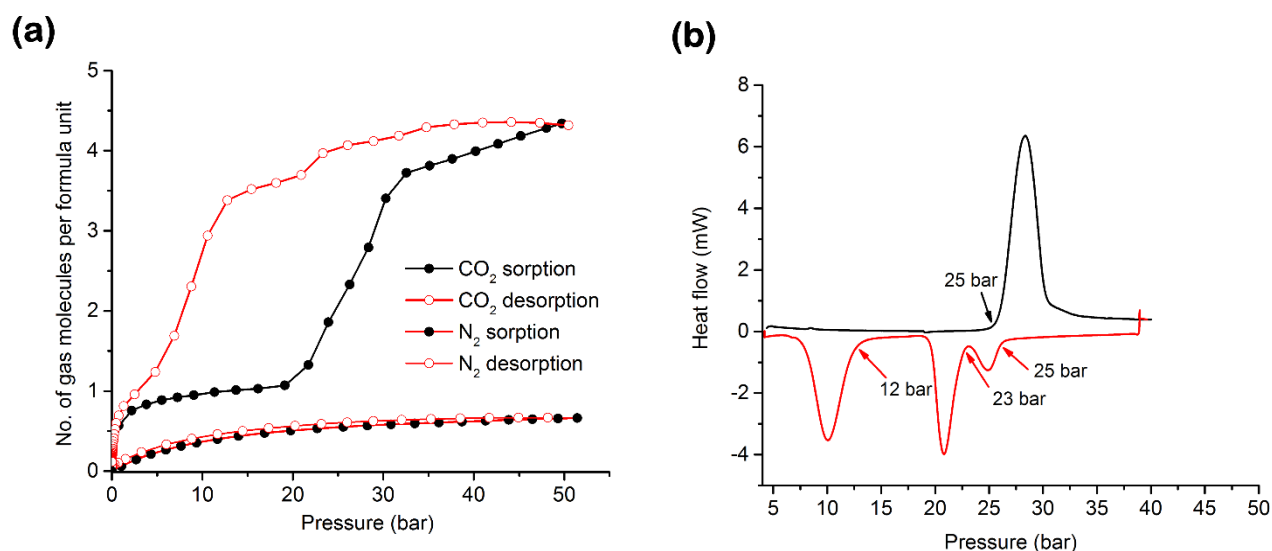


Fig. 3 (a) CO₂ and N₂ adsorption/desorption isotherms for **COB1** recorded at 298 K; (b) PG-DSC under CO₂ gas pressure recorded at 298 K.

increasing pressure; the peak corresponds approximately to the step observed in the adsorption isotherm, which signals the structural transformation to **COB1-CO2**¹⁹. Also consistent with the desorption isotherm, three endothermic peaks (with onset pressures of 25, 23, and 12 bar) are observed upon decreasing the CO₂ pressure from 40 to 5 bar. It is interesting to note that the CO₂ uptake pathway does not appear to be consistent with that for CO₂ release – i.e. single-step adsorption vs three-step desorption. This implies either that the structural transformations that occur do not follow a reversible pathway, or that the single step observed during adsorption represents a poorly resolved multi-step process. Indeed, upon lowering the temperature, the adsorption peak is resolved into two separate peaks (Fig. S3, ESI[†]).

PXRD diffractograms were recorded before and after the CO₂ sorption experiment (Fig. 4). By comparison to

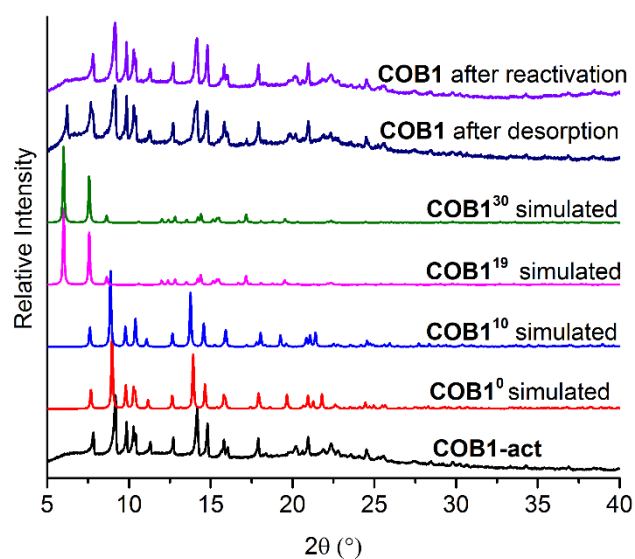


Fig. 4 Comparison of PXRD diffractograms of **COB1** recorded at 298 K to those simulated from VP-SCD crystal structures determined at 298 K.

diffractograms simulated from VP-SCD crystal structures, it appears that most of the material reverts to **COB1-act** after complete desorption. However, some of the material remains in the wide-pore form and the bulk sample only reverts completely to its original activated form after heating at 120 °C under dynamic vacuum (3.1×10^{-2} mbar).

In situ SCD structural characterisation was carried out at 298 K under controlled CO₂ gas pressure using an environmental gas cell.^{16,20} A single crystal of **COB1**⁰ was exposed to vacuum and subsequently pressurised incrementally to 10, 19 and 30 bar of CO₂. Despite diminishing reflection intensities (as compared to the data for **COB1**⁰) it was still possible to determine the crystal structures of **COB1-CO2**^x, where $x = 10, 19$ and 30 (Table S1, ESI[†]). In all three cases it was possible to model the host framework, but not the CO₂ guest molecules. The host structure of **COB1-CO2**¹⁰ is similar to that of **COB1**⁰. The transformation from **COB1-CO2**¹⁰ to **COB1-CO2**¹⁹ results in significant lengthening of the crystallographic a and c axes (by ca 6 and 3 Å, respectively), and concomitant shrinkage by ca 2 Å along the crystallographic b axis (Table S1 and Fig. S2, ESI[†]). Together, these changes result in an increase in the guest-accessible volume from 19% in **COB1-CO2**¹⁰ to 39% in **COB1-CO2**¹⁹. The acute angle between the paddlewheel and P_{ac} increases from 35.9° to 44.0°, while the OBA linker remains largely rigid during the phase transition (Table S3). Rotation of the piperazine moiety from 83.9° (**COB1-CO2**¹⁰) to 25.7° (**COB1-CO2**¹⁹) causes slight elongation of the SBU centroid...centroid separation across the BPMP pillar from 18.91 Å to 19.41 Å (Videos S1 and S2, ESI[†]). A theoretical evaluation at the plane-wave DFT-PBE level of theory revealed a 5.58 kcal mol⁻¹ energy cost per HFU that is compensated for by inclusion of extra CO₂ molecules (See ESI[†] for details). After the phase change, the crystal retains its singularity and SCD data recorded at 30 bar CO₂ pressure (**COB1-CO2**³⁰) shows that the framework geometry remains largely unchanged as compared to that of **COB1-CO2**¹⁹ (Table S1). Owing to severe crystal degradation, it was not possible to determine crystal structures of possible phases resulting from

decreasing the pressure after the crystals had been exposed to 30 bar of CO₂ pressure.

In summary, we have employed VP-SCD to investigate the CO₂-induced flexibility of a new dynamic non-interpenetrated pillared-layered MOF **COB1**. Upon activation 2D channels of the as-synthesised form **COB1-DMF** collapse to become discrete voids. **COB1** undergoes hysteretic and, ultimately, reversible breathing in the presence of CO₂ gas pressure. This type of behaviour is poorly understood for flexible porous materials and knowledge gained from in situ VP-SCD structural studies is critical for the development of new tuneable MOFs, for which sorption properties and other applications depend on control of the pore space.

The authors thank the National Research Foundation of South Africa for financial support and the Centre for High Performing Computing (CHPC) in Cape Town for use of their computational resources.

Notes and references

‡ A non-standard space group setting was imposed on the crystal structure of **COB1-DMF** in order to facilitate direct comparison of unit cell directions with those of the activated and gas-loaded forms. We note that activation results in an increase in symmetry from $P2_1/n$ for **COB1-DMF** to $C2/c$ for **COB1**⁰. This conversion involves halving of the periodicity along the crystallographic b axis from 15.7987(7) to 9.7971(6) Å, which is consistent with a macroscopic elongation of periodicity by 3.8 Å along this direction.

- (a) H. Furukawa, K. E. Cordova, M. O'Keeffe and O. M. Yaghi, *Science*, 2013, **341**, 1230; (b) O. M. Yaghi, M. O'Keeffe, N. W. Ockwig, H. K. Chae, M. Eddaoudi and J. Kim, *Nature*, 2003, 423, 705.
- (a) Li, H, Eddaoudi, M., O'Keeffe, M. and Yaghi, O. M. *Nature*, 1999, **402**, 276; (b) Z. Chen, L. J. Weselinski, K, Adil, Y. Belmabkhout, A. Shkurenko, H, Jiang, P. M. Bhatt, V, Guillerme, E. Duzon, D. X. Xue, M, O'Keeffe and M. Eddaoudi, *J. Am. Chem. Soc.*, 2017, **139**, 3265.
- M. Eddaoudi, J. Kim, N. Rosi, D. Vodak, J. Wachter, M. O'Keeffe and O. M. Yaghi, *Science*, 2002, **295**, 469.
- (a) D. Alezi, I.; Spanopoulos, V. Tsangarakis, A. Shkurenko, K, Adil, Y. M. O. Belmabkhout, M. Eddaoudi and P. N. Trikalitis, *J. Am. Chem. Soc.*, 2016, **138**, 12767; (b) D. Alezi, A. M. Peedikakkal, L. J. Weselinski, V. Guillerme, Y. Belmabkhout, A. J. Cairns, Z. Chen, L. Wojtas and M. Eddaoudi, *J. Am. Chem. Soc.*, 2015, **137**, 5421; (c) P. F. Muldoon, C. Liu, C. C. Miller, S. B. Koby, A. Gamble Jarvi, T. Y. Luo, S. Saxena, M. O'Keeffe and N. L. Rosi, *J. Am. Chem. Soc.* 2018, **140**, 6194.
- O. K. Farha, I. Eryazici, N. C. Jeong, B. G. Hauser, C. E. Wilmer, A. A. Sarjeant, R, Q; Snurr, S. T. Nguyen, A. O. Yazaydin and J. Hupp, *J. Am. Chem. Soc.*, 2012, **134**, 15016.
- (a) T. M. McDonald, J. A. Mason, X. Kong, E. D Bloch, E. D. Gygi, A, Dani, V, Crocella, F. Giordanino, S.O. Odoh, W. S. Drisdell, B. Vlasisavljevich, A. L.; Dzubak, R. Poloni, S.K. Schnell, N. Planas, K. Lee, T. Pascal, L. F Wan, D. Prendergast, J. B. Neaton, B. Smit, J. B. Kortright, L. Gagliardi, S. Bordiga, J. A. Reimer and J. R Long, *Nature*, 2015, **519**, 303; (b) L. Liang, C. Liu, F. Jiang, Q. Chen, L. Zhang, H. Xue, H.-L. Jiang, J. Qian, D. Yuan and M, Hong, *Nat. Commun.*, 2017, **8**, 1233.
- (a) S. Horike, S. Shimomura and S. Kitagawa, *Nat. Chem.*, 2009, **1**, 695; (b) A. Schneemann, V. Bon, I. Schwedler, I. Senkowska, I. Kaskel and R. A. Fischer, *Chem. Soc. Rev.*, 2014, **43**, 6062; (c) Y. Yan, A. E. O'Connor, G. Kanthasamy, G. Atkinson, D. R. Allan, A. J. Blake and M. Schröder, *J. Am. Chem. Soc.*, 2018, **140**, 3952.
- (a) S. Krause, V. Bon, I. Senkowska, U. Stoeck, D. Wallacher, D. M. Töbrens, S. Zander, R. S.; Pillai, G. Maurin, F.-X. Coudert and S. Kaskel, *Nature*, 2016, **532**, 348; (b) E. J. Carrington, C. A, McAnally, A. J. Fletcher, S. P. Thompson, M. Warren and L. Brammer, *Nat. Chem.*, 2017, **9**, 882.
- (a) D. Bousquet, F. X. Coudert, A. G. Fossati, A. V. Neimark, A. H. Fuchs and A. Boutin, *J. Chem. Phys.*, 2013, **138**, 174706; (b) P. Lama, A. Aggarwal, X. C. Bezuidenhout and L. J. Barbour, *Angew. Chem. Int. Ed.*, 2016, **55**, 13271, *Angew. Chem.*, 2016, **128**, 13465.
- (a) R. Kitaura, K. Seki, G. Akiyama and S. Kitagawa, *Angew. Chem. Int. Ed.*, 2003, **42**, 428; (b) K. Uemura, S. Kitagawa, K. Fukui and K. Saito, *J. Am. Chem. Soc.*, 2004, **126**, 3817; (c) K. Uemura, R. Matsuda and S. Kitagawa, *J. Solid State Chem.*, 2005, **178**, 2420.
- J. A. Mason, J. Oktawiec, M.K. Taylor, M. Hudson, J.; Rodriguez, J. E. Bachman, M. L.; Gonzalez, A. Cervellino, A. Guagliardi, C. M Brown, P. L. Llewellyn, N, Masciocchi and J. R. Long, *Nature*, 2015, **527**, 357.
- (a) O. K. Farha and J. T. Hupp, *Acc. Chem. Res.*, 2010, **43**, 1166; (b) M. Shivanna, Q. Y. Yang, A. Bajpai, E. Patyk-Kazmierczak and M. J. Zaworotko, *Nat. Commun.*, 2018, **9**, 3080; (c) H. Aggarwal, P. M. Bhatt, C. X. Bezuidenhout and L. J. Barbour, *J. Am. Chem. Soc.*, 2014, **136**, 3776.
- C. Serre, S. Bourrelly, A. Vimont, N. A. Ramsahye, G. Maurin, P.L. Llewellyn, M. Daturi, Y. Filinchuk, O.; Leynaud, P. Barnes and G. Férey, *Adv. Mater.*, 2007, **19**, 2246.
- D. N. Dybtsev, H. Chun and K. Kim, *Angew. Chem. Int. Ed.*, 2004, **43**, 5033.
- (a) A. Schneemann, P. Vervoorts, I. Tu. M. Hante, S. Wannapaiboon, C.; Sternemann, M, Paulus, D.C. F. Wieland, S. Henke and R. A. Fischer, *Chem. Mater.*, 2018, **30**, 1667; (b) S. Henke, A. Schneemann, A. Wutscher and R. A. Fischer, *J. Am. Chem. Soc.*, 2012, **134**, 9464.
- T. Jacobs, G. O. Lloyd, J. A. Gertenbach, K. Müller-Nedebock, C. Esterhuysen and L. J. Barbour, *Angew. Chem. Int. Ed.*, 2012, **51**, 4913.
- R. E. Morris and L. Brammer, *Chem. Soc. Rev.* 2017, **46**, 5444.
- P. Sikiti, C. X. Bezuidenhout, D. P. van Heerden and L. J. Barbour, Submitted.
- Dassault Systèmes BIOVIA, Materials Studio*, Release 18, San Diego: Dassault Systèmes, 2017.
- (a) P. M Bhatt, E. Batisai, V.J. Smith and L. J. Barbour, *Chem. Commun.*, 2016, **52**, 11374; (b) P. Lama, P. H. Aggarwal, C. X. Bezuidenhout and L. J. Barbour, *Angew. Chem. Int. Ed.*, 2016, **55**, 13271; *Angew. Chem.*, 2016, **128**, 13465; (c) P. Lama and L. J. Barbour, *J. Am. Chem. Soc.*, 2018, **140**, 2145.

3.2 SUPPORTING INFORMATION

A new dynamic framework with direct *in situ* visualisation of breathing under CO₂ gas pressure

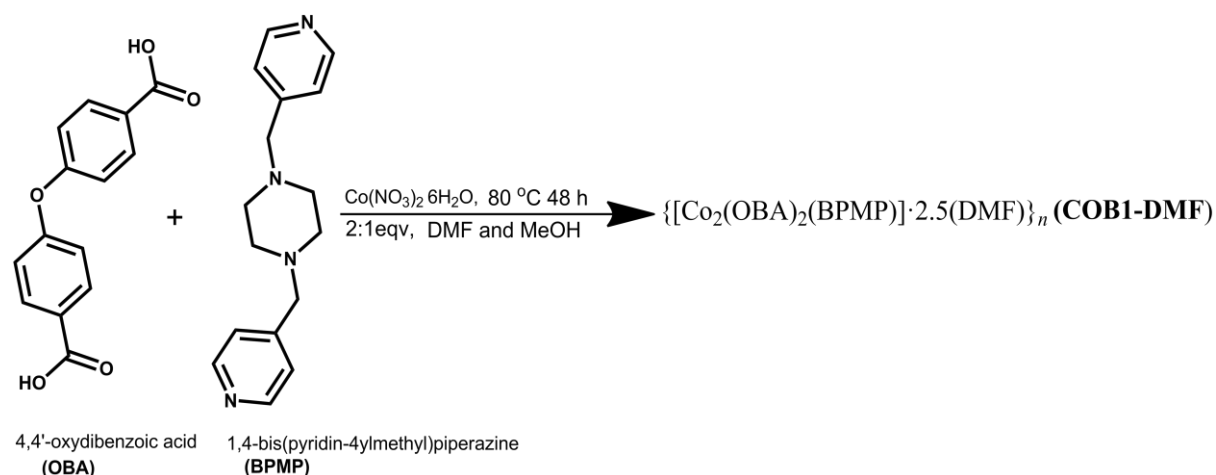
1. Synthesis and characterisation

Materials

All chemicals and solvents were purchased from Aldrich and used without further purification. The ligand 4-bis(pyridin-4-ylmethyl)piperazine was prepared according to a literature procedure.¹

Preparation of COB1-DMF

{[Co₂(OBA)₂(BPMP)]·2.5(DMF)}_n (COB1-DMF): Co₂(NO₃)₂·6H₂O (1 mmol), 4,4'-oxybis(benzoic acid) (OBA, 1 mmol) and (4-bis(pyridin-4-ylmethyl)piperazine (BPMP, 1 mmol) were mixed in 2 ml methanol (MeOH) and dimethylformamide (DMF) and placed in a pre-heated oven at 80 °C. Blue block-shaped crystals of solvated (COB1-DMF) were obtained after 48 h.



Scheme S1. Synthesis of COB1-DMF.

2. Methods

Thermogravimetric analysis (TGA)

Thermogravimetric analysis was carried out using a TA Instruments Q500 analyser. The sample was loaded onto an aluminium pan and heated at 10 °C/min from room temperature to 600 °C.

Activation method of COB1-DMF

Pure bulk material of COB1-DMF was activated at 120 °C under dynamic vacuum (3.1×10^{-2} mbar) for 12 hours to yield the fully desolvated form COB1-act. TGA shows that COB1-act is desolvated and PXRD analysis shows that it is still crystalline. Direct

activation does not yield single crystals suitable for SCD analysis. Single crystals of suitable quality were obtained by activation via solvent exchange with diethyl ether for 2 days, followed by activation in a Schlenk tube at ca 195 K (slurry of dry ice and acetone) under a dynamic vacuum of 3.1×10^{-2} mbar for 48 hours. The desolvated form absorbs moisture and needed to be pre-activated under dynamic vacuum at room temperature for 2 hours before any further experiments were carried out.

Powder X-ray Diffraction (PXRD)

Experiments were carried out on a PANalytical X'Pert PRO instrument with Bragg-Brentano geometry. Intensity data were recorded using an X'Celerator detector and 2 θ scans in the range of 5-40° were performed. During the experiment the powdered sample was exposed to Cu-K α radiation ($\lambda = 1.5418 \text{ \AA}$). The PXRD patterns of the as-synthesised (**COB1-DMF**) and activated (**COB-act**) samples were recorded at 298 K.

Single-crystal X-ray Diffraction

Single crystal X-ray diffraction data were collected on a Bruker APEX-II Quasar CCD area-detector diffractometer equipped with an Oxford Cryostream 700Plus cryostat, and on a Bruker D8 Venture diffractometer equipped with a PHOTON II CPAD detector and an Oxford Cryostream 800Plus cryostat. A multilayer monochromator with MoK α radiation ($\lambda = 0.71073 \text{ \AA}$) from an Incoatec I μ S microsource was used. Data reduction was carried out by means of standard procedures using the Bruker software package SAINT² and absorption corrections and the correction of other systematic errors were performed using SADABS.³ The structures were solved by direct methods using SHELXS-2016 and refined using SHELXL-2016⁴ and X-Seed⁵ or Olex⁵ were used as the graphical interface for the SHELX program suite. Hydrogen atoms were placed in calculated positions using riding models.

Environmental gas cell experiments

An environmental gas cell (developed in-house) was used to determine the crystal structures of the various phases at 298 K under controlled pressures by means of single-crystal X-ray diffraction. First, the structure of **COB1⁰** was determined under vacuum after activating a crystal of **COB1-DMF**. The structure of **COB1-CO2¹⁰** was determined after pressurising **COB1⁰** with 10 bar of CO₂ gas for 8 hours. The structure of **COB1-CO2¹⁹** was determined after pressurising the crystal of **COB1-CO2¹⁰** with 19 bar CO₂ and allowing it to equilibrate for 8 hours. The structure of **COB1-CO2³⁰** was determined after pressurising **COB1-CO2¹⁹** with 30 bar CO₂ and equilibrating for 8 hours. We note that *R*₁ for the gas-loaded structures increases with pressure, and this is most likely due to increasing strain experienced by the crystal.

Volumetric Sorption Analysis

A Setaram PCTPro-E&E gas sorption analyser with a MicroDoser attachment was utilised to conduct high pressure gas sorption experiments with CO₂ and N₂. The instrument utilises Sievert's volumetric method. The sample temperature was maintained to an accuracy of ± 1 °C using a Grant refrigerated recirculation bath filled with antifreeze and water. A sample at known pressure and volume was connected to a reservoir of known volume and pressure through an isolation valve. The valve was opened, and the system allowed to equilibrate. The difference between the measured and calculated pressures was used to determine the amount of gas adsorbed. National Institute of Standards and Technology (NIST) software was used to calculate the thermodynamic corrections to account for the non-ideal behaviour of the gases at relatively high pressures. The PCTPro-E&E with the MicroDoser attachment is used for small sample sizes and has a range of vacuum to 60 bar. Sample sizes of 80 mg were used and activated in situ using vacuum and heat, if necessary. Blank runs for each gas were recorded to further correct for any other residual systematic errors in the experiment. Figure preparation and data analyses were performed using Microsoft Excel and OriginPro.

Pressure-Gradient Differential Scanning Calorimetry for CO₂ (PG-DSC)

Experiments were carried out using a Setaram Micro-DSC7 Evo instrument. Heat flow was recorded at 298 K in the pressure range of 4-35 bar for CO₂ at 298 K.

Table S1. Crystallographic table of **COB1** under controlled pressure of CO₂

Complex	COB1-DMF	COB1 ⁰	COB1-CO ₂ ¹⁰	COB1-CO ₂ ¹⁹	COB1-CO ₂ ³⁰
Temperature (K)	100	298	298	298	298
Empirical formula	C _{51.50} H _{53.50} CO ₂ N _{6.50} O _{12.50}	C ₄₄ H ₃₆ N ₄ O ₁₀ CO ₂	C ₄₄ H ₃₆ N ₄ O ₁₀ CO ₂	C ₄₄ H ₃₆ N ₄ O ₁₀ CO ₂	C ₄₄ H ₃₆ N ₄ O ₁₀ CO ₂
Formula weight	1081.36	898.66	898.66	898.66	898.66
Wavelength (Å)	0.71073	0.71073	0.71073	0.71073	0.71073
Crystal system	monoclinic	monoclinic	monoclinic	monoclinic	monoclinic
Space group	<i>P</i> 2 ₁ / <i>n</i>	<i>C</i> 2/ <i>c</i>	<i>C</i> 2/ <i>c</i>	<i>C</i> 2/ <i>c</i>	<i>C</i> 2/ <i>c</i>
<i>a</i> , (Å)	29.7813(12)	23.7504(14)	23.7632(11)	30.071(3)	30.075(5)
<i>b</i> , (Å)	15.7987(7)	9.7971(6)	9.8043(5)	7.8976(6)	7.8801(13)
<i>c</i> , (Å)	23.7492(9)	20.3230(12)	20.3897(10)	23.8471(17)	23.860(4)
β , (°)	101.808(2)	104.156(2)	102.360(2)	101.951(4)	102.013(4)
Volume (Å ³)	10937.7(8)	4585.3(5)	4640.3(4)	5540.6(8)	5531.0(16)
Z	8	4	4	4	4
Calculated density (g cm ⁻³)	1.313	1.301	1.286	1.077	1.074
Absorption coefficient (mm ⁻¹)	0.671	0.781	0.772	0.646	0.647
F ₀₀₀	4496	1848	1848	1848	1832
Approx. Crystal size (mm ³)	0.300 × 0.170 × 0.100	0.268 × 0.135 × 0.088	0.268 × 0.135 × 0.088	0.268 × 0.135 × 0.088	0.268 × 0.135 × 0.088
θ range for data collection (°)	1.97 to 26.0	4.52 to 52.9	4.42 to 50.2	1.99 to 26.8	1.99 to 21.3
Miller index ranges	-36 ≤ <i>h</i> ≤ 36 -19 ≤ <i>k</i> ≤ 19 -36 ≤ <i>l</i> ≤ 36	-29 ≤ <i>h</i> ≤ 29 -12 ≤ <i>k</i> ≤ 12, -25 ≤ <i>l</i> ≤ 2	-28 ≤ <i>h</i> ≤ 28 -11 ≤ <i>k</i> ≤ 11 -24 ≤ <i>l</i> ≤ 24	-37 ≤ <i>h</i> ≤ 36, 0 ≤ <i>k</i> ≤ 9 0 ≤ <i>l</i> ≤ 30	-30 ≤ <i>h</i> ≤ 30 -8 ≤ <i>k</i> ≤ 8 -24 ≤ <i>l</i> ≤ 24
Reflections collected	135400	60406	55175	11597	105988
Independent reflections	21507 <i>R</i> _{int} = 0.1097 <i>R</i> _{sigma} = 0.0818	4721 <i>R</i> _{int} = 0.1258 <i>R</i> _{sigma} = 0.0611	4116 <i>R</i> _{int} = 0.1010 <i>R</i> _{sigma} = 0.0448	5776 <i>R</i> _{int} = 0.1658 <i>R</i> _{sigma} = 0.1368	3072 <i>R</i> _{int} = 0.2130 <i>R</i> _{sigma} = 0.1089
Completeness to θ max (%)	0.995	99.9	99.5	98.0	99.9
Refinement method	Full-matrix least-squares on F ²				
Data / restraints / parameters	21507 / 0 / 1081	4721 / 0 / 271	4116 / 0 / 271	5776 / 0 / 430	3072 / 0 / 462
Goodness-of-fit on F	1.021	1.034	1.021	1.236	1.139
Final R indices [<i>I</i> > 2 θ (<i>I</i>)]	<i>R</i> ₁ = 0.0848 <i>wR</i> ₂ = 0.2354	<i>R</i> ₁ = 0.0494 <i>wR</i> ₂ = 0.1000	<i>R</i> ₁ = 0.0428 <i>wR</i> ₂ = 0.0843	<i>R</i> ₁ = 0.1368 <i>wR</i> ₂ = 0.2858	<i>R</i> ₁ = 0.0826 <i>wR</i> ₂ = 0.2111
R indices	<i>R</i> ₁ = 0.1453 <i>wR</i> ₂ = 0.2855	<i>R</i> ₁ = 0.1217 <i>wR</i> ₂ = 0.1371	<i>R</i> ₁ = 0.0791 <i>wR</i> ₂ = 0.0983	<i>R</i> ₁ = 0.1658 <i>wR</i> ₂ = 0.3045	<i>R</i> ₁ = 0.1100 <i>wR</i> ₂ = 0.2456

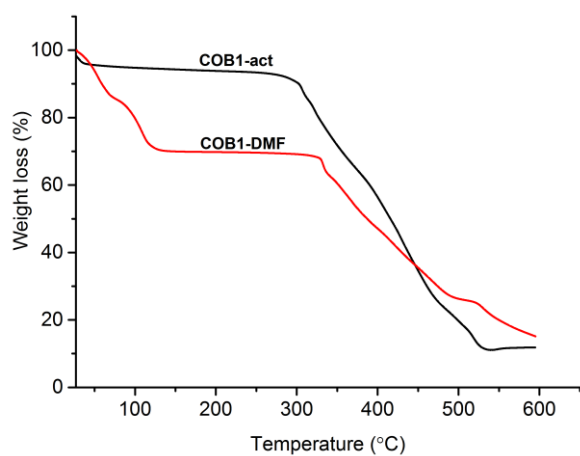
Table S2. Structural phase classification at 298 K.

COB1-DMF	As-synthesised version containing DMF guest molecules
COB1⁰	Host framework determined under vacuum
COB1-CO2¹⁰	Form determined under 10 bar of CO ₂ gas pressure
COB1-CO2¹⁹	Form determined under 19 bar of CO ₂ gas pressure
COB1-CO2³⁰	Form determined under 30 bar of CO ₂ gas pressure

Table S3. Selected distances and angles of **COB1-DMF** and **COB1^x** under controlled CO₂ pressures.

Compound	OBA length (centroid _{SBU} ··· centroid _{SBU}) (Å)	OBA Bend angle (centroid _{SBU} ···O _{ethe} r···centroid _{SBU}) (°)	BPMP length (centroid _{SBU} ··· centroid _{SBU}) (Å)	Acute angle of pyrazine relative to <i>P_{ac}</i> (°)	Co···Co distance (Å)	Paddlewheel acute angle with <i>P_{ac}</i> (°)
COB1-DMF	14.263	119.764	19.029	26.401	2.629	43.910
COB1⁰	14.141	119.208	18.902	84.11	2.749	35.892
COB1-CO2¹⁰	14.144	119.288	18.906	83.903	2.749	35.885
COB1-CO2¹⁹	14.302	120.444	19.142	25.662	2.727	43.991

1. TGA thermograms

**Figure S1.** TGA of **COB1-DMF** and **COB1-act**.

2. Unit cell dimensions and volume as a function of pressure

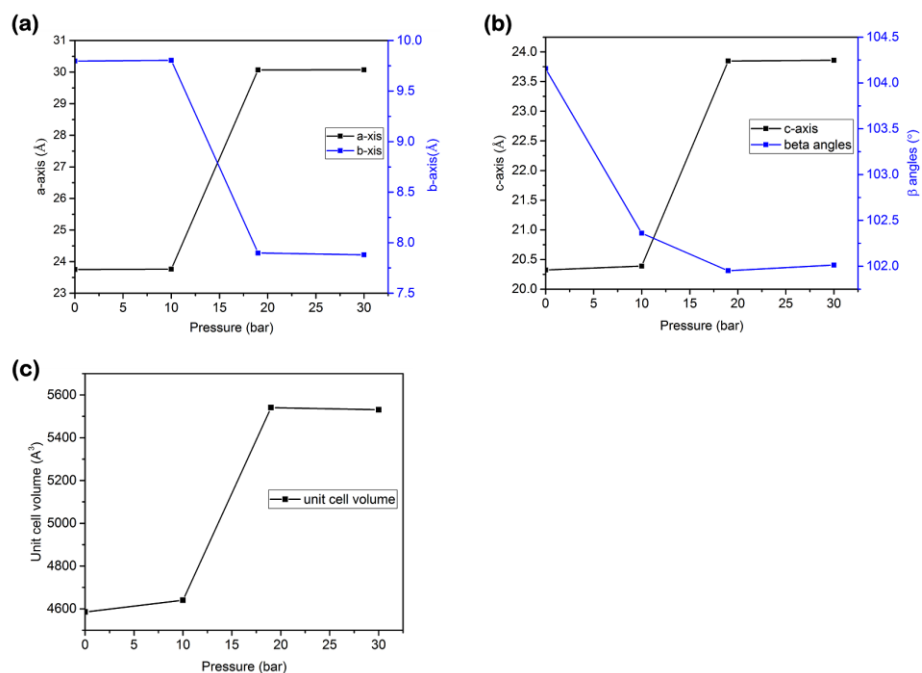


Figure S2. Changes in unit cell parameters for the VP-SCD structures COB1^x , where $x = 0, 10, 19$ and 30 . In situ data were collected at 298 K.

3. Variable temperature PG-DSC under CO_2 pressure

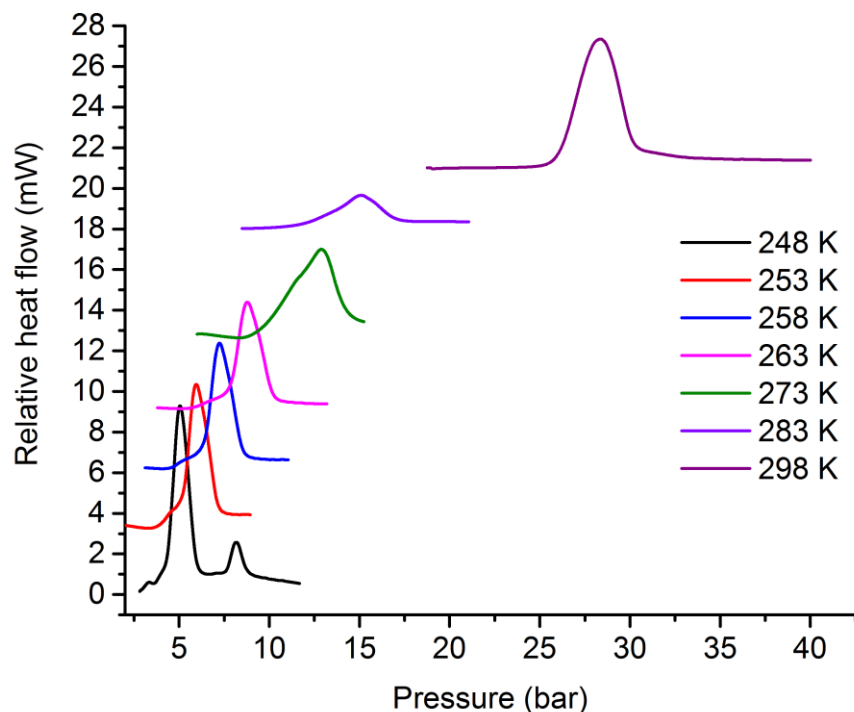


Figure S3. Variable temperature PG-DSC under CO_2 gas pressure.

4. Theoretical investigation

Owing to positional disorder, the apohost crystallographic models obtained under CO₂ pressure were geometry optimized using the CASTEP⁶ code implemented in Materials Studio.⁷ The density functional theory (DFT) generalised gradient approximation of Perdew-Burke-Ernzerhof (PBE)⁸ in combination with Grimme's DFT-D dispersion correction⁹ was employed with on the fly generated Vanderbilt-type ultrasoft pseudopotentials¹⁰ in combination with the Koelling-Harmon scalar-relativistic approach¹¹ and a plane-wave expansion to an energy cutoff of 489.8 eV. Integration in the reciprocal lattice was performed using a Monkhorst-Pack grid¹² with a 0.05 Å⁻¹ k-point separation and self-consistent field convergence was set to 2.0 × 10⁻⁶ eV. A 50% admixture of the charge density¹³ was applied in conjunction with a DIIS (direct inversion in an iterative subspace)¹⁴ size of 20 to speed up convergence. Convergence tolerances for geometry optimization using the BFGS (Broyden-Fletcher-Goldfarb-Shanno) algorithm¹⁵ were set to 2.0 × 10⁻⁵ eV atom⁻¹, 0.05 eV Å⁻¹ and 0.002 Å on energy, maximum force and maximum displacement respectively. To reduce computational expense, calculations were carried out in the primitive cell representation with

$$a' = b' = \sqrt{a^2 + b^2}/2$$

$$c' = c$$

$$\cos(\gamma'/2) = a/\sqrt{a^2 + b^2}$$

$$\cos^2 \alpha' = \cos^2 \beta' = \frac{\sin^2 \gamma' - (2ab \sin \beta / (a^2 + b^2))^2}{2 - 2 \cos \gamma'}$$

since $V' = V/2$, as shown in Figure S4.

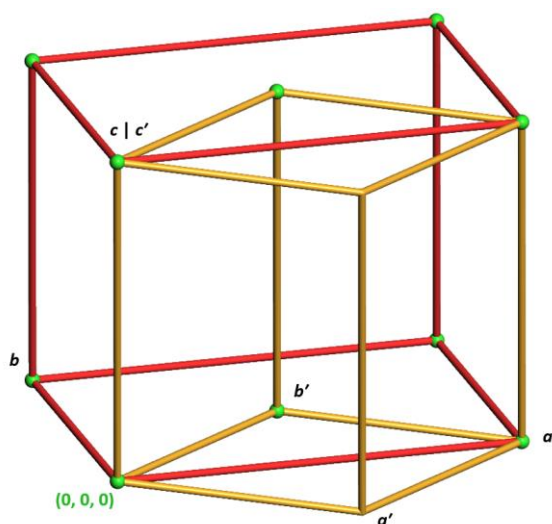


Figure S4. Overlay of conventional and primitive representations of a face-centred monoclinic unit cell in red and orange, respectively. Lattice points are indicated as green spheres.

Table S3. Guest-omitted unit cell energies (kcal mol⁻¹) relative to that of COB1⁰.

COB1-DMF	54.65
COB1 ⁰	0
COB1-CO2 ¹⁰	0.058
COB1-CO2 ¹⁹	45.26
COB1-CO2 ³⁰	56.36

Attempting to model the CO₂-induced gate opening through an incremental perturbing of the unit cell parameters (10 bar → 19 bar) rendered the ligands far removed from their crystallographic orientations. A linear synchronous transit approach was subsequently applied to geometrically follow the structural transformation.¹⁶ A molecular fragment representing a complete coordination sphere of the Co₂OBA₂ paddlewheel was extracted from the geometry optimised 10 bar and 19 bar crystal structures and each atom paired after translocation to the same origin. The resulting pathway shown in Video S1 reveals a major contortion of the BPMP ligand, while the Co₂OBA₂ paddlewheel undergoes a reorientation. Since OBA links paddlewheels along the (0±12) Miller planes, viewing down [0±21] sheds light on the BPMP contribution to the transformation. Similarly, BPMP bridges paddlewheels along (3±10) allowing the [1±30] view to highlight the contortion of the OBA ligand. The rotation of the piperazine moiety from nearly perpendicular (83.90°) to acute (25.66°) during the course of the transformation is discernible in the view down the c axis in **Figure S4** below.

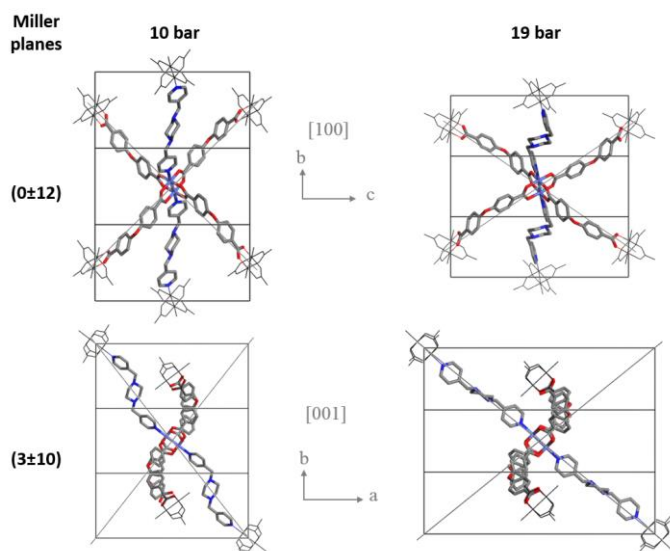


Figure S4. Comparison of CO₂-adsorption induced gate opening structural transformation. Miller planes along which the two ligands interconnect paddlewheel moieties are shown.

5. Description of video files

Video S1 shows the CO₂-induced gate opening transformation of the framework from **COB1-CO2**¹⁰ to **COB1-CO2**¹⁹. Expanding the mechanism derived for the fragment into a crystallographic representation, Video S2 shows the gradual increase in solvent-accessible space. These video files are best viewed with the video player set to loop.

References

1. D. Pocic, J. Planeix, N. Kyritsakas, A. Jouaiti, M. Hosseini, *CrystEngComm*. 2005, **7**, 624.
2. *SAINT Data Reduction Software*, Version 6.45; Bruker AXS Inc., Madison, WI, 2003.
3. (a) *SADABS*, Version 2.05; Bruker AXS Inc., Madison, WI, 2002; (b) Blessing, R. H. *Acta Crystallogr., Sect. A: Found. Crystallogr.* 1995, **51**, 33.
4. G. M. Sheldrick, *Acta Crystallogr., Sect. A: Found. Crystallogr.* 2008, **64**, 112.
5. (a) L. J. Barbour, *J. Supramol. Chem.* 2001, **1**, 189; (b) L.J. Bourhis, O.V. Dolomanov, R.J. Gildea, J.A.K. Howard, H. Puschmann, *Acta Cryst.* 2015. **A71**, 59.
6. S. J. Clark, M. D. Segall, C. J. Pickard, P. J. Hasnip, M. J. Probert, K. Refson, M. C. Payne, *Z. Kristallogr.* 2005, **220**, 567.
7. Dassault Systèmes BIOVIA, Materials Studio, Release 18, San Diego: *Dassault Systèmes*, 2017.
8. J. P. Perdew, K. Burke, M. Ernzerhof, *Phys. Rev. Lett.* 1996, **77**, 3865
9. S. Grimme, *J. Comput. Chem.* 2006, **27**, 1787.
10. D. Vanderbilt, *Phys. Rev. B* 1990, **41**, 7892.
11. D. D. Koelling, B. N. Harmon, *J. Phys. C* 1977, **10**, 3107.
12. H. J. Monkhorst, J. D. Pack, *Phys. Rev. B* 1976, **13**, 5188.
13. G. Kresse, J. Furthmuller, *Phys. Rev. B* 1996, **54**, 11169.
14. P. Pulay, *Chem. Phys. Lett.* 1980, **73**, 393.
15. B. G. Pfrommer, M. Cote, S. G. Louie, M. L. Cohen, *J. Comput. Phys.* 1997, **131**, 233.
16. A. Halgren, W. N. Lipscomb, *Chem. Phys. Lett.* 1977, **49**, 225.

CHAPTER 4

A new interdigitated porous coordination polymer that exhibits flexibility and highly hysteretic shape recovery with CO₂ sorption and desorption at 298 K

4.1. Manuscript not yet submitted

Contributions of the author:

- ✓ Design of project
- ✓ Preparation of the new MOF
- ✓ Collection of single-crystal X-ray data
- ✓ Solution and refinement of single-crystal X-ray structure
- ✓ Recording of PXRD patterns
- ✓ Recording of TGA thermograms
- ✓ Sorption analysis
- ✓ Interpretation of results with Len
- ✓ Writing the first draft of the article

A new interdigitated porous coordination polymer that exhibits flexibility and highly hysteretic shape recovery with CO₂ sorption and desorption at 298 K

Received 00th January 20xx,
Accepted 00th January 20xx

DOI: 10.1039/x0xx00000x

Phumile Sikiti and Leonard J. Barbour*

Department of Chemistry and Polymer Science, University of Stellenbosch, Matieland 7602, South Africa

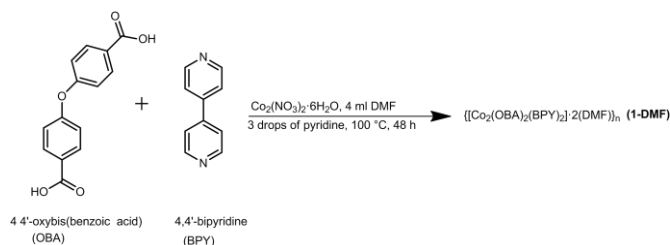
A new interpenetrated two dimensional porous coordination polymer $\{[Co_2(OBA)_2(BPY)_2] \cdot 2DMF\}_n$ (1-DMF**) possesses structural flexibility and displays hysteretic sorption of CO₂ gas at 298 K. The structural flexibility upon activation by desolvation has been characterised by means of single-crystal X-ray diffraction. Activation of **1-DMF** causes distortion of the coordination geometry, with concomitant sliding of mutually interdigitated layers. The structural change due to CO₂ uptake beyond 27 bar is evidenced by *in situ* variable-pressure powder X-ray diffraction. Although the CO₂ sorption isotherm appears to indicate shape memory, the powder diffraction results show that desorption results in recovery of the activated form. Closer inspection of the low-pressure desorption data confirms this observation.**

Porous coordination polymers (PCPs) and metal-organic frameworks (MOFs) are a class of materials constructed from inorganic ions/clusters bridged by organic linkers.¹ Owing to intrinsic properties such as structural and compositional diversity, tunable functionality, high surface areas² and adjustable pores, PCPs often permit reversible guest uptake and removal.³ PCPs have recently been investigated extensively for various applications that include molecular sensing,⁴ catalysis,⁵ and gas or liquid separations.⁶ Some PCPs are known to be flexible and undergo processes such as pressure-induced phase transitions in the presence of certain gases.⁷ The mechanisms for these structural transitions have been shown to involve breathing, swelling, linker rotation, and subnetwork displacement.⁸ The pressure-induced structural changes greatly affect the sorption behaviour of the materials and generally give rise to stepped sorption profiles;⁹ transformation from a narrow-pore to a wide-pore form is evidenced by a sudden increase in gas uptake.¹⁰ Such flexible materials present opportunities for improved performance in applications that take advantage of selective adsorption properties.¹¹ Owing to the crystallinity of flexible PCPs and MOFs, their structures are primarily characterised using *in-situ* powder X-ray diffraction

(PXRD) analysis under gas pressure,¹² and only a handful of such materials have been characterised using *in situ* single-crystal diffraction (SCD) methods under gas pressure at relevant conditions.^{8,9} Structural investigation of flexible materials under relevant non-ambient conditions is becoming an increasingly active area of research.

Here we report the preparation and characterisation of a new PCP $\{[Co_2(OBA)_2(BPY)_2] \cdot 2DMF\}_n$ (**1-DMF**, where OBA = 4,4'-oxybis(benzoic acid) and BPY = 4,4'-bipyridine). **1-DMF** undergoes activation by means of simple desolvation as a single-crystal to single-crystal transformation. SCD analysis reveals that this phase change involves distortion of the coordination geometry with ligand, as well as concomitant sliding of interdigitated layers relative to one another. The activated form yields a stepped sorption isotherm when exposed to CO₂ gas.

Pink plate-shaped crystals of the solvated PCP **1-DMF** were prepared according to the procedure outlined in Scheme 1. A



Scheme S1. Synthesis of $\{[Co_2(OBA)_2(BPY)_2] \cdot 2(DMF)}_n$ (**1-DMF**)

suitable crystal was selected and subjected to SCD analysis at 100 K; **1-DMF** crystallises in the monoclinic space group $C2/c$ (Table S1) and the asymmetric unit (Fig. S1) consists of a cobalt ion, an OBA ligand, a BPY ligand and a DMF molecule disordered over two positions of approximately equal occupancy. The structure is characterised by a two dimensional coordination network based on two centrosymmetrically-related Co²⁺ ions, each in a distorted octahedral geometry where it is coordinated

Department of Chemistry and Polymer Science, University of Stellenbosch, Matieland, 7600, South Africa E-mail: ljb@sun.ac.za; Fax: (+27) 21-808-3360

† Electronic supplementary information (ESI) available: SCD, sorption, PXRD, Crystallographic Information Files CCDC 1852200-1852201.

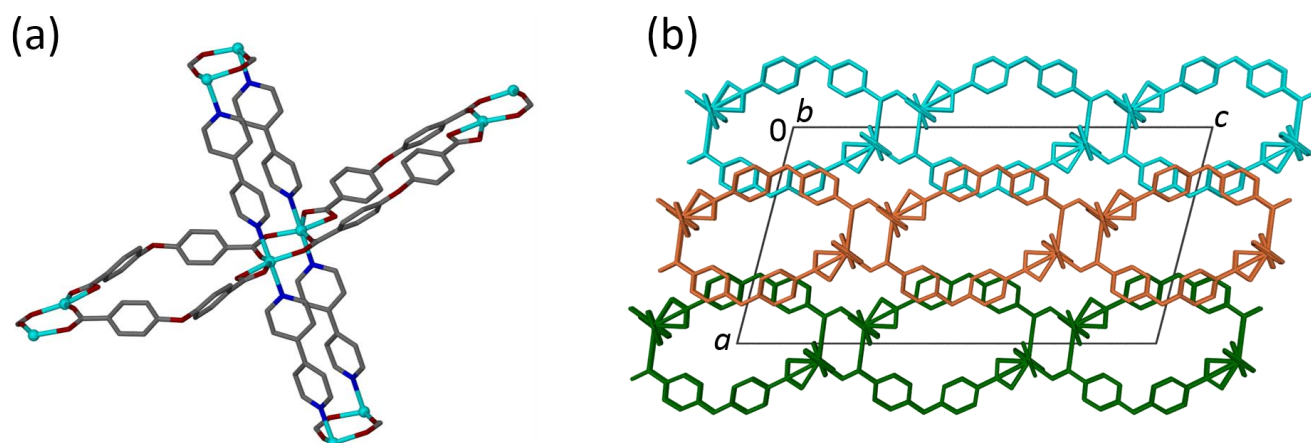


Fig. 1 (a) Coordination environment of **1-DMF** showing the interconnection of Co_2^+ -based secondary building units by means of bridging ligands. (b) Perspective view of **1-DMF** along [010] showing two dimensional layers parallel to the bc plane, and interdigitation of adjacent layers (shown in different colours so that separate layers can be easily identified). Interdigitation involves overlap of OBA ether moieties of adjacent layers. Hydrogen atoms and DMF guest molecules have been omitted for clarity.

to two BPY ligands at the axial positions, one OBA carboxylate ion in chelating mode, and to two oxygen atoms from two different OBA carboxylate groups in bridging mode (Fig. 1a). The double-stranded OBA linkages produce one dimensional chains that propagate parallel to the crystallographic c axis. These chains are cross-linked along b by means of BPY ligands to generate two dimensional layers parallel to the bc plane, and

neighbouring planes are mutually interdigitated (Fig. 1b). The disordered DMF molecules are situated in discrete solvent-accessible virtual voids,¹³ of which there are eight symmetry-related instances per unit cell. Each void has a total contact surface volume of approximately 140 \AA^3 (estimated by Mercury¹⁴ using a probe radius of 1.5 \AA and a grid spacing of 0.2 \AA , Fig. 2a left). Phase purity of the bulk material was confirmed

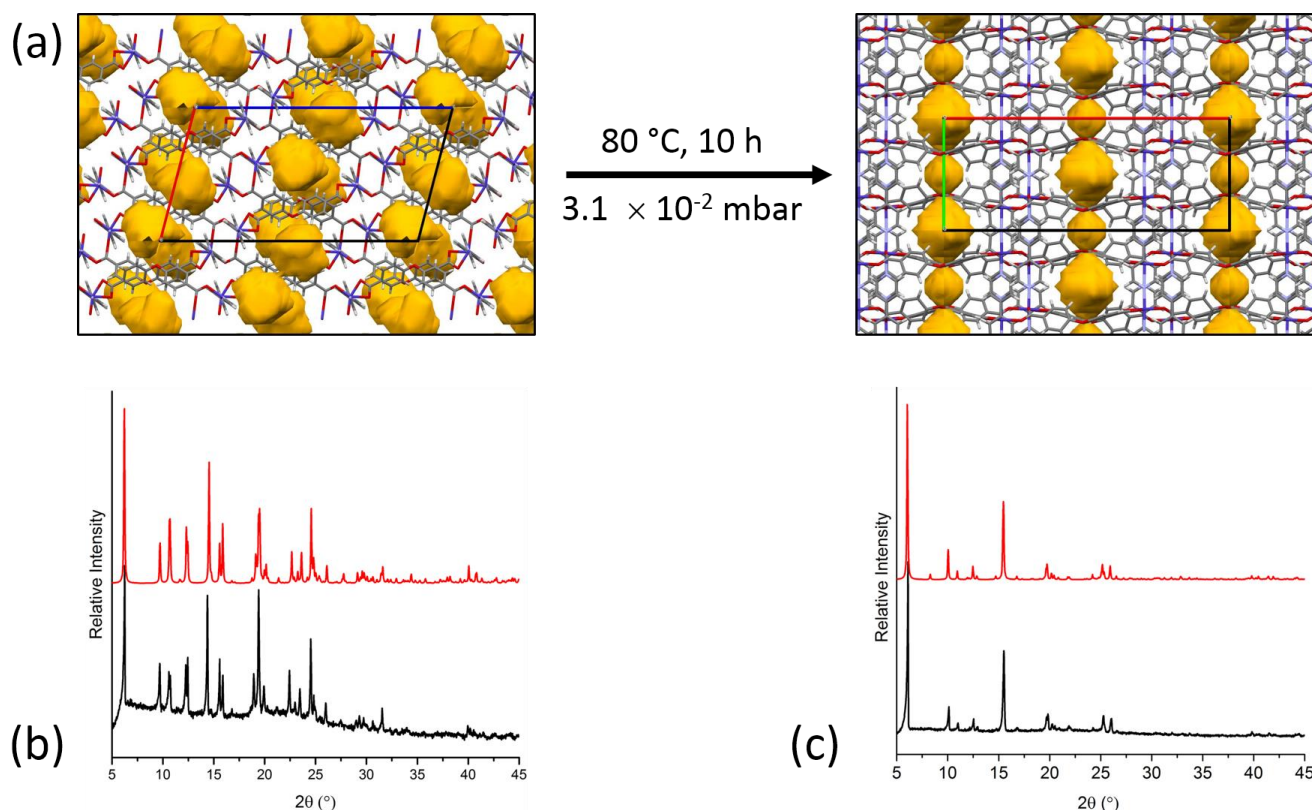


Fig. 2 (a) Projections of **1-DMF** and **1-act**, showing the reduction in the guest-accessible space (yellow surfaces) upon activation. (b) PXRD diffractogram of **1-DMF** recorded at 298 K (black) and simulated from the SCD structure (red). (c) PXRD diffractogram of **1-act** recorded at 298 K (black) and simulated from the SCD structure (red). The SCD structure of **1-DMF** was determined at 100 K while **1-act** were determined at 298 K.

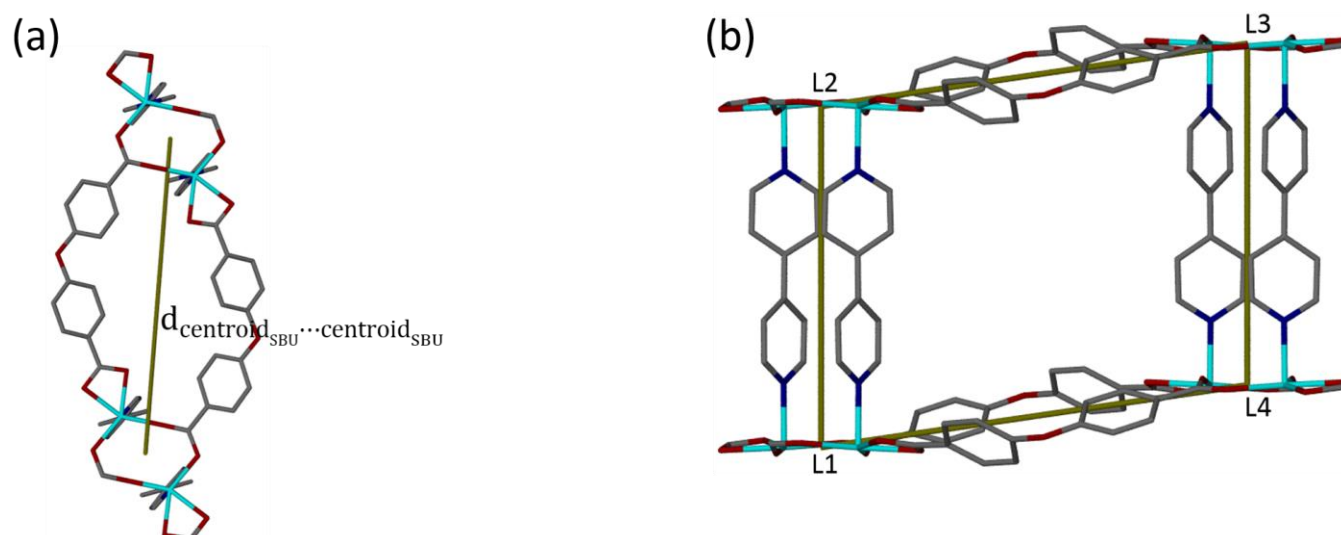


Fig. 3 (a) Measures from centroid to centroid of Co_2 -based secondary units and (b) Square block Co_2 -based secondary units represented by L1, L2, L3 and L4.

by PXRD analysis (i.e. despite the differences in temperature, the PXRD pattern simulated from the crystal structure of **1-DMF** corresponds well to that measured for the bulk material (Fig. 1b).

Thermogravimetric analysis (TGA) of **1-DMF** shows a weight loss of approximately 20% in the range 25 to 120 °C (Fig. S2), which corresponds to one **DMF** guest molecule per host formula unit. It appears that the framework starts to decompose after 300 °C. A bulk sample of **1-DMF** was activated at 80 °C under dynamic vacuum (3.1×10^{-2} mbar) for 10 hours, after which TGA showed that the DMF had been removed. PXRD analysis of the activated sample (Fig. 2c) confirmed retention of crystallinity and conversion to a new phase, hereafter referred to as **1-act**. A crystal suitable for SCD was selected and intensity data recorded at 298 K reveal that **1-act** is a new reduced-pore form, the structure of which is consistent with the PXRD pattern for

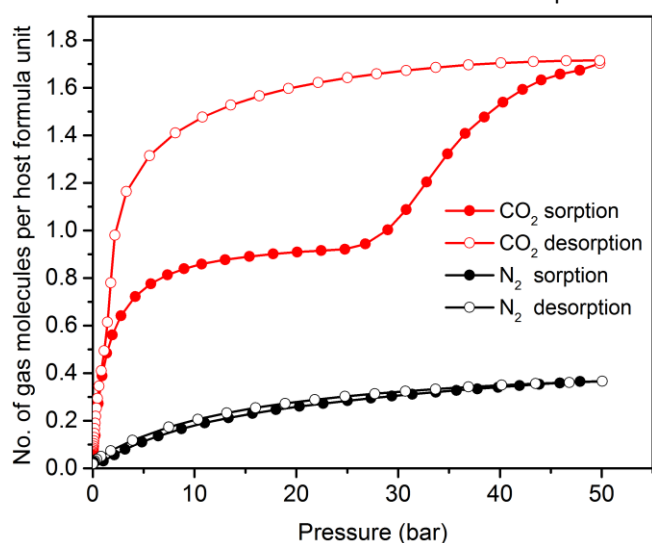


Fig. 4 N_2 and CO_2 sorption/desorption isotherms for **1-act** recorded 298 K.

the bulk activated material (Fig. 2a right and Table S1, ESI⁺). We note that activation results in severe degradation of single-crystal quality. However, it was still possible to obtain a model that allows comparison of the phases before and after activation, albeit that the final model is not suitable for publication. Besides poor data, the OBA ligand of **1-act** is disordered over two different positions. Nevertheless, it is apparent that for either of these positions, the host network connectivity remains intact, although activation results in a 7% reduction in the unit cell volume. Indeed, it is well established that such phase changes can arise through structural distortions involving changes in bond lengths and angles.¹⁵ In order to understand the phase change that occurs upon desolvation, the structural geometries and moiety conformations of **1-DMF** and **1-act** were compared. The conformation of OBA is largely preserved and the centroid...centroid distances of the Co_2 SBUs across the OBA ligands remain unchanged (Fig. 3a). However, the centroid_{SBU}...centroid_{SBU} vectors L1...L2...L3...L4 shown in Fig. 3b change from describing a parallelogram in **1-DMF** (with an internal angle L1...L2...L3 = 98°) to a rectangle in **1-act** (see Fig. S3). Consequently, the interlayer spacing between adjacent mutually interdigitated layers changes from 7.59 Å in **1-DMF** to 5.5 Å in **1-act**, thus resulting in a decrease in the total amount of guest-accessible space. The eight crystallographically-related voids per unit cell of **1-DMF** become transformed (Fig. 1a) such that **1-act** contains two types of voids, one slightly larger than the other (with four of each per unit cell). We note that, although neither **1-DMF** nor **1-act** contains permanent pores, it is well known that many such materials are still capable of facilitating guest transport by means of a mechanism that involves the dynamic formation of short-lived transient channels between adjacent voids.¹³

To explore the potential porosity of **1-act**, gas sorption analyses were carried out at 298 K using CO_2 and N_2 up to pressures of 50 bar (Fig. 4). The smooth type I sorption isotherm

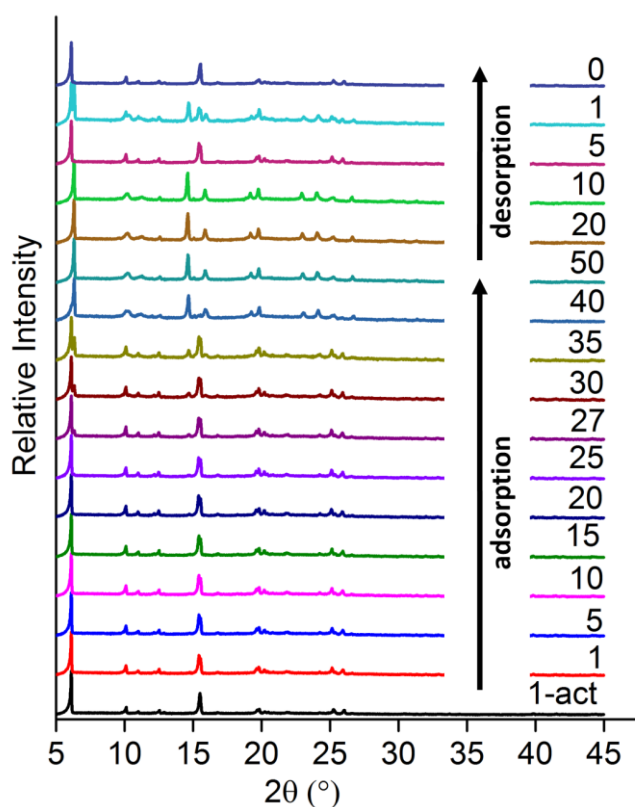


Fig. 5 *In situ* VP-PXRD patterns recorded at 298 K under controlled CO₂ pressures during both sorption and desorption.

recorded for N₂ shows a maximum loading of 0.38 molecules per host formula unit at 50 bar. However, in the case of CO₂ the sorption isotherm contains a step with an onset pressure of 27 bar, at which the CO₂ uptake is approximately 0.9 molecules per host formula unit. Upon further increase in pressure, additional CO₂ is adsorbed with apparent saturation being reached at 50 bar, where the total uptake is approximately 1.8 molecules of CO₂ per host formula unit. Such stepped profiles are usually associated with gate-opening phase changes, and the sorption isotherm therefore implies that a structural transformation occurs after 27 bar.^{8,9} Pronounced hysteresis is evident upon desorption and, interestingly, no obvious step is observed during CO₂ release (i.e. the desorption isotherm exhibits a type I profile). This observation is consistent with the phenomenon of shape-memory, which occurs when the gate-opening step is not reversible and the host material retains its gas-loaded form upon guest release.¹⁵

To confirm whether a phase change occurs during CO₂ sorption, as well as possible shape-memory upon subsequent desorption, *in situ* variable-pressure PXRD analysis (VP-PXRD) (Fig. 5) was carried out at 298 K using an environmental gas cell. A powdered sample of **1-act** was subjected to vacuum for 2 hours and then pressurised incrementally with CO₂ gas; a diffractogram was recorded at 298 K for each pressure. The PXRD patterns from 1 to 25 bar show no phase transition relative to **1-act**. However, at 27 bar small changes and peak broadening can be observed at low 2θ values, thus signalling the onset of a phase change. This result is consistent with the

sorption isotherm (Fig. 4). In the 27 to 35 bar range, new peaks gradually emerge and it appears that there is a mixture of two phases. Thereafter, the new phase dominates and persists until 50 bar. Unfortunately, it was not possible to obtain SCD data for this new phase because the single crystal did not survive the transition intact. It is therefore impossible (at this time) to provide a detailed structural mechanism for the gate opening event that allows additional uptake of CO₂ in the range 27 to 50 bar. The PXRD pattern recorded at 1 bar during desorption appears to show the presence of a mixture of phases and that recorded at 0 bar after complete desorption of CO₂ shows that the original activated form is recovered. This implies that the material does not exhibit shape memory upon complete desorption. Indeed, closer inspection of the desorption isotherm in the range 0 to 6 bar (Fig. S4b) shows that there is a subtle step with an onset pressure of between 2 and 1 bar, and this step is most likely due to recovery of the original activated phase. The 26 bar hysteresis associated with reversibility of the breathing mechanism is unusually large and warrants further investigation.

In summary, we have produced a new PCP that can be activated in single-crystal to single-crystal fashion. The activated phase undergoes a further phase change associated with gate-opening upon exposure to CO₂ gas at pressures above 27 bar at 298 K. The gate-opening mechanism most likely involves sliding of interdigitated two dimensional layers relative to one another, but this could not be confirmed by means of *in situ* SCD analysis. Although the sorption isotherm appeared to indicate shape memory, detailed *in situ* powder diffraction analysis showed that this is not the case. Indeed, closer inspection of the sorption isotherm reveals that a gate-closing event occurs at relatively low pressure, with substantial hysteresis for the reversibility of this interesting phenomenon. Further studies that employ pressure-gradient differential scanning calorimetry are warranted. It is also necessary to investigate milder activation conditions, as well as the possibility of retaining single-crystal quality during the CO₂-induced phase change in order to obtain a more complete assessment of the flexibility of the framework.

The authors thank the National Research Foundation of South Africa for financial support.

Notes and references

1. Y. Yan, A. E. O'Connor, G. Kanthasamy, G. Atkinson, D. R. Allan, A. J. Blake, Martin Schröder. *J. Am. Chem. Soc.* 2018, **140**, 3952. (a) O. K. Farha, I. Eryazici, N. C. Jeong, B. G. Hauser, C. E. Wilmer, A. A. Sarjeant, R. Q; Snurr, S. T. Nguyen, A. O. Yazaydin and J. Hupp, *J. Am. Chem. Soc.*, 2012, **134**, 15016.
2. Z. Chen, L. J. Weselinski, K. Adil, Y. Belmabkhout, A. Shkurenko, H. Jiang, P. M. Bhatt, V. Guillerm, E. Duzon, D. X. Xue, M. O'Keeffe and M. Eddaoudi, *J. Am. Chem. Soc.*, 2017, **139**, 3265.
3. E. L. Kreno, K. Leong, O. K. Farha, A. Richard P. V. Duyne, J. T. Hupp. *Chem. Rev.* 2012, **112**, 1105.
4. L. Ma, C. Abney, W. Lin. *Chem. Soc. Rev.*, 2009, **38**, 1248.
5. S. Mukherjee, B. Joarder, A. V. Desai, B. Manna, R. Krishna, S. K. Ghosh. *Inorg. Chem.*, 2015, **54**, 4403.

6. R. Kitaura, K. Seki, G. Akiyama, S. Kitagawa. *Angew. Chem. Int. Ed.* 2003, **42**, No. 4.
7. A. Schneemann, V. Bon, I. Schwedler I. Senkovska, b S. Kaskel, R. A. Fischer. *Chem. Soc. Rev.*, 2014, **43**, 6062.
8. P. Lama, H. Aggarwal, C. X. Bezuidenhout L. J. Barbour. *Angew. Chem. Int. Ed.* 2016, **55**, 13271; *Angew. Chem.* 2016, 128, 13465.
9. P. Lama and L. J. Barbour. *J. Am. Chem. Soc.*, 2018, **140**, 2145.
10. J. A. Mason, J. Oktawiec, M.K. Taylor, M. Hudson, J.; Rodriguez, J. E. Bachman, M. I.; Gonzalez, A. Cervellino, A. Guagliardi, C. M Brown, P. L. Llewellyn, N, Masciocchi and J. R. Long, *Nature*, 2015, **527**, 357.
11. (a) V. Bon, I. Senkovska, D. Wallacher, A. Heerwig, N. Klei I. Zizak, R. Feyerherm, E. Dudzik. S. Kaskel. *Microporous and Mesoporous Materials*. 2014, **188**, 190; (b) A. Schneemann, P. Vervoorts, I. Tu. M. Hante, S. Wannapaiboon, C.; Sternemann, M, Paulus, D.C. F. Wieland, S. Henke and R. A. Fischer, *Chem. Mater.*, 2018, **30**, 1667; (c) R. E. Morris and L. Brammer, *Chem. Soc. Rev.* 2017, **46**, 5444.
12. L. J. Barbour. *Chem. Commun.*, 2006, 1163.
13. Connolly, M. L. *J. Mol. Graphics*. 1993, **11**, 139.
14. M. Shivanna, Q. Y. Yang, A. Bajpai, E. Patyk-Kazmierczak and M. J. Zaworotko, *Nat. Commun.*, 2018, **9**, 3080.

4.2. SUPPORTING INFORMATION

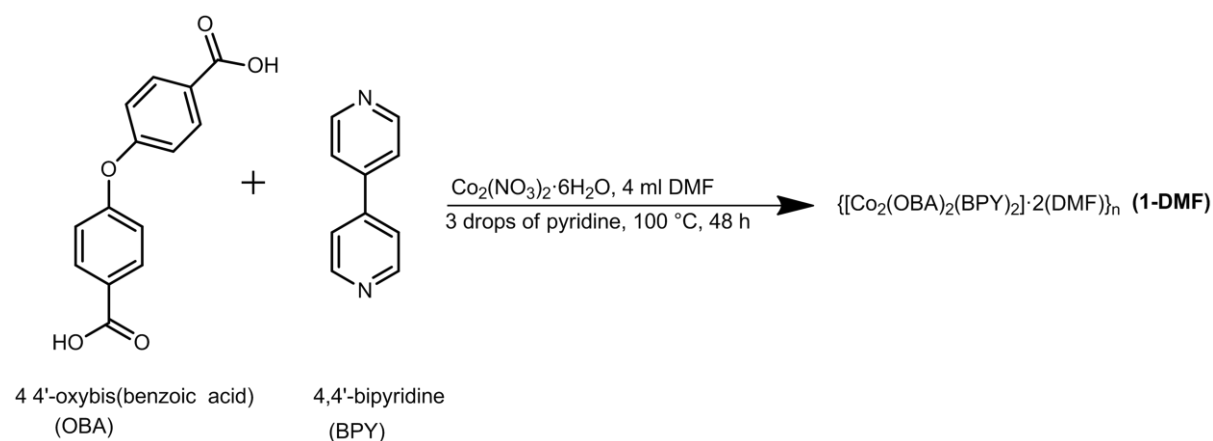
A new interdigitated porous coordination polymer that exhibits flexibility and highly hysteretic shape recovery with CO₂ sorption and desorption at 298 K

Materials

All chemicals and solvents were purchased from Aldrich and used without further purification.

Preparation of 1-DMF

$\{[\text{Co}_2(\text{OBA})_2(\text{BPY})_2] \cdot 2\text{DMF}\}_n$ (**1-DMF**): CO₂(NO₃)₂·6H₂O (1 mmol), 4,4'-oxybis(benzoic acid) (OBA, 1 mmol) and 4,4'-bipyridine (BPY, 1 mmol) were mixed in 4 ml of dimethylformamide (DMF) and 3 drops of pyridine were added. The solution was placed in a pre-heated oven at 100 °C. Pink plate-shape crystals were obtained after 48 h.



Scheme S1. Synthesis of $\{[\text{Co}_2(\text{OBA})_2(\text{BPY})] \cdot 2(\text{DMF})\}_n$ (**1-DMF**)

Activation method of 1-DMF

1-DMF was activated at 80 °C under dynamic vacuum (3.1×10^{-2} mbar) for 8 hours to yield the fully desolvated form **1-act**.

Single-crystal X-ray diffraction

Single crystal X-ray diffraction data were collected on a Bruker APEX-II Quasar CCD area-detector diffractometer equipped with an Oxford Cryostream 700Plus cryostat, and on a Bruker D8 venture PHOTON II CPAD detector equipped with an Oxford Cryostream 800Plus cryostat. A multilayer monochromator with $\text{MoK}\alpha$ radiation ($\lambda = 0.71073 \text{ \AA}$) from an Incoatec $I_{\mu\text{S}}$ microsource was used. Data reduction was carried out by means of standard procedures using the Bruker software package SAINT¹ and absorption corrections and the correction of other systematic errors were performed using SADABS.² The structures were solved by direct methods using SHELXS-2016 and refined using SHELXL-2016³ and X-Seed⁴ was used as the graphical interface for the SHELX program suite. Hydrogen atoms were placed in calculated positions using riding models. All of the non-bonding distances and angles were measured using the program X-Seed⁴ and Diamond Version 3.0. Some of the figures were generated using OLEX² crystallographic software⁴ (version 1.2.9) and X-Seed/MSROLL.^{4,5}

Owing to significant crystal degradation, most likely due to the strain introduced by desolvation, the intensity data for **1-act** were poor. Moreover, the OBA ligand appears to be disordered over two positions, which were modelled with almost equal occupancy. The crystal structure was therefore refined isotropically; before publication of this result in a journal, milder activation conditions need to be investigated in order to improve the quality of the crystal structure. However, the crystal structure analysis in hand is sufficient to allow comparison of the structures before and after activation. The asymmetric units of **1-DMF** and **1-act** are shown in Figures S1a and S1b, respectively.

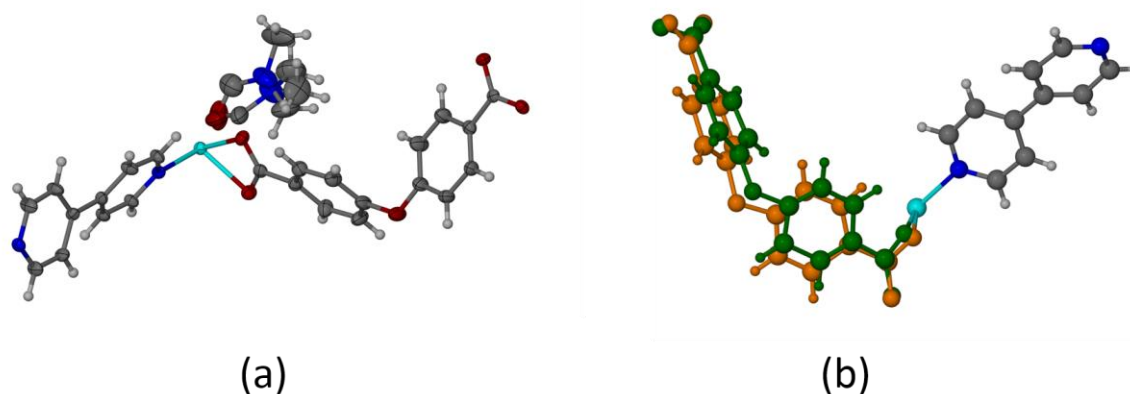


Figure S1 Thermal ellipsoid plot of the asymmetric units of (a) **1-DMF** and (b) **1-act**.

Table S1. Crystallographic table of **1-DMF** and **1-act**

Complex Name	1-DMF	1-act
Temperature (K)	100	298
Empirical formula	C ₂₇ H ₂₃ N ₃ O ₆ Co	C ₂₄ H ₁₆ CoN ₂ O ₅
Formula weight	544.41	471.32
Wavelength (Å)	0.71073	0.71073
Crystal system	monoclinic	monoclinic
Space group	<i>C2/c</i>	<i>C2/c</i>
<i>a</i> , (Å)	15.6815(17)	30.099(9)
<i>b</i> , (Å)	11.3713(13)	11.441(3)
<i>c</i> , (Å)	29.386(4)	14.144(4)
β, (°)	104.588(3)	104.024(5)
Volume (Å ³)	5071.2(10)	4728(2)
Z	8	8
Calculated density (gcm ⁻³)	1.426	1.324
Absorption coefficient (mm ⁻¹)	0.724	0.761
F000	2248	1936
Approx. Crystal size (mm ³)	0.323 × 0.236 × 0.142	0.137 × 0.115 × 0.097
θ range for data collection (°)	2.24 to 28.45	2.315 to 24.027
Miller index ranges	-17 ≤ <i>h</i> ≤ 20, -15 ≤ <i>k</i> ≤ 15 39 ≤ <i>l</i> ≤ 37	26 ≤ <i>h</i> ≤ 26, -10 ≤ <i>k</i> ≤ 10, -12 ≤ <i>l</i> ≤ 12
Reflections collected	29373	21642
Independent reflections	6308 <i>R</i> _{int} = 0.1151	1813 <i>R</i> _{int} = 0.0927
Completeness to θ max (%)	0.987	0.997
Refinement method	Full-matrix least-squares on <i>F</i> ²	Full-matrix least-squares on <i>F</i> ²
Data / restraints / parameters	6308 / 0 / 321	3705 / 0 / 284
Goodness-of-fit on <i>F</i> ²	1.024	1.070
Final R indices [I > 2 σ(I)]	<i>R</i> ₁ = 0.0869 <i>wR</i> ₂ = 0.2039	<i>R</i> ₁ = 0.0966 <i>wR</i> ₂ = 0.2510
R indices	<i>R</i> ₁ = 0.1673 <i>wR</i> ₂ = 0.2584	<i>R</i> ₁ = 0.1216 <i>wR</i> ₂ = 0.2731

Thermogravimetric analysis

Thermogravimetric analysis was carried out using a TA Instruments Q500 analyser. The sample was loaded in an aluminium pan and heated at 10 °C/min from room temperature up to 600 °C. The TGA thermograms of **1-DMF** and **1-act** are shown in Figure S1.

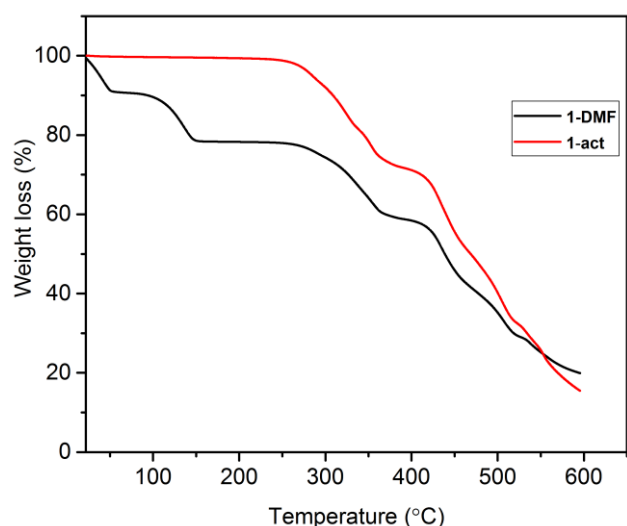


Figure S2 TGA of **1-DMF** and **1-act**.

Comparison of the framework geometries of **1-DMF** and **1-act**

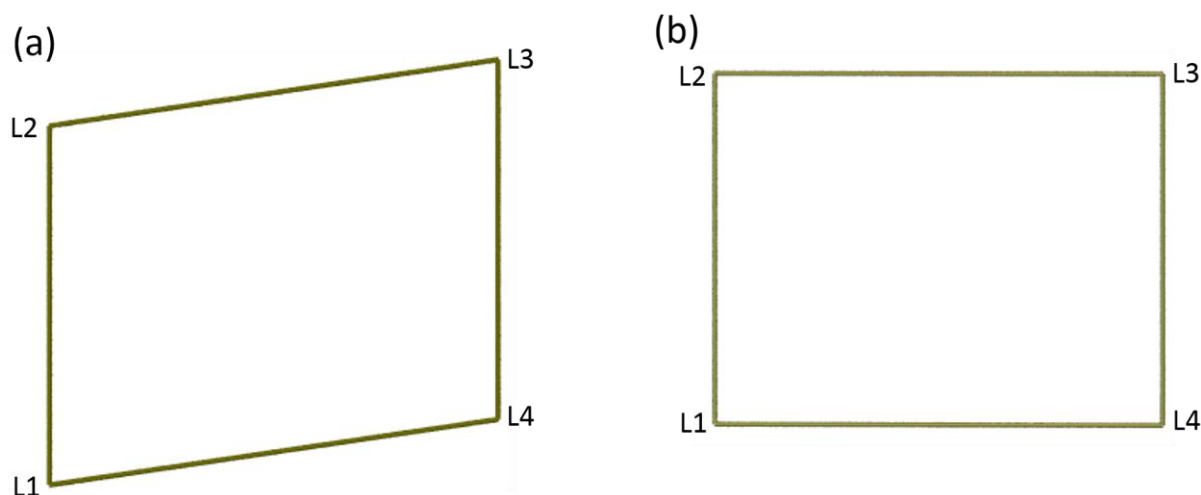


Figure S3. Vectors joining CO₂ SBU centroids in 2D grids of (a) **1-DMF** and (b) **1-act**.

Powder X-ray diffraction (PXRD)

Experiments were carried out on a PANalytical X'Pert PRO instrument in transmission mode. Intensity data were recorded using an X'Celerator detector and 2θ scans were performed in the range of 5-40°. During the experiment the powdered sample was exposed to Cu-K α radiation ($\lambda = 1.5418 \text{ \AA}$). Samples were sealed within a glass capillary (environmental gas cell) and the capillary spinner configuration (with focusing mirror) of the instrument was used since this setup allows for very accurate temperature control using an Oxford Cryostream 700 Plus cryostat. Carbon dioxide was used to pressurize **1-act** and its variable pressure PXRD patterns were measured at a constant temperature of 298 K.

Volumetric sorption analysis

A Setaram PCTPro-E&E gas sorption analyser with MicroDoser attachment was utilised to conduct high pressure gas sorption experiments with gases such as N₂ and CO₂ at 298 K. The instrument is a volumetric gas analyser which utilises Sievert's volumetric method. The sample temperature was maintained to an accuracy of ± 1 °C using a Grant refrigerated recirculation bath filled with antifreeze and water. A sample at known pressure and volume was connected to a reservoir of known volume and pressure through an isolation valve. The valve was opened and the system allowed to equilibrate. The difference between the measured pressure and calculated pressure was used to determine the amount of gas adsorbed. NIST software was used to calculate the thermodynamic corrections in order to account for the non-ideal behaviour of the gases at relatively high pressures. The PCTPro-E&E with the MicroDoser attachment is used for small sample sizes and has a range of vacuum to 60 bar. Sample sizes of 100-120 mg were used and activated in-situ using vacuum and heat. Blank runs for each gas were recorded to further correct for any other residual systematic errors in the experiment. The sorption/desorption isotherms are shown in Figure S4. The figure was prepared using OriginPro.

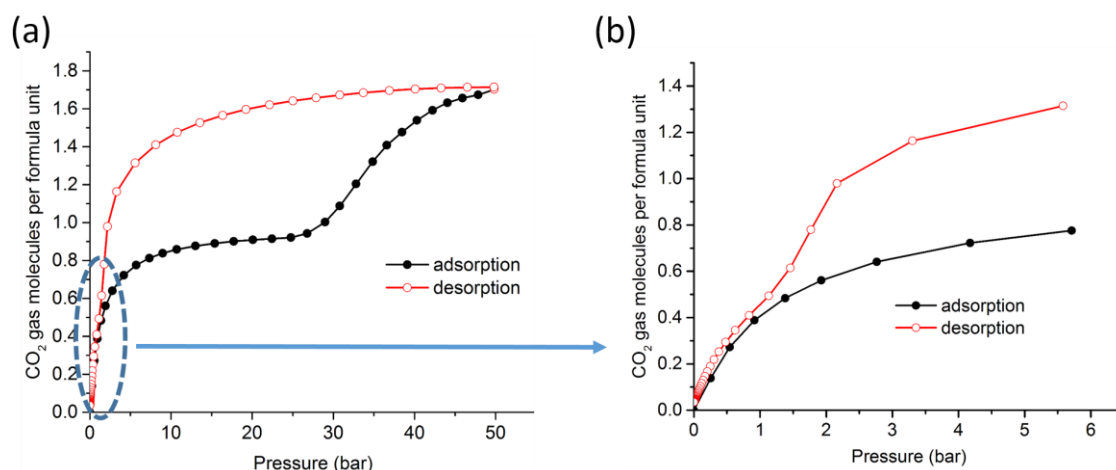


Figure S4. Sorption/desorption isotherms for **1-act** with CO₂ and N₂ gases at 298 K in the range (a) 0 to 50 bar and (b) the same data plotted from 1 to 6 bar.

References

1. *SAINT Data Reduction Software*, Version 6.45; Bruker AXS Inc., Madison, WI, 2003.
2. (a) *SADABS*, Version 2.05; Bruker AXS Inc., Madison, WI, 2002; (b) Blessing, R. H. *Acta Crystallogr., Sect. A: Found. Crystallogr.* 1995, **51**, 33.
3. G. M. Sheldrick, *Acta Crystallogr., Sect. A: Found. Crystallogr.* 2008, **64**, 112.
4. (a) L. J. Barbour, *J. Supramol. Chem.* 2001, **1**, 189; (b) L.J. Bourhis, O.V. Dolomanov, R.J. Gildea, J.A.K. Howard, H. Puschmann, *Acta Cryst.* 2015. **A71**, 59.
5. Connolly, M. L. *J. Mol. Graphics.* **1993**, *11*, 139-141

6. S. J. Clark, M. D. Segall, C. J. Pickard, P. J. Hasnip, M. J. Probert, K. Refson, M. C. Payne, Z. *Kristallogr.* 2005, **220**, 567.

CHAPTER 5

Summary and Conclusion

This dissertation is a compilation of three separate manuscripts, each of which describes the formation and characterisation of a cobalt-based MOF or PCP. The summaries and conclusions of the separate studies are provided in the corresponding manuscripts, and the objective of this final chapter is to provide an overview that ties the work together. Suggestions for further work are also provided here.

The new robust non-interpenetrated flexible MOF $\{[\text{Co}_2(\text{OBA})_2(\text{BPMP})]\cdot 1.5(\text{DMF})\}_n$ (**COB-DMF**) was synthesised solvothermally to yield crystals suitable for diffraction experiments. The crystals of the as-synthesised framework survive desolvation under dynamic vacuum to afford activated crystals of **COB**. SCD analysis shows that the network connectivity remains intact upon activation, but that the space group changes from $F2dd$ (**COB-DMF**) to $Fddd$ (**COB-act** and **COB⁰**). The guest-accessible space of **COB-DMF** consists of discrete mushroom-shaped voids. Activation causes each of these cavities to split into two crystallographically unique ellipsoidal voids, with a 27% decrease in total solvent-accessible volume and a centrosymmetric arrangement of guest-accessible pockets. From the CO_2 sorption isotherm it was inferred that **COB** undergoes two gas-induced phase transitions in the range 0-50 bar, with moderate hysteresis upon desorption. However, VP-PXRD and VP-SCD analyses (0 to 50 and 0 to 35 bar, respectively) show that only one phase change occurs in these pressure ranges. From the SCD data it was possible to obtain structural insight related to the phase changes by comparing the crystal structures of the as-synthesised, activated and CO_2 -loaded forms. The framework undergoes an unusual combination of two processes, i.e. breathing and overall swelling. Our use of VP-PXRD and VP-SCD to establish that the second step in the sorption isotherm is not due to a phase change highlights the importance of in situ techniques to establish the identities of the phases that undergo gas inclusion. This work can be further enhanced by determining the energies of sorption and desorption using pressure-gradient differential scanning calorimetry (PG-DSC). In the work described above it was not possible to model the CO_2 guest molecules since the diffraction data were recorded at room temperature. Future studies might focus on redetermining these structures at low temperature in the hope of obtaining reliable models for the guests. Such studies would involve overcoming some technical challenges associated with environmental gas cell work at low temperature.

It is interesting that the same components (and in the same ratios) that yielded **COB** produced a completely different MOF ($\{[\text{Co}_2(\text{OBA})_2(\text{BPMP})]\cdot 2.5(\text{DMF})\}_n$, **COB1-DMF**) when the temperature of the synthesis was altered. **COB1-DMF** also consists of a new non-interpenetrated MOF with discrete guest-accessible pockets. It displays structural flexibility upon activation, transforming from a wide-pore to a narrow-pore form (a decrease in accessible volume from 38% to 17%). CO_2 sorption analysis at 298 K reveals a stepped sorption/desorption profile for **COB1⁰** with significant hysteresis. The large step in the sorption isotherm is attributed to the phase change to **COB1-CO2¹⁹**, with a concomitant sudden increase in the guest-accessible volume. This phase change is well supported by VP-SCD, PG-DSC analysis and computational modelling. PXRD analysis shows that the sorption/desorption process is ultimately reversible for the most part, but that some of the sample remains in the open form even when all of the CO_2 has been removed. Reactivation of the sample by heating at 120 °C under dynamic vacuum ensures complete reversion to the original activated phase. It is interesting to note that the PG-DSC shows one

peak (possibly a peak with a shoulder) upon sorption while three distinct peaks are observed for desorption. As yet, we do not have an explanation for this observation since the single crystals do not survive desorption intact. Future studies might focus on investigating a milder desorption protocol in the hope of obtaining structural information regarding the complex three-step desorption process. Preliminary variable-temperature PG-DSC studies showed that, as expected, the onset pressures of the uptake/release processes are highly temperature-dependent. It would be of considerable interest to expand the study to determine the exact relationship between onset pressure and temperature, and to investigate whether such a relationship might be generalised to other materials.

The new flexible porous coordination polymer $\{[\text{Co}_2(\text{OBA})_2(\text{BPY})_2] \cdot 2(\text{DMF})\}_n$ (**1-DMF**) was prepared and characterised. Upon activation **1-DMF** switches from possessing one type of void exclusively to having two different types of voids. Once again the single crystals survive activation intact and it was possible to determine the structures of **1-DMF** and **1-act**. The CO_2 sorption isotherm for **1-act** exhibits a single large step with an onset pressure of 27 bar at 298 K. The desorption profile displays significant hysteresis and, at first, appears to indicate shape-memory (i.e. that the structure remains in the open form after complete desorption). However, VP-PXRD shows that the material reverts to the original activated form when the CO_2 gas is removed. Closer inspection of the desorption isotherm in the low pressure range shows that there is a step with an onset pressure of between 2 and 1 bar. The 36 bar hysteresis in the reversibility of the gate-opening phase change is remarkable. Unfortunately it was not possible to obtain the crystal structure of the gas-loaded form at 50 bar since the single crystals did not survive sorption intact. Once again, these results highlight the importance of employing complementary in situ techniques to monitor sorption/desorption processes. It would therefore be of interest to extend this study by investigating milder conditions for adsorption and desorption such that the single crystals might survive. In that case we would be able to elucidate the mechanism responsible for the gate-opening phase transition under CO_2 gas pressure by means of our environmental gas cell.

The three new porous metal-organic systems described in this dissertation have provided some insight into their flexibility. This was achieved by using a complementary range of experimental techniques, as well as molecular modelling (in two of the cases).

APPENDIX

A CD containing all the supporting files and videos provides the following:

Chapter 2:

- ✓ CIF files and CheckCIF reports

Chapter 3:

- ✓ CIF files and CheckCIF reports

Video S1 and S2: showing the phase change under CO₂ controlled gas pressure

Chapter 4:

- ✓ CIF files and CheckCIF reports

